

# Cool DZ white dwarfs I: Identification and spectral analysis

M.A. Hollands,<sup>1\*</sup> D. Koester,<sup>2</sup> V. Alekseev,<sup>3</sup> E.L. Herbert,<sup>1</sup> and B.T. Gänsicke<sup>1</sup>

<sup>1</sup> *Department of Physics, University of Warwick, Coventry CV4 7AL, UK*

<sup>2</sup> *Institut für Theoretische Physik und Astrophysik, University of Kiel, 24098 Kiel, Germany*

<sup>3</sup> *St. Petersburg State University, 7/9 Universitetskaya Nab., 199034 St. Petersburg, Russia*

Accepted 2017 January 26. Received 2017 January 26; in original form 2016 November 25

## ABSTRACT

White dwarfs with metal lines in their spectra act as signposts for post-main sequence planetary systems. Searching the Sloan Digital Sky Survey (SDSS) data release 12, we have identified 231 cool ( $< 9000$  K) DZ white dwarfs with strong metal absorption, extending the DZ cooling sequence to both higher metal abundances, lower temperatures, and hence longer cooler ages. Of these 231 systems, 104 are previously unknown white dwarfs. Compared with previous work, our spectral fitting uses improved model atmospheres with updated line profiles and line-lists, which we use to derive effective temperatures and abundances for up to 8 elements. We also determine spectroscopic distances to our sample, identifying two halo-members with tangential space-velocities  $> 300 \text{ km s}^{-1}$ . The implications of our results on remnant planetary systems are to be discussed in a separate paper.

**Key words:** (stars:) white dwarfs – planets and satellites: composition – (stars:) atmospheres – (stars:) abundances

## 1 INTRODUCTION

White dwarfs are often found to have traces of metals polluting their otherwise pristine atmospheres of hydrogen or helium (van Maanen 1917; Weidemann 1960; Hintzen & Tapia 1975; Shipman et al. 1977; Aannestad & Sion 1985; Zuckerman & Reid 1998; Koester & Kepler 2015). These are classified as spectral types DAZ, DBZ, and DZ, depending on whether hydrogen, helium, or no lines are present in the spectrum in addition to those from metals (Sion et al. 1983). Due to gravitational settling, metals are expected to sink below the observable photosphere on time scales many orders of magnitude shorter than the white dwarf cooling age (Koester 2009). Therefore the observed atmospheric contamination by metals at 25–50 percent (Zuckerman et al. 2003; Koester et al. 2014) of white dwarfs requires recent or ongoing accretion of metal-rich material (Vauclair et al. 1979).

In the last two decades it has become clear that these accreted metals originate from rocky debris that has survived the post-main sequence evolution of its host star (Graham et al. 1990; Jura 2003; Farihi et al. 2010). This astonishing realisation has led to white dwarfs becoming the primary tool for directly probing the bulk compositions of rocky planetary material (Zuckerman et al. 2007; Gänsicke et al. 2012).

The first indicator pointing towards a planetary origin for metal-pollution came from the detection of white dwarfs

with infra-red excesses (Zuckerman & Becklin 1987; Becklin et al. 2005; Kilic et al. 2005). The infra-red flux is interpreted to come from circumstellar dust discs that have thermally reprocessed the light incident from the close-by white dwarf (Graham et al. 1990). Gaseous components to these discs have also been identified at a handful of young metal-polluted white dwarfs (e.g. Gänsicke et al. 2006; Dufour et al. 2012; Melis et al. 2012; Farihi et al. 2012; Wilson et al. 2014; Guo et al. 2015), typically through double peaked emission lines of Ca II and Fe II.

The now established scenario is that perturbations to the trajectories of small planetary objects such as asteroids can occasionally push them onto grazing orbits with the degenerate star (Debes & Sigurdsson 2002). Mass-loss during evolution off of the main-sequence results in reduced dynamical stability at the white dwarf stage, increasing the probability of this scenario occurring (Veras & Gänsicke 2015). Once within the white dwarf’s Roche radius, the planetesimal is tidally disrupted which circularises into a debris disc, and finally is accreted onto the surface of the star (Jura 2003; Veras et al. 2014a). A recent review of remnant planetary systems by Veras (2016) can be consulted for more details.

While this picture of evolved planetary systems has adequately explained observations for more than a decade, the most unambiguous evidence surfaced only recently, with deep transits (up to 40 percent) in the K2 lightcurve of WD1145+017, leading to the discovery of a disintegrating planetesimal orbiting near the Roche radius of this star

\* E-mail: M.Hollands@warwick.ac.uk

( $P_{\text{orb}} \simeq 4.5$  hr) (Vanderburg et al. 2015; Gänsicke et al. 2016; Alonso et al. 2016; Rappaport et al. 2016). WD1145+017 also exhibits an infra-red excess, broad absorption features from transiting circumstellar gas (Xu et al. 2016), and an atmosphere enriched with metals. WD1145+017 therefore provides the firmest link between metals in the atmospheres of white dwarfs and rocky planetary material. Unfortunately the prospect of detecting a statistically large sample of WD1145+017-like systems in the near future is low considering the chance alignment required, and the potentially short timescales for which transits are visible. For the foreseeable future, the study of white dwarfs with metal-line spectra remains the primary tool in understanding the variety of remnant planetary systems.

Over the last 15 years, the Sloan Digital Sky Survey (SDSS) has been an invaluable source of white dwarf discoveries, providing spectroscopy for  $> 40\,000$  stellar remnants of all spectral types and spanning all temperature regimes (Kleinman et al. 2004; Eisenstein et al. 2006; Kleinman et al. 2013; Kepler et al. 2015, 2016). More than one thousand of these white dwarfs also possess metal-lines.

In this work we consider only DZ white dwarfs, which have spectra with only metal lines present. The absence of hydrogen/helium lines simply reflects their relatively low effective temperatures ( $T_{\text{eff}}$ ) as they have cooled for at least  $\simeq 0.5$  Gyr since leaving the tip of the AGB. Below  $\simeq 12\,000$  K helium atoms are almost entirely in the ground state, while optical transitions of helium all occur between excited states. Therefore white dwarfs with pure helium atmospheres, have featureless spectra below  $\simeq 12\,000$  K. Below  $\simeq 5000$  K the Balmer lines also disappear for white dwarfs with hydrogen dominated atmospheres. Because of the wider temperature range that helium lines are absent, but also because of the much lower opacity of helium compared with hydrogen (leading to stronger metal lines for given abundances), most of the known DZ stars have atmospheres dominated by helium. This includes the first known metal-polluted white dwarf, vMa2 (van Maanen 1917), which is both the prototype DZ, and the first *acquired* evidence for an extrasolar planetary system (Zuckerman 2015; Farihi 2016), although another 90 years were needed for a correct interpretation (Jura 2003).

Prior atmospheric analyses of DZ white dwarfs by Bergeron et al. (2001) and Dufour et al. (2007), found a wide range in the level of observed metal pollution across the  $T_{\text{eff}}$  range of their samples (see Figure 9 of Dufour et al. 2007). However below  $\simeq 7000$  K only one object, G165-7 (SDSS J1330+3029 later in this work), was found with  $\log[\text{Ca}/\text{He}] > -9$  dex. The authors noted that this could be explained as a selection bias. The majority of the DZs analysed by Dufour et al. (2007) came from the SDSS white dwarf catalogue of Eisenstein et al. (2006), which was subject to a colour-cut excluding objects with  $(u-g)$  sufficiently red to overlap the main-sequence. This colour-cut would also preclude the identification of SDSS objects spectrally similar to G165-7 ( $u-g = 1.96 \pm 0.03$  mag), which was instead included by Dufour et al. (2007) as one of twelve additional systems from Bergeron et al. (1997) and Bergeron et al. (2001).

The suspicion of selection effects by Dufour et al. (2007) was soon proved correct by Koester et al. (2011) (hereafter KGGD11) who searched specifically for DZs with strong

metal-pollution and low  $T_{\text{eff}}$  similar to G165-7. KGGD11 noted that such white dwarfs would follow cooling tracks extending below the main-sequence in  $(u-g)$  vs.  $(g-r)$  (see Figure 1), exhibiting colours not possible for other types of stars due to extremely strong H/K line absorption in the SDSS  $u$ -band. In total KGGD11, identified 26 cool DZs ( $T_{\text{eff}} < 9000$  K) with spectra strongly line-blanketed by metals, occupying a previously sparse corner of the  $T_{\text{eff}}$  vs.  $\log[\text{Ca}/\text{He}]$  plane.

In this study, we extend the work of KGGD11 to SDSS DR12, finding 231 cool DZ white dwarfs with strong metal lines. These stars provide not only detailed information on ancient exoplanetary chemistry, but also serve as laboratories for state of the art atomic physics under the extreme conditions found in white dwarf atmospheres.

As our analysis of DZ white dwarfs covers a broad range of astrophysical phenomena, we present our results in three distinct papers. Here (Paper I), we discuss the identification of our DZ sample, our latest model atmospheres, and the fitting of these models to the observed spectra. Additionally we examine the properties of our new sample combined with the complementary work of Dufour et al. (2007) and Koester & Kepler (2015). In paper II, we discuss the bulk compositions of the accreted planetesimals which we obtained from our spectral fits, as well as our sample in the wider context of ancient exoplanetary systems. Finally, we find that more than 10 percent of our DZ sample exhibit Zeeman-splitting from strong ( $> 0.5$  MG) magnetic fields which we discuss in paper III.

## 2 WHITE DWARF IDENTIFICATION

### 2.1 Spectroscopic search

We adopted two distinct methods to identify DZ white dwarfs from the SDSS DR12 spectra. The first (*method 1*) makes use of various data cuts (colour, proper-motion, etc.) to filter the number of objects requiring visual inspection. Following the release of SDSS DR12, we employed a new identification scheme (*method 2*) where we fit all SDSS spectra with DZ templates. This method was found to be superior to *method 1* as it required fewer spectra to be visually inspected, and allowed a larger range of colour space to be explored. We still describe the first method briefly as the initial results it provided were used to calibrate the template fitting approach.

#### 2.1.1 Method 1

The first method is essentially an extension of the work by KGGD11 to subsequent SDSS data releases. We restricted our search for further cool DZs firstly to SDSS point-sources, and then performing a colour-colour cut in  $(u-g)$  vs.  $(g-r)$  (dashed region in Figure 1), similar to that used by KGGD11. This region avoids the main sequence and contains the 17 coolest and most metal polluted DZs found by KGGD11. While this area of colour-space was chosen to avoid other types of stellar objects, it is instead home to quasars with Ly- $\alpha$  breaks occurring in the  $u$ -band, which were intensely targeted for spectroscopy in SDSS-III (Ross et al. 2012). While this targeting strategy leads to cool DZ

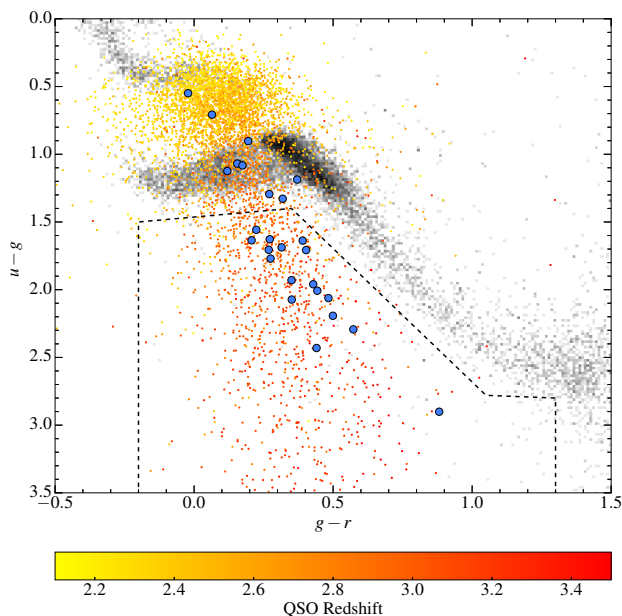


**Figure 1.** Our colour-cut (dashed line) is similar to that used by KGGD11, although their  $u - g < 3.2$  constraint is removed. The cut includes 17 of the original KGGD11 sample (blue points) which are the coolest and most metal-rich of their stars. A random sample of SDSS quasars is shown by the smaller coloured points – their colour corresponding to the redshift, illustrating the degeneracy between DZs and QSOs in this colour-space.

stars being serendipitously observed, these quasars required filtering from our colour selection.

We removed quasars using a combination of proper-motion and spectroscopic redshifts: We required a  $> 3\sigma$  detection of proper-motions, where SDSS proper-motion errors are typically  $2\text{--}6 \text{ mas yr}^{-1}$ . The total proper-motion is chi-distributed with two degrees-of-freedom, whereas the  $1\text{-}\sigma$  errors correspond to single components, therefore  $\simeq 1$  percent of the  $\simeq 477\,000$  quasar spectra<sup>1</sup> will have measured proper-motions in excess of our  $3\sigma$ -cut. Using *only* proper-motion to filter quasars was insufficient as these are not always available for faint,  $g > 20$  objects, due to lack of cross-detections in USNO-B. Additionally a few high proper-motion systems ( $> 100 \text{ mas yr}^{-1}$ ) have such large displacement between SDSS and USNO-B photometry that cross-matching fails. For instance, SDSS J1144+1218 (KGGD11) has no available SDSS proper-motion, but is found in PP-MXL with a celestial motion of  $617 \pm 6 \text{ mas yr}^{-1}$  (see appendix Table A4).

We supplemented our proper-motion cut with a cut on redshift,  $z$ , to remove additional quasars, and avoid missing DZs with no SDSS proper-motion – systems only needed to pass one of the two tests to make it to the next stage. For the redshift cut we imposed  $z - 3\sigma_z < 0.01$ , removing both quasar and galaxy spectra from our sample. The relative rarity of cool DZ spectra in SDSS can lead to incorrect spectral classification and subsequently an incorrect redshift

<sup>1</sup> See <http://www.sdss.org/dr12/scope/> for a breakdown of all SDSS DR12 spectroscopy.

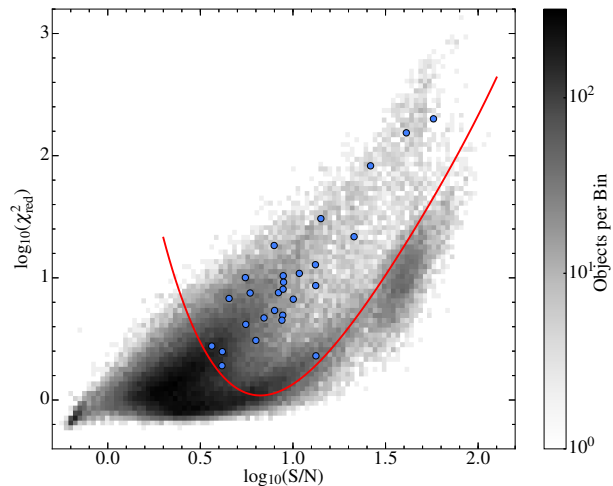


**Figure 2.** Density map in the  $\chi^2_{\text{red}}$ -S/N plane for proper-motion/redshift selected objects. Blue points are the DZs identified by KGGD11 that fall within our colour-cut. Several of these systems have more than one SDSS spectrum (see appendix Table A1 for number of SDSS spectra per object), hence there are more than 17 points shown here. The red curve indicates a 4th-order polynomial in log-log space which defines our final cut.

estimate from the SDSS pipeline. Therefore we allowed objects with the `zwarning` flag not equal to zero to “automatically pass” our redshift test (zero indicates a  $z$  value that is deemed to be correct). However of the 17 KGGD11 DZs within our colour-cut, five were found with  $1.38 < z < 1.41$  and `zwarning` = 0, indicating that DZ stars can be misclassified as quasars with no warning flags raised in this narrow redshift range. Therefore an exception to our redshift cut was made for the few SDSS spectra with  $1.3 < z < 1.5$ .

Our combined proper-motion/redshift cut successfully removed most QSOs and galaxies, thus reducing the size of the sample of purely colour-selected spectra by 33 percent to around 100 000. At this stage, all 17 DZs from KGGD11 were still contained within the selection.

As this sample was still rather large for visual inspection, we sought to remove additional contaminants. Most of the remaining spectra were of K/M dwarfs at the border of our colour-cut. We performed template fitting for spectral subclasses K1–M9 to remove these cool main sequence stars. For M dwarfs we used the templates from [Rebassa-Mansergas et al. \(2007\)](#). For subclasses K1, K3, K5 and K7 we created templates by combining multiple (at least 20 per subclass) high signal-to-noise (S/N) SDSS spectra which we identified in the CasJobs database ([Li & Thakar 2008](#)) using the `class` and `subclass` attributes.

We fitted each of the 100 000 spectra against all stellar templates, obtaining a reduced chi-squared ( $\chi^2_{\text{red}}$ ) for each fit. The template with lowest  $\chi^2_{\text{red}}$  for a given spectrum was recorded as the best-fitting template. The median S/N was also recorded for each SDSS spectrum.

The resulting distribution in the S/N vs.  $\chi^2_{\text{red}}$  plane (Figure 2) is bimodal at high-signal to noise indicating probable main sequence stars in the lower cluster, and objects spectrally different to the K/M star templates in the upper branch. The bulk of spectra are found at low signal-to-

noise/low  $\chi_{\text{red}}^2$ , and so are of too poor quality for meaningful analysis. The KGGD11 DZs were used to define a cut-off for the remaining spectra as indicated by the red line. This has the effect of removing the high S/N and low  $\chi_{\text{red}}^2$  (main sequence) objects, as well as very low S/N spectra.

The  $\chi_{\text{red}}^2$ -S/N cut reduced the sample size down to  $\simeq 35\,000$  spectra which we visually inspected for DZ white dwarfs. In total we identified 126 spectra corresponding to 103 unique DZ stars. Some objects had additional spectra which were not identified via *method 1* (e.g. because of low S/N), but were found upon searching for spectra with the same SDSS ObjID. This brought the total number of DZ spectra to 138 for the 103 systems.

### 2.1.2 Method 2

While we successfully identified more than 100 cool, metal-rich DZs with *method 1*, its scope was severely limited by our initial colour-cut. Of the 26 DZ white dwarfs in the KGGD11 sample, 9 were excluded by this cut (Figure 1), suggesting that many more DZs may have colours overlapping the main-sequence in  $(u-g)$  vs.  $(g-r)$ . Additionally, the  $u$ -band errors for DZs in SDSS are sometimes  $> 1.0$  mag, and so while the true  $u-g$  value should place a system below the main sequence in Figure 1, the measured colour could instead escape our colour cut. Furthermore, the possibility remained that systems could fail both our proper-motion and redshift tests, or also fall under our  $\chi_{\text{red}}^2$ -cut in Figure 2.

*Method 2* essentially uses only the SDSS spectra for identification, and so allows us to identify objects that would otherwise be photometrically degenerate with main sequence stars. To provide zeroth-order estimates of atmospheric parameters for our spectral fitting (described later in Section 5), we generated a grid of DZ models of varying  $T_{\text{eff}}$  and  $\log[\text{Ca}/\text{He}]$ . The grid spanned  $4400\text{ K} \leq T_{\text{eff}} \leq 14\,000\text{ K}$  in steps of 200 K and  $-10.5 \leq \log[\text{Ca}/\text{He}] \leq -7$  in steps of 0.25 dex (735 DZ model spectra). For all models in the grid the surface gravity,  $\log g$ , is fixed to the canonical value of 8. Other elements were fixed to bulk Earth abundances (McDonough 2000) relative to Ca. We found our model grid could also be used as templates to identify DZ white dwarfs through fitting to the SDSS spectra.

We supplemented our DZ grid with a list of the highest quality SDSS spectra with average S/N  $> 100$ . These consisted entirely of main sequence stars of spectral-types B through K, and amounted to 768 spectra bringing the total number of templates to 1503.

With these template spectra at hand we fitted each template against *all* 2.4M SDSS spectra with mean S/N  $> 3$  – this S/N cut removes not only the poorest quality spectra, but also quasars where the bulk of the signal is contained within a few narrow emission lines. For each fit the template spectra were linearly interpolated onto the same wavelength grid as the SDSS spectrum under consideration – the high S/N requirement of the non-DZ templates meant the effects of interpolating noise were kept to a minimum. Secondly, a reduced  $\chi^2$  was calculated between the SDSS spectrum and interpolated template with only a scaling factor as a free parameter. Ignoring the small flux errors on the non-DZ templates, the optimum scaling factor,  $A$ , has the simple

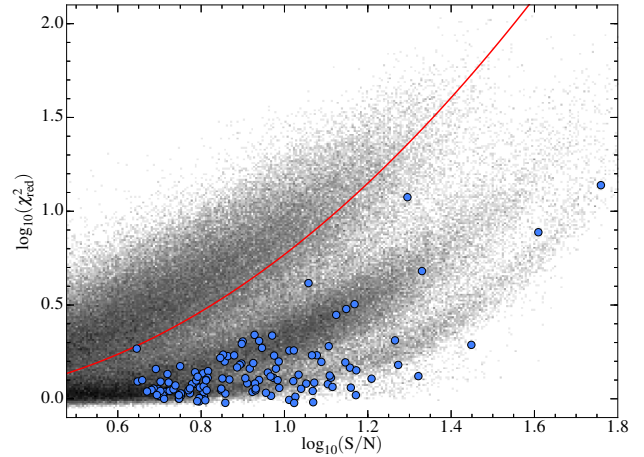


**Figure 3.** Density map in the  $\chi_{\text{red}}^2$ -S/N plane for objects with best fits to DZ templates. Blue points correspond to the DZ spectra identified using *method 1*. Our  $\chi_{\text{red}}^2$ -cut is indicated by the red parabola.

analytic form

$$A = \frac{\sum_i f_i t_i / \sigma_i^2}{\sum_j t_j^2 / \sigma_j^2}, \quad (1)$$

where the  $f_i$  and  $\sigma_i$  are the fluxes and errors on the SDSS spectra and the  $t_i$  are the unscaled fluxes on the interpolated templates. For each SDSS spectrum, the template with the lowest  $\chi_{\text{red}}^2$  was considered to be the best fit.

SDSS spectra which best fit a non-DZ template were immediately discarded, reducing the 2.4M spectra to  $\simeq 244\,000$ . All SDSS DZ spectra identified via *method 1* still remained after this cut. Next we applied a single colour cut of  $u-g > 0.50$ , essentially enforcing that white dwarfs in our sample contain significant absorption in the blue end of their spectra. This has the effect of removing DZ stars with  $T_{\text{eff}} > 9000\text{ K}$  for the most metal rich objects and  $T_{\text{eff}} > 6500\text{ K}$  for the lowest metallicities in our grid. Hotter objects are not the focus of this work.

Although only  $\simeq 10$  percent of objects best-fit a DZ template, the best fit does not imply a good fit. Thus we next cut on  $\chi_{\text{red}}^2$  vs. S/N, similarly to *method 1* (Figure 2). The cut is a parabola in  $\log(\chi_{\text{red}}^2)$  vs.  $\log(\text{S/N})$ , whose scale we chose to keep all objects identified through *method 1*. This is shown in Figure 3.

At S/N  $> 7$ , the distribution in Figure 3 becomes trimodal in  $\chi_{\text{red}}^2$  with only the upper cluster filtered by our cut. We found the majority of points in the intermediate distribution had best fitting templates with the lowest two values of  $\log[\text{Ca}/\text{He}]$  ( $-10.5$  and  $-10.25$  dex) in our model grid. This is because those templates are relatively featureless and so had a tendency to match other types of main-sequence stars. Therefore we chose to remove all spectra matching the low Ca-abundance templates, leaving only  $\simeq 10\,600$  spectra for visual inspection<sup>2</sup>.

<sup>2</sup> While this final cut inevitably biases us towards high-metallicity systems, objects with  $\log[\text{Ca}/\text{He}] < -10$  do not permit



**Table 1.** Coordinates, SDSS spectral identifiers, and photometry for the ultracool white dwarfs we have serendipitously discovered.

SDSS J	Plate-MJD-Fib	$u$ [mag]	$g$ [mag]	$r$ [mag]	$i$ [mag]	$z$ [mag]	Ref.
003908.33+303538.9	6526-56543-0006	$21.731 \pm 0.260$	$20.397 \pm 0.038$	$20.449 \pm 0.047$	$20.975 \pm 0.096$	$21.159 \pm 0.445$	
025754.92+042807.5	4256-55477-0926	$22.725 \pm 0.338$	$21.154 \pm 0.040$	$20.650 \pm 0.045$	$21.067 \pm 0.076$	$21.207 \pm 0.263$	
100103.42+390340.4	1356-53033-0280	$21.303 \pm 0.118$	$20.017 \pm 0.030$	$19.587 \pm 0.021$	$19.956 \pm 0.042$	$20.524 \pm 0.236$	1
133739.40+000142.8	0299-51671-0357	$20.795 \pm 0.054$	$19.546 \pm 0.022$	$19.138 \pm 0.021$	$19.521 \pm 0.023$	$20.022 \pm 0.088$	2
140237.31+080519.1	4863-55688-0792	$21.960 \pm 0.195$	$21.419 \pm 0.055$	$21.331 \pm 0.060$	$21.513 \pm 0.131$	$20.966 \pm 0.186$	
144440.01+631924.4	6983-56447-0685	$21.729 \pm 0.120$	$20.375 \pm 0.031$	$20.223 \pm 0.030$	$20.081 \pm 0.036$	$20.137 \pm 0.130$	
170320.12+271106.8	5013-55723-0128	$22.500 \pm 0.183$	$21.428 \pm 0.037$	$20.841 \pm 0.032$	$21.164 \pm 0.064$	$21.158 \pm 0.231$	
225817.87+012811.1	4290-55527-0290	$21.102 \pm 0.096$	$19.828 \pm 0.026$	$19.626 \pm 0.021$	$20.077 \pm 0.032$	$20.528 \pm 0.152$	
231130.14+283444.8	6292-56566-0964	$22.677 \pm 0.205$	$21.143 \pm 0.029$	$20.958 \pm 0.035$	$21.270 \pm 0.055$	$21.100 \pm 0.179$	
234931.16-080245.6	7146-56573-0460	$22.432 \pm 0.429$	$21.034 \pm 0.038$	$20.822 \pm 0.050$	$20.972 \pm 0.081$	$20.399 \pm 0.176$	

References: (1) Gates et al. (2004), (2) Harris et al. (2001)

**Table 2.** Breakdown of methods 1 & 2 for the visually inspected SDSS spectra. For each spectral type, the *number/number* format indicates the total spectra, and the number of unique systems respectively.

Method	1	2
Main-sequence stars	29545/27660	6645/6253
Carbon stars	148/126	15/12
Quasars	4477/3575	2013/1895
Galaxies	128/123	9/9
WDMS binaries	33/30	0/0
<b>Cool DZ WDs</b>	126/103	291/229
Other WDs	61/59	773/715
Unclassifiable spectra	54/52	808/784
Total	34572/31728	10554/9897

We identified 291 DZ spectra via visual inspection corresponding to 229 unique white dwarfs, including all of those identified through *method 1*. Serendipitously, *method 2* also lead us to identify 10 ultracool white dwarfs, of which only 2 are previously known (Harris et al. 2001; Gates et al. 2004). Ultracool white dwarfs have temperatures below 4000 K, yet exhibit blue colours due to collision induced absorption of H<sub>2</sub> in their atmospheres. The 10 systems are listed in Table 1 and their spectra are displayed in Figure B1. Since we do not find all previously known SDSS ultracool white dwarfs (Harris et al. 2000; Gates et al. 2004; Harris et al. 2008), a targeted search via template fitting would likely find additional such objects.

### 2.1.3 Comparison of methods 1 & 2

*Method 2* was clearly superior to *method 1* for identifying DZ white dwarfs as it allowed us to identify additional systems and required manual inspection of fewer spectra. A comparison of all visually inspected spectra between the two methodologies is shown in Table 2. Note that the listed spectra for *method 2* are only a superset of *method 1* with respect to cool DZ white dwarfs. For instance *method 1* shows some sensitivity to carbon stars, as these are not rejected

by the K/M star template fitting shown in Figure 2, but *are* rejected by the DZ template fitting in *method 2*.

Our final sample of cool DZ white dwarfs is listed in appendix Table A1, which includes coordinates, plate-MJD-fiber identifiers, and SDSS photometry. For systems where multiple SDSS spectra are available, only one row is listed, where the plate-MJD-fiber ID corresponds to the spectrum fitted in Section 5. We also show an updated  $(u - g)$  vs.  $(g - r)$  colour-colour diagram for our sample in Figure 4. The left panel shows the observed colours for our sample, whereas the right panel shows the synthetic colours computed from our best-fitting models (Section 5). The difference in spread is due to the large  $u$ -band errors, which are biggest for very cool systems and those with strong metal absorption in the spectral range covered by the SDSS  $u$  filter.

## 2.2 Photometric search

We also attempted to identify potential DZ white dwarfs purely from SDSS photometry and astrometry, with the intention of subsequent spectroscopic follow-up. We filtered for point sources with clean photometry (using the `type` and `clean` flags), and the colour-cut indicated by the black dashed line Figure 1 was applied. Since the number of photometric sources dwarfs the already large size of the spectroscopic database, we also imposed a maximum magnitude of  $g < 18.5$  to filter on only the brightest objects. We also required all the magnitudes in all bandpasses  $> 15$  in order to avoid objects with saturated photometry. DZ white dwarfs within the specified brightness limit ought to have reasonably large proper-motions. We therefore required proper-motions to be at least  $50 \text{ mas yr}^{-1}$ , with a detection of at least  $3\sigma$  above zero.

The combination of these cuts resulted in a small sample of 217 objects. Many of these were in crowded fields and so their proper-motions were not considered trustworthy. In total, six known DZ stars with spectra were recovered. These are SDSS J0116+2050, SDSS J0916+2540, SDSS J1214-0234, SDSS J1330+3029, SDSS J1336+3547, and SDSS J1535+1247.

Two objects (SDSS J0512-0505 and SDSS J0823+0546) were identified as clear DZ white dwarfs contenders, and were both followed up in Dec 2013 using the William Herschel Telescope (WHT – details of the spectroscopic reduction are summarised in Section 3).

meaningful chemical analyses of the accreted material, with Ca as potentially the only detected element.

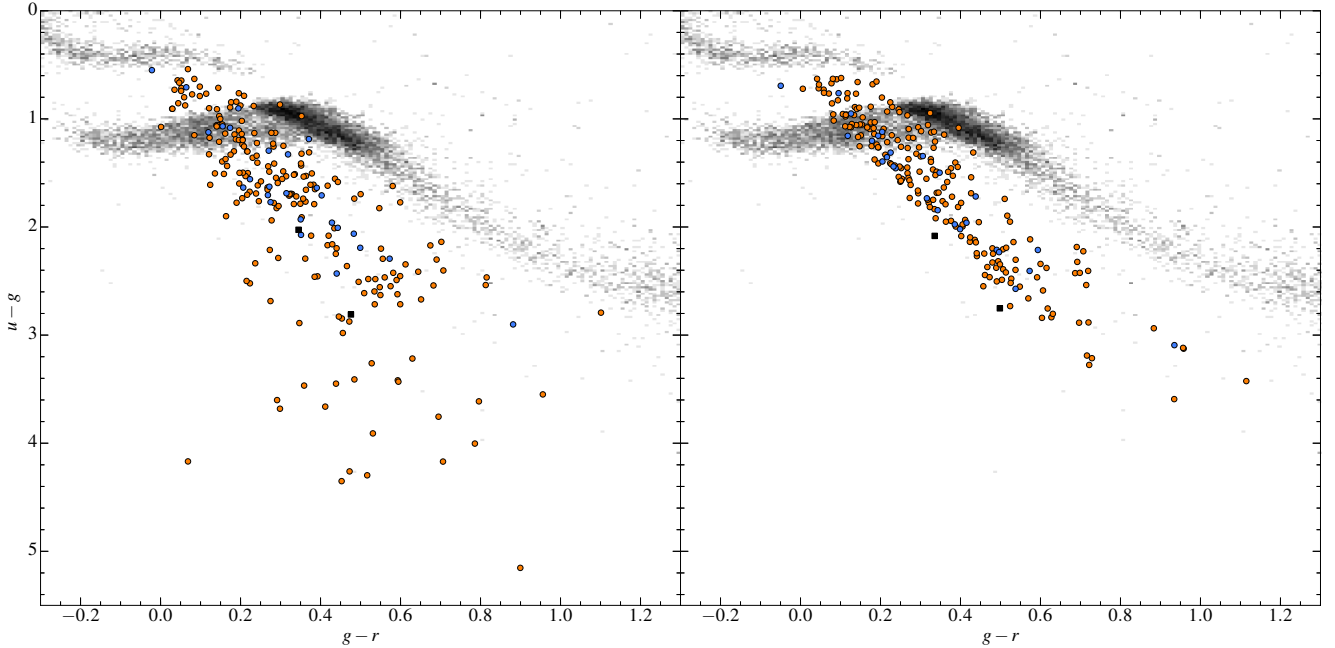


**Figure 4.** Colour-colour diagrams of our white dwarf sample. The left panel shows the observed SDSS colours, whereas those on the right are the synthetic colours from our best fit models. Objects also in the KGGD11 sample are shown in blue, photometrically identified DZs as black squares, and the remainder of our sample in orange. The increased scatter for the observed colours is dominated by uncertainty on the  $u$ -band fluxes which in some cases can exceed 1 mag.

The observations confirmed both targets to be cool DZ white dwarfs and we include them in all relevant figures and tables throughout this work. These two systems bring our full DZ sample to 231 unique objects. As six of the eight objects our photometric search highlighted as possible DZ white dwarfs already had SDSS spectra, this indicates a high spectroscopic completeness for DZ white dwarfs in the range  $15 > g > 18.5$ .

### 2.3 Note on magnetic objects

Prior to [Hollands et al. \(2015\)](#) the only known magnetic DZ white dwarfs (DZH) were LHS2534 ([Reid et al. 2001](#)), WD0155+003 ([Schmidt et al. 2003](#)) and G165-7 ([Dufour et al. 2006](#)), which were identified through Zeeman split lines of Mg I, Na I, Ca II, and Fe I. All 3 systems have SDSS spectra and are included in our sample with respective names SDSS J1214-0234, SDSS J0157+0033, and SDSS J1330+3029. In the early stages of this work, before the release of SDSS DR12, we had identified a further 7 magnetic DZs which have already been published ([Hollands et al. 2015](#)).

Since the release of DR12, we have identified further DZH including some we had missed from DR10 (fields  $\lesssim 1$  MG are only detectable from close inspection of the sharpest lines, with further objects found through the expanded colour-selection of method 2). Our full list of magnetic DZs is given in Table 3.

While magnetic white dwarfs are interesting astrophysical objects in their own right, their magnetic nature is beyond the scope of this paper, and will be discussed in a separate publication (Paper III). However, their presence

requires some mentioning here, as the magnetic fields affect the quality of our spectroscopic fits which do not incorporate magnetism, and varying degrees caution should be applied when considering results for these stars. In the best cases (lowest fields) like SDSS J1330+3029, the effect of magnetism on line shapes/equivalent widths is minimal and so our  $T_{\text{eff}}$ /abundance values can be trusted as much as the non-magnetic case. In the highest field cases like SDSS J1536+4205 the effect is much greater with the uncertainty in  $T_{\text{eff}}$  around 500 K and abundances uncertainties likely around 0.5 dex. SDSS J1143+6615 is a special case where the field is so high, that attempting to fit with a non-magnetic model was found to be a pointless exercise. Therefore this star is included here as a DZ identification only.

### 3 ADDITIONAL SPECTRA

The 26 DZ white dwarfs analysed by KGGD11 were identified before the introduction of BOSS, and their spectra only extended as blue as  $\simeq 3800 \text{ \AA}$ , i.e. covering the cores of the Ca H/K doublet, and its red wing. However the blue wing extends several hundred  $\text{\AA}$  further. Synthetic  $(u - g)$  colours calculated by KGGD11 from their best fit models were found to be in poor agreement with the reported SDSS colours, typically over-predicting  $u$ -band flux by about 50 percent, and in the worst case by a factor 2.9 (SDSS J2340+0817). This result indicated our models required an additional source of opacity bluewards of  $3800 \text{ \AA}$ .

The newer BOSS spectrograph offers bluer wavelength coverage down to  $\simeq 3600 \text{ \AA}$ . The spectra of DZs observed

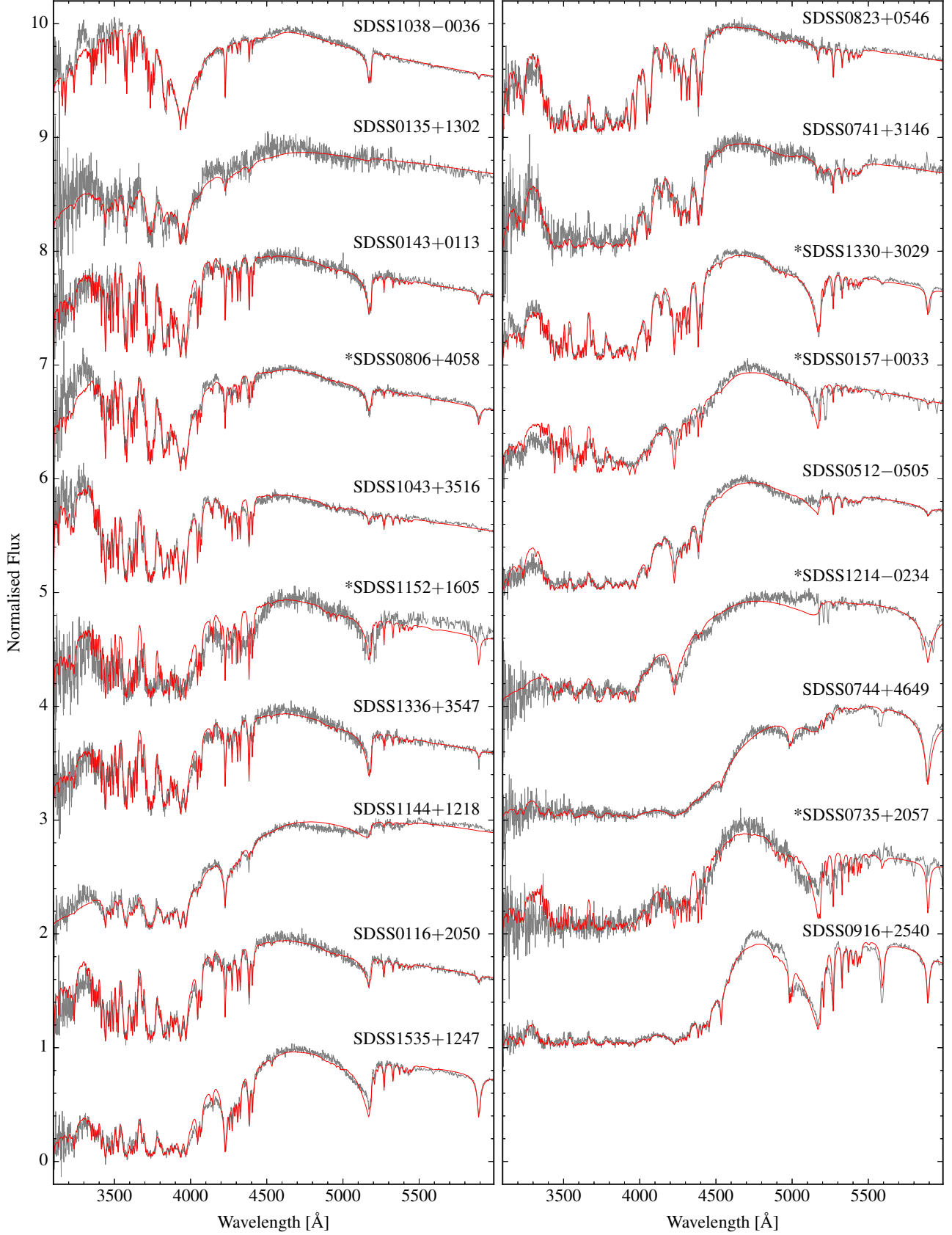


**Figure 5.** WHT spectra taken down to the atmospheric cutoff, ordered by approximate level of absorption below 4500 Å. Spectra are peak normalised to 1 and offset by 1 from one another. Magnetic objects are indicated by asterisks.

**Table 3.** Magnetic objects in our sample with the measured average field strengths and their detected Zeeman split lines.

SDSS J	$B_S$ [MG]	Split lines	Note	Ref.
SDSS J0037−0525	$7.09 \pm 0.04$	Mg I, Na I		1,2
SDSS J0107+2650	$3.37 \pm 0.07$	Mg I, Na I		1,2
SDSS J0157+0033	$3.49 \pm 0.05$	Mg I,		3
SDSS J0200+1646	$10.71 \pm 0.07$	Mg I, Na I		1
SDSS J0735+2057	$6.12 \pm 0.06$	Mg I, Na I		4
SDSS J0806+4058	$0.80 \pm 0.03$	Na I, Fe I		1
SDSS J0832+4109	$2.35 \pm 0.11$	Na I		4
SDSS J0902+3625	$1.92 \pm 0.05$	Na I		4
SDSS J0927+4931	$2.10 \pm 0.09$	Mg I		1
SDSS J1003−0031	$4.37 \pm 0.05$	Mg I, Na I		4
SDSS J1105+5006	$4.13 \pm 0.11$	Mg I, Na I		1
SDSS J1106+6737	$3.50 \pm 0.09$	Mg I, Ca I		1,2
SDSS J1113+2751	$3.18 \pm 0.09$	Mg I		1,2
SDSS J1143+6615	$> 20$		a	1,2
SDSS J1150+4533	$2.01 \pm 0.20$	Mg I, Na I		1
SDSS J1152+1605	$2.72 \pm 0.04$	Mg I, Na I		4
SDSS J1214−0234	$2.12 \pm 0.03$	Mg I, Na I		5
SDSS J1249+6514	$2.15 \pm 0.05$	Mg I		1
SDSS J1330+3029	$0.57 \pm 0.04$	Ca II, Fe I		6
SDSS J1412+2836	$1.99 \pm 0.10$	Na I		1
SDSS J1536+4205	$9.59 \pm 0.04$	Mg I, Na I		4,7
SDSS J1546+3009	$0.81 \pm 0.07$	Fe I		1
SDSS J1651+4249	$3.12 \pm 0.28$	Mg I, Na I	b	1
SDSS J2254+3031	$2.53 \pm 0.03$	Mg I, Na I		1,2
SDSS J2325+0448	$6.56 \pm 0.09$	Mg I		4
SDSS J2330+2956	$3.40 \pm 0.04$	Mg I, Na I		1,2

References: (1) This work/Hollands et al. (in preparation), (2) Kepler et al. (2016), (3) Schmidt et al. (2003), (4) Hollands et al. (2015), (5) Reid et al. (2001), (6) Dufour et al. (2006), (7) Kepler et al. (2015).

Notes: (a) Mg I and Na I lines are seen but splitting is not apparent. Rather they show quadratic Zeeman shifts of a few  $1000 \text{ km s}^{-1}$ , indicating a very high surface field. (b) Lines are broadened rather than completely split, however the subspectra suggest this white dwarf has a roughly 0.5 hr rotation period leading to smeared Zeeman lines in the coadded spectrum.

from DR9 onwards include additional absorption lines of Mg and Fe in this wavelength range, as predicted by the model spectra. However, while our models predicted further absorption features between 3000 and 3600 Å (particularly from Fe), they remained insufficient to explain the additional opacity required in the *u*-band.

To determine the source of ground-based UV opacity, we acquired spectra of 18 DZs with the William Herschel Telescope (WHT) down to 3000 Å using the Intermediate dispersion Spectrograph and Imaging System (ISIS). The observations were made during December 2013 and 2014, with a basic observing log given in Table 4. The same instrument setup was used on all nights. ISIS uses a dichroic beam splitter to separate the light onto two CCDs optimised for blue and red wavelengths. For the ISISB arm we used the R300B grating, and the 158R grating on the ISISR arm, with central wavelengths of 4300 Å and 7300 Å respectively. Using a 1.2" slit, this setup leads to spectral resolutions of about 5 Å in the blue arm and 9 Å in the red arm. For both CCDs we used  $2 \times 2$  binning to reduce readout noise.

For the 2013 observations we focused on obtaining bluer

**Table 4.** Observation log of WHT spectra. The observation date corresponds to the start of the night.  $t_{\text{exp}}$  is the total exposure time for each target.

SDSS J	Obs. date	$t_{\text{exp}}$ [s]	(Airmass)	Note
SDSS J0823+0546	28/12/2013	3000	1.09	a
SDSS J0116+2050	29/12/2013	2700	1.02	b,c
SDSS J0135+1302	29/12/2013	3000	1.12	c
SDSS J0512−0505	29/12/2013	2700	1.28	a
SDSS J0735+2057	29/12/2013	12600	1.09	c
SDSS J0916+2540	29/12/2013	3600	1.02	b
SDSS J1038−0036	29/12/2013	1800	1.22	b
SDSS J1214−0234	29/12/2013	3000	1.34	
SDSS J1330+3029	29/12/2013	1200	1.20	b
SDSS J1336+3547	29/12/2013	1800	1.13	b
SDSS J1535+1247	29/12/2013	1200	1.66	b
SDSS J0806+4058	23/12/2014	7200	1.05	c
SDSS J1043+3516	23/12/2014	4800	1.03	b
SDSS J1144+1218	23/12/2014	3300	1.05	b
SDSS J0143+0113	24/12/2014	2400	1.13	b,c
SDSS J0157+0033	24/12/2014	7200	1.19	b
SDSS J0741+3146	24/12/2014	9000	1.03	c
SDSS J0744+4649	24/12/2014	7200	1.19	c
SDSS J1152+1605	24/12/2014	6900	1.05	b,c

Notes: (a) Photometrically identified DZs, confirmed with these spectra. (b) Object appears in KGGD11. (c) Has at least one BOSS spectrum.

spectra of bright targets taken before the introduction of BOSS, and confirming two photometrically/astrometrically selected DZ candidates (Section 2.2). Thick cloud dominated the first half of December 28th, with some sporadic thin cloud during the remainder of the night. Therefore the only good quality data obtained was for SDSS J0823+0546 (taken during a clear part of the night). All other objects observed on the 28th were re-observed on the 29th with stable, clear conditions throughout the night. The flux calibration of spectra taken during 2013 was found to be excellent including for SDSS J0823+0546 (the only object successfully observed on December 28th).

For the 2014 observations we instead concentrated on obtaining improved spectra for objects where the existing SDSS spectra were poor, as well as following up some objects from SDSS DR10 with atypical spectra, e.g. SDSS J0744+4649. The first half of December 23rd was strongly affected by Saharan dust, only permitting observations in the second half of the night. On the 24th, while some small amount of dust still persisted in the air, it remained fairly stable throughout the night and so the flux calibration of objects taken on this night were found to be of reasonable quality.

Standard spectroscopic techniques were used to reduce the data with software from the *starklink* project. For each night multiple bias frames were combined to produce a master-bias image which was subtracted from each frame. Multiple flat fields were also taken per night, and co-added to produce a master-flat field. Images were then divided by the master-flat to remove pixel dependent variations. Extraction of 1-D spectra was performed using the optimal-extraction method via routines in the *pamela* package. Wave-



length and flux calibrations along with telluric removal were subsequently performed in *molly*<sup>3</sup>.

The flux calibration of SDSS J1144+1218 was strongly affected by the aforementioned dust. We corrected the spectrum by fitting the difference between synthetic magnitudes and SDSS photometry (in all SDSS filters) with a 3rd-order polynomial, providing a wavelength dependent correction. The calibrated spectra are shown in Figure 5 with their best fitting models (modelling discussed in Sections 4 and 5).

Comparison with the WHT spectra and model atmospheres revealed that the missing source of opacity came from lines of Ni and Ti. The missing lines were added to our line list used for calculation of DZ models described in the subsequent Sections of this paper.

#### 4 MODEL ATMOSPHERES

The methods and basic data for the calculation of model atmospheres and synthetic spectra are described in Koester (2010) and KGGD11. Atomic line data were obtained from the VALD (Piskunov et al. 1995; Ryabchikova et al. 1997; Kupka et al. 1999) and NIST databases (Kramida et al. 2016). Since many of the metal lines are extremely strong and have a significant influence on the atmospheric structure, we have included approximately 4500 lines not only in the calculation of synthetic spectra but also for the atmospheric structure calculation. The blanketing effect is very important and with every change of abundances new tables of the equation of state and absorption coefficients were calculated to obtain consistent results.

The strongest lines considered are the resonance lines H+K of Ca II (3968/3934 Å) and h+k of Mg II (2803/2796 Å). Although the latter are in the UV outside the range of the optical spectra, they still influence the models in the visible range. In KGGD11 we used approximate unified line profiles for these lines, but the quasi-molecular data – in particular dipole moments – were not available at that time. We have since calculated all missing data and redetermined the line profiles for this work.

##### 4.1 Ab-initio potentials and dipole moments for the Ca<sup>+</sup>He, Mg<sup>+</sup>He, and MgHe quasi-molecules

Ab-initio calculations were performed using the MOLCAS package (Aquilante et al. 2010). Electronic energies were calculated at the CASSCF (complete active space self-consistent field) level. Calculations of the dynamic electron correlation effects for the multiconfigurational CASSCF wave functions are based on the second order perturbation theory, the CASPT2 method in MOLCAS (Finley et al. 1998). The spin-orbit interaction energy was included using the state interaction program RASSI (restricted active space state interaction) in MOLCAS (Malmqvist et al. 2002). The RASSI program also calculates dipole moments of optical transitions between electronic states. Some details

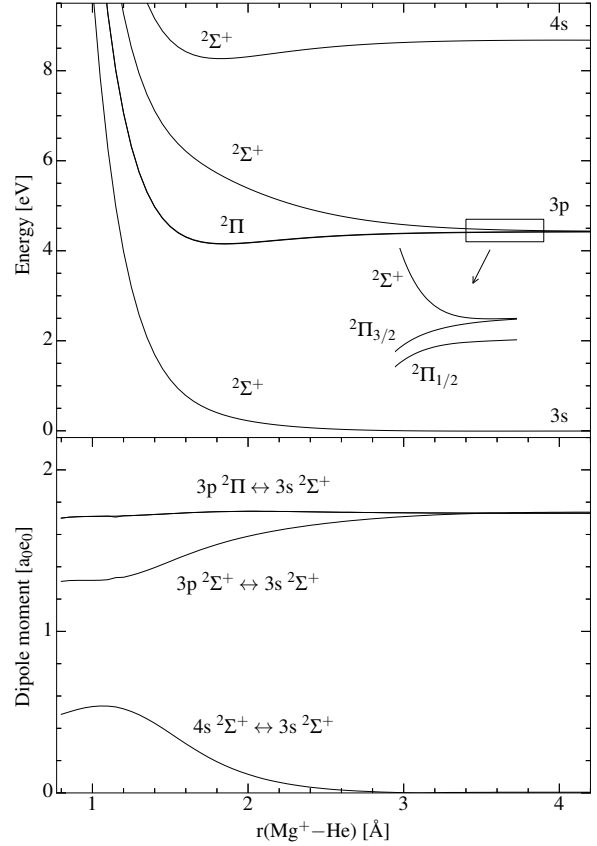


**Figure 6.** Potential energies (top) and dipole moments (bottom) for the Mg<sup>+</sup>He molecule. The resonance lines at 2796 and 2803 Å are the transitions from the 3s to the 3p states. The insert shows the small difference between the  $^2\Pi_{3/2}$  and  $^2\Pi_{1/2}$  states due to the spin orbit interaction. Likewise the corresponding dipole moments overlap on the larger scale.

on the results of the present calculations are given below.

**Mg<sup>+</sup>He:** The calculations included electronic states of Mg<sup>+</sup>He correlating with the ground  $2p^63s$  state and excited 3p and 4s states of the Mg<sup>+</sup> ion. Calculated potentials and dipole moment functions for some transitions are shown in Figure 6. The ground  $^2\Sigma^+$  state has a shallow potential well ( $D_e \approx 50 \text{ cm}^{-1}$ ,  $r_e \approx 3.5 \text{ Å}$ ). Interaction of Mg  $2p^63p$  with He gives  $^2\Pi_{1/2,3/2}$  states, and a  $^2\Sigma^+$  state. A slight difference between the  $^2\Pi_{1/2}$  and  $^2\Pi_{3/2}$  states is not seen in the plot scale. The dipole moment of  $3p \ ^2\Pi - 3s \ ^2\Sigma^+$  transitions is nearly constant. The  $3p \ ^2\Sigma^+$  state interacts with a higher lying  $4s \ ^2\Sigma^+$  state. Due to this interaction the dipole moment of the resonance  $3p \ ^2\Sigma^+ - 3s \ ^2\Sigma^+$  transition decreases (Figure 6). Calculations were performed using relativistic atomic natural orbital (ANO) type basis sets (Almlöf & Taylor 1987). The data shown in Figure 6 were obtained using

Mg.ano-rc. Roos.17s12p6d2f2g.9s8p6d2f2g  
He.ano-rc. Widmark.9s4p3d2f.7s4p3d2f

which are the largest ANO type basis sets in the MOLCAS basis set library. The accuracy of CASSCF/CASPT2 cal-

<sup>3</sup> *molly* software can be found at <http://www2.warwick.ac.uk/fac/sci/physics/research/astro/people/marsh/software>

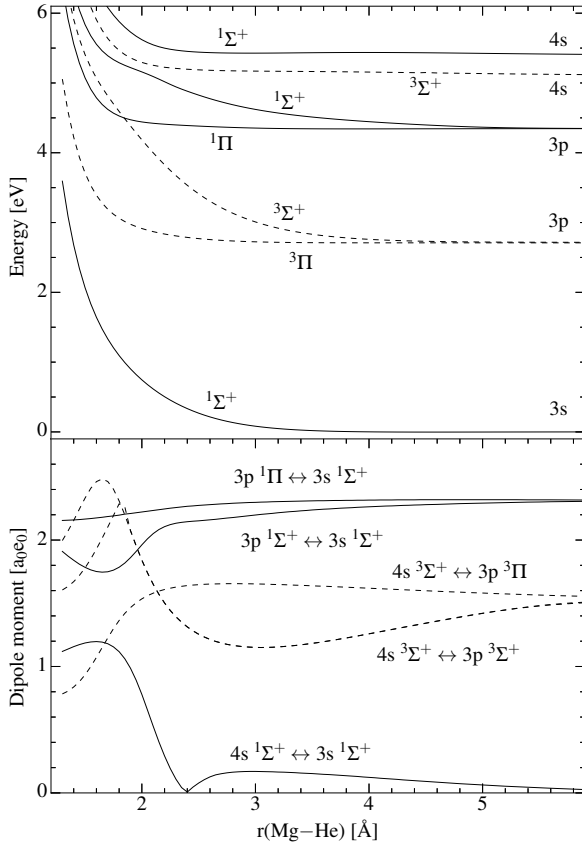


**Figure 7.** Potentials (top) and dipole moments (bottom) for the singlet (solid lines) and triplet (dashed lines) states of MgHe molecule.

culations with the ANO basis sets has been discussed in detail in [Roos et al. \(2004\)](#). Smaller ANO type basis sets for the He atom (VQZP and VTZP) were tested as well. The deviations from the results obtained with the largest basis sets (Figure 6) were found rather small (at least the differences would not be seen in the scale of Figure 6). For calculations of quasi-molecular bands corresponding to the  $3p\ ^2\Pi - 3s\ ^2\Sigma^+$  and  $3p\ ^2\Sigma^+ - 3s\ ^2\Sigma^+$  transitions, the asymptotic energies were adjusted to match the energies of the  $\text{Mg}^+(3p\ ^2P_{1/2,3/2})$  doublet.

The  $\text{Mg}^+\text{He}$  molecule has been the subject of several theoretical studies ([Monteiro et al. 1986](#); [Allard et al. 2016b](#)). Comparison of the present results with other studies is given in [Allard et al. \(2016b\)](#).

**MgHe:** The present calculations include electronic states of MgHe molecule correlating with the ground  $3p^6 4s^2$  and excited singlet and triplet  $4s4p$  and  $4s5s$  states of the Ca atom. Calculated potentials and dipole moments of some transitions are shown in Figure 7. The results were obtained with the same basis sets as for  $\text{Mg}^+\text{He}$  molecule.

The MgHe molecule was studied using ab initio methods by [Demetropoulos & Lawley \(1982\)](#) and very recently by [Leininger et al. \(2015\)](#) and [Allard et al. \(2016a\)](#). The latter study reports potentials and transition dipole moments only for the triplet  $3p\ ^3\Sigma^+$ ,  $3p\ ^3\Pi$ , and  $4s\ ^3\Sigma^+$  states. Comparison reveals close similarities with the present results including in particular crossing of  $4s\ ^3\Sigma^+ - 3p\ ^3\Sigma^+$  and  $4s\ ^3\Sigma^+ -$

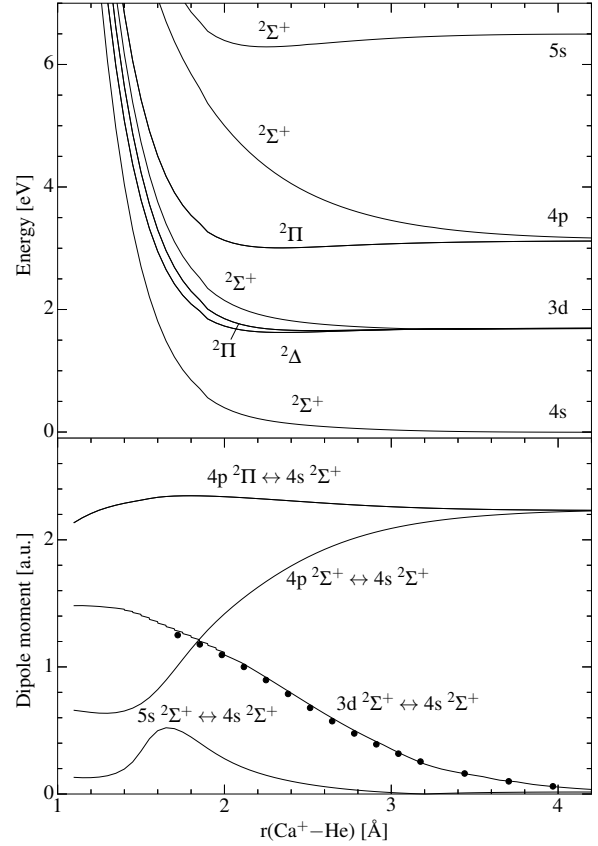


**Figure 8.** Potential energies (top) and dipole moments (bottom) for the  $\text{Ca}^+\text{He}$  molecule. The transitions for the Ca II H+K resonance lines are from the  $4s$  to the  $4p$  states. Some of the [Czuchaj et al. \(1996\)](#) results are shown by dotted lines for comparison.

$3p\ ^3\Pi$  transition dipole moment functions at  $r(\text{Mg}-\text{He}) \approx 2.2\text{ \AA}$  (dashed lines in lower part of Figure 7).

**$\text{Ca}^+\text{He}$ :** The present calculations include electronic states of  $\text{Ca}^+\text{He}$  molecule correlating with the ground  $3p^6 4s$  and excited  $3d$ ,  $4p$ , and  $5s$  states of the  $\text{Ca}^+$  ion. Potentials and dipole moments of some transitions calculated with the basis sets

Ca.cc-pV5Z.Peterson.26s18p8d3f2g1h.8s7p5d3f2g1h,  
He.cc-pV5Z.Dunning.8s4p3d2f1g.5s4p3d2f1g

are shown in Figure 8. The  $\text{Ca}^+\text{He}$  states correlating with  $3d\ ^2D_{3/2,5/2}$  are metastable. The  $3d\ ^2\Delta_{3/2,5/2}$  and  $2\Pi_{1/2,3/2}$  states are weakly bound ( $D_e \leq 400\text{ cm}^{-1}$ ) and  $3d\ ^2\Sigma^+$  is strongly repulsive. Due to interaction between  $3d\ ^2\Sigma^+$  and  $4p\ ^2\Sigma^+$  states, the asymptotically forbidden  $3d\ ^2\Sigma^+ - 4s\ ^2\Sigma^+$  transition acquires a considerable dipole moment as  $r(\text{Ca}^+-\text{He})$  decreases (figure 8). In turn, the dipole moment of the resonance  $4p\ ^2\Sigma^+ - 4s\ ^2\Sigma^+$  transition decreases ([Czuchaj et al. 1996](#)).

The  $\text{Ca}^+\text{He}$  molecule has been the subject of several theoretical studies ([Giusti-Suzor & Roueff 1975](#); [Monteiro et al. 1986](#); [Czuchaj et al. 1996](#)). Line profiles of Ca II H+K resonance lines perturbed by He calculated with the present potentials and transition dipole moments have been discussed in [Allard & Alekseev \(2014\)](#).

## 4.2 Unified line profiles

For the calculation of line profiles we used the semi-classical unified theory as described in [Allard & Kielkopf \(1982\)](#) and many later papers by Allard and coworkers. In particular we use the concept of the “modulated dipole” as developed in [Allard et al. \(1999\)](#), which takes into account the change of the transition probability with emitter-perturber distance, as well as the modification of perturber densities through the Boltzmann factor, depending on the interaction potential. For this work we need profiles extending to more than 1000 Å from the line centre; in a unified theory, which aims to describe the line core and far wing simultaneously this needs profiles extending over a dynamic range of 12 and more orders of magnitude. This required a complete rethinking and reimplementation of all algorithms for the calculation of the auto-correlation function and Fourier transforms; while the physics is taken unchanged from the papers cited above the numerical code was completely rewritten. Improved algorithms and numerous small changes now allow us to cover the profile over more than 10 orders of magnitude without excessive noise and artefacts. We mention only one of the more significant improvements: the calculation of the one-perturber correlation function (see [Allard & Kielkopf 1982](#)) involves integrals of the type

$$\int V(x) \sin(2\pi x) dx, \quad (2)$$

where  $V$  is slowly varying and the  $\sin$  a rapidly oscillating function. By replacing  $V(x)$  over small intervals with a linear approximation the integral can be calculated analytically, avoiding the greatest source of noise in previous calculations.

Line profiles calculated with these new algorithms were used for the resonance lines of Ca II and Mg II.

After the bulk of this project was complete, new calculations for the Mg I triplet 5168/5174/5185 Å were presented by [Allard et al. \(2016a\)](#). Using atmospheric parameters from KGGD11 ( $T_{\text{eff}} = 6000$  K) they show a reasonable fit to the Mg I triplet in SDSS J1535+1247. Our fits to this object with the KGGD11 parameters and also with the new value  $T_{\text{eff}} = 5770$  K were of similar quality with our first calculated line profile tables. This table had a spacing of logarithmic perturber density of 0.5 dex, with a high end at 21.0, 21.5, 22.0. When analysing the structure of the atmosphere, we realised that the logarithmic neutral perturber density was close to 22 already near  $\tau_{\text{Rosseland}} = 2/3$ , and much of the line profile was formed at densities larger than 21. As can be seen in Figure 3 of [Leininger et al. \(2015\)](#) the maximum absorption changes very rapidly with increasing perturber density, moving to the blue of the central wavelength. To better describe the line profile we calculated new profile tables with a finer spacing (0.2 dex) of the log density between 21 and 22. With these tables, the calculated profiles did not fit the spectrum, but showed the maximum absorption far to the blue of the low density maximum. As we do not know the details of the calculations in [Allard et al. \(2016a\)](#), we cannot explain the differences. However, we note that the conditions for this triplet in this object are close to or possibly beyond the limits of the unified theory as discussed in [Allard & Kielkopf \(1982\)](#) (e.g. eqs. 106, 108). Because of these current uncertainties for the Mg I triplet we have decided to use the interpolation algorithm of [Walkup et al. \(1984\)](#), already used and described in KGGD11, which

gives a reasonable fit. The same method was also used for other medium strong lines with notable asymmetries.

## 5 ATMOSPHERIC ANALYSIS

The process of fitting the white dwarfs in our sample is made difficult by both the complexity of the emergent flux and the practical challenge of dealing with the various systematics which affect the SDSS spectra.

Typically one begins the analysis of white dwarf spectra by fitting of the model spectrum to the data at some chosen – preferably line free – continuum regions. Atmospheric parameters are then obtained by fitting to only absorption lines. Such a procedure removes the effects of interstellar reddening and poor flux calibration, allowing for precise estimation of  $T_{\text{eff}}$  and  $\log g$  for DA and DB stars. For the cool DZ stars in our sample, the intense line blanketing at wavelengths below  $\simeq 5500$  Å results in no clearly defined continuum. We therefore chose to work with the flux-calibrated spectra for the fitting of our atmospheric models. However, the flux calibration accuracy for some of the spectra still presented a major hurdle.

The SDSS spectra obtained using the original spectrograph (released DR1–DR8) show very good flux calibration as synthetic  $g$ ,  $r$ , and  $i$  magnitudes calculated from these spectra agree well with SDSS photometry. This has previously been investigated in great detail by [Genest-Beaulieu & Bergeron \(2014\)](#), who reach a similar conclusion. In general, flux calibrations taken by the newer BOSS spectrograph from DR9 onwards (most of the new objects in this work were observed using BOSS) are typically much lower in quality for two reasons. Firstly, for objects targeted as QSO candidates, the BOSS flux calibration is purposely incorrect. To improve sensitivity for the Ly- $\alpha$  forest of quasars, the fibers are offset in the bluewards direction of atmospheric dispersion ([Dawson et al. 2013](#)). These offsets were not applied for the flux calibration fibers, which are centred at 5400 Å, and so QSO targets have spectra which appear too blue. Because our DZ sample overlaps the colour-space of quasars, many of the white dwarf spectra are affected by this issue. In principle this can be rectified as DR13 provides post-processing corrections for BOSS flux calibrations according to the procedure of [Margala et al. \(2015\)](#). However, high proper-motions (median value of 60 mas yr<sup>−1</sup>, and maximum of 600 mas yr<sup>−1</sup> for our sample) lead to a second source of systematic error resulting in unreliable flux calibrations. The spectroscopic fibers (2 arcsec in diameter for BOSS), are placed according to positions obtained via SDSS imaging, taken up to and including DR7. Therefore significant displacement of sources between photometric and spectroscopic observations results in further calibration error of spectral fluxes.

Since the fitting of our model atmospheres requires fairly good flux calibration we apply a simple correction to affected spectra. The BOSS spectrograph fully covers the wavelengths of the SDSS  $g$ ,  $r$ , and  $i$  filters, allowing us to calculate synthetic magnitudes in these bands. The differences between the SDSS and synthetic magnitudes against their effective wavelengths are then fitted with a first order polynomial (including uncertainties on both the SDSS and synthetic photometry). Converting the fit

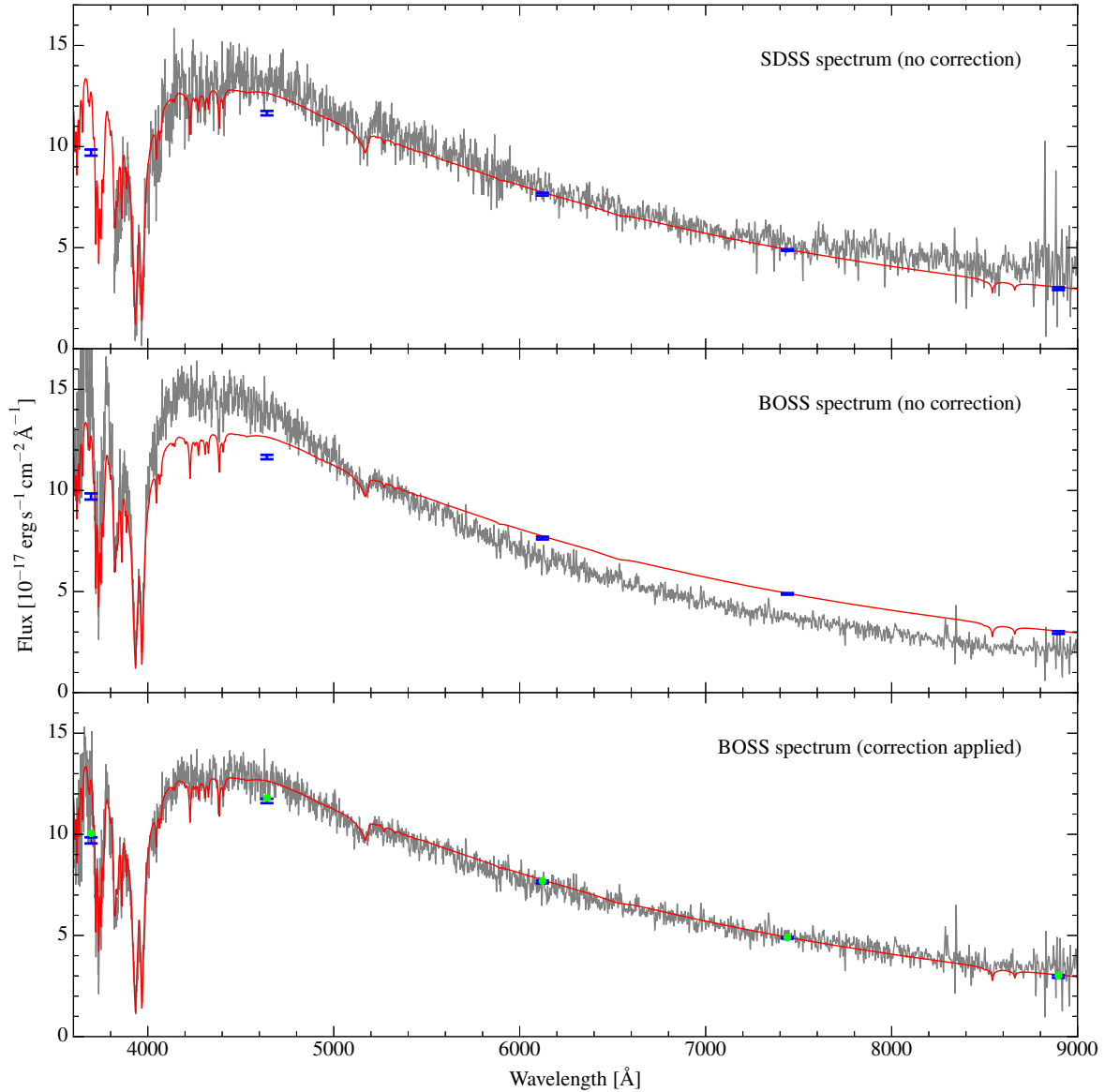


**Figure 9.** The pre-BOSS spectrum of SDSS J1058+3143 (top) is seen to match the SDSS photometry (blue points). The BOSS spectrum with its original flux calibration (middle) overestimates flux at blue wavelengths, and underestimates it at red wavelengths. Applying our corrective procedure to the BOSS spectrum (bottom) effectively removes the distortion to the flux calibration. In all panels our best fitting model is shown in red. In the bottom panel the model’s synthetic magnitudes are also displayed (green) showing the close agreement in all bands when fitting to the corrected spectra. Displayed spectra are smoothed with a 3-point boxcar for clarity. The *u*-band points are placed redwards of their effective wavelength (3595 Å) in order to appear within the bounds of the figure.

from magnitudes to spectral flux units provides a wavelength dependent correction, which we multiply with the original spectrum. Iterating this procedure three times ensures good agreement of the spectrum with its *g*, *r*, and *i* magnitudes. To demonstrate the effectiveness of this procedure, one system, SDSS J1058+3143, is shown in Figure 9 with both its SDSS and BOSS spectra. The BOSS spectrum is distorted by the original flux calibration, but is seen to agree well with photometry following our correction. In cases like SDSS J1058+3143 where BOSS and SDSS spectra were available, it was usually preferable to use the corrected BOSS spectra (unless the BOSS spectra were of very low

quality) as these go to bluer wavelengths ( $\simeq 3600$  Å versus  $\simeq 3800$  Å for the original spectrograph), covering additional spectral lines, in particular Mg and Fe. The SDSS spectrum that fitting was performed on is given in the plate-MJD-fiber column in appendix Table A1.

To model the corrected spectra, we first made zeroth order estimates by fitting a grid of DZ models, spanning a wide range in  $T_{\text{eff}}$  and metal abundances (the same model grid described in Section 2.1.2).  $T_{\text{eff}}$  is varied from 4400 to 14000 K in 200 K steps, and  $\log[\text{Ca}/\text{He}]$  from  $-10.5$  to  $-7.0$  in 0.25 dex steps. All other elements are held at bulk Earth abundances relative to Ca, and the  $\log g$  is set to 8.0 in all



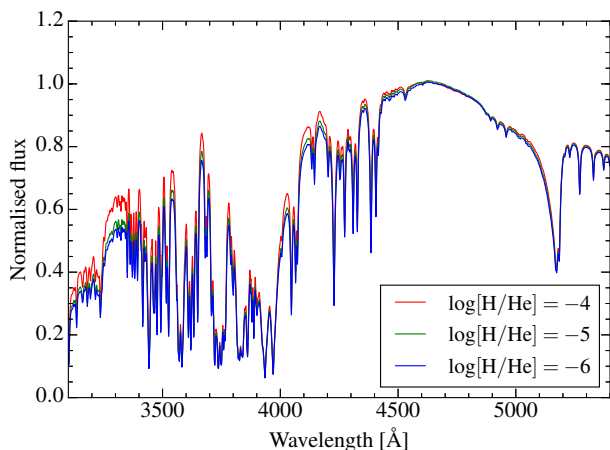


**Figure 10.** The best fitting model for SDSS J1336+3547 is shown in red. The green and blue models are recomputed at decreased hydrogen abundances with all other atmospheric parameters held constant. No discernible change is seen for abundances below  $\log[\text{H}/\text{He}] = -6$ . Normalisation is with respect to the  $\log[\text{H}/\text{He}] = -4$  model.

cases. The  $\chi^2$  between each grid point and the target spectrum was calculated. The grid of  $\chi^2$  values was then fit with a bi-cubic spline to estimate the location of minimum  $\chi^2$  in the plane of  $T_{\text{eff}}$  and Ca abundance, and the corresponding parameters were then used as a starting point for a detailed fit. From this point, parameters in the model were manually iterated in small steps (typically 100 K or less in  $T_{\text{eff}}$  and 0.05–0.3 dex for abundances), until satisfactory agreement between spectrum and model was found.

Two caveats to our fits are that they are performed at a fixed  $\log g$  of 8, and unless in obvious disagreement with the data, at a fixed hydrogen abundance of  $\log[\text{H}/\text{He}] = -4$  dex. Here we discuss the effect of these caveats on our parameter estimation.

Firstly we note that it is not possible to estimate surface gravities from the spectra of cool helium atmosphere white dwarfs, as the effect of changing  $\log g$  on the emergent spectrum can generally be compensated by adjustment of the other model parameters. In other words  $\log g$  is strongly correlated with the other atmospheric parameters, and so increases the uncertainties in the parameters derived from our fits compared with those at a fixed value  $\log g = 8.0$ . We attempted to quantify the effect of  $\log g$  on our uncertainties, by refitting SDSS J1535+1247 at multiple  $\log g$  values and examining the shift in  $T_{\text{eff}}$  and abundances. Genest-Beaulieu & Bergeron (2014) find the SDSS spectroscopic  $\log g$  distribution to have a standard deviation of 0.2 dex. We therefore repeated our fits to SDSS J1535+1247 at  $\log g = 7.8$  and 8.2. We found that a 0.2 dex increase in  $\log g$  leads to 75 K increase in  $T_{\text{eff}}$ , and 0.19 dex increases in abundances, with the opposite effects for a 0.2 dex decrease. Fortunately, because all abundances correlate with  $\log g$  to the same degree, abundance ratios are minimally effected. Therefore using a fixed  $\log g$  value will not significantly impact the investigation of accreted body compositions (Paper II).

By default hydrogen abundances were set to  $\log[\text{H}/\text{He}] = -4$  dex in our models, as we do detect

trace hydrogen at this level (and higher) in several of the brightest systems. This value of  $-4$  dex was only adjusted if the models showed departure from the data and hence we report hydrogen abundances only in those cases. The presence of trace hydrogen does increase the electron density within the atmosphere slightly and so, in principle, modifies the metal line profiles compared with a hydrogen deficient atmosphere. However, we demonstrate in figure 10 that this effect is negligible, where we decrease the hydrogen abundance from  $\log[\text{H}/\text{He}] = -4$  to  $-6$  dex with all other atmospheric parameters held constant for the system SDSS J1336+3547. For transitions such as the Ca H+K lines, Ca I 4228 Å line, and the Mg-b blend ( $\simeq 5170$  Å) the difference between line profiles is small enough as to be undetectable even in the highest quality spectra presented in this work. The largest difference is seen at blue wavelengths between 3000 Å and 4500 Å, where the continuum flux can be 15 percent greater at  $-4$  dex than at  $-6$  dex. However, for the majority of spectra the signal-to-noise ratio at these wavelengths is so low (typically between 2 and 6) that the effect of a fixed hydrogen abundance does not affect our fits.

Generally the  $\chi^2$  between data and models served only as an indicator of fit quality. Direct  $\chi^2$  minimization did not necessarily correspond to the *best* fit as, for instance, any remaining flux calibration error (higher order than our corrections could account for) could dominate the residuals in the fit. Additionally, residuals are affected where the wings of line profiles still require further theoretical improvement. For example the blue wing of the Mg I b-blend at  $\simeq 5170$  Å, does not always fit the data well, particular for the lowest temperatures in our sample. In this situation, we found an adequate solution was to match the equivalent widths between model and spectrum (as well as fitting other Mg features), which does not correspond to  $\chi^2$  minimization.

For a few of the brightest objects where the flux calibration is considered to be exceptionally good, in particular those where we have WHT spectra (SDSS J0116+2050, SDSS J0512–0505, SDSS J0741+3146, SDSS J0744+4649, SDSS J0823+0546, SDSS J0806+4058, SDSS J0916+2540, SDSS J1043+3516, SDSS J1144+1218, and SDSS J1535+1247), direct  $\chi^2$  minimization was considered to be appropriate. Even so, in some cases where line widths between model and spectrum are not in exact agreement (e.g. the Mg I line of SDSS J0512–0505), a better fit was achieved by manually updating some parameters following the least-squares fit.

The atmospheric parameters derived from our fits are given in appendix Table A2. The final models are shown with their corresponding spectra in appendix Figures B2 to B12. Where we obtained WHT spectra, the models are also shown in Figure 5.

From the fit parameters we also derive convection zone masses and diffusion timescales for each element. For this purpose we calculated the convection zone sizes and diffusion timescales for the same grid of models described before in terms of  $T_{\text{eff}}$  and Ca abundances<sup>4</sup>. These were then bi-

<sup>4</sup> for detailed discussion on these envelope calculations see Koester & Wilken 2006 and Koester 2009 with the most up to

linearly interpolated to estimate diffusion rates and convection zone sizes.

Uncertainties are difficult to estimate from these fits. For the 10 objects mentioned above that we fitted via a least-squares routine, the reported errors on  $T_{\text{eff}}$  are typically a few K, and for abundances a few 0.01 dex. As these are purely statistical errors they are far too small and fail to account for systematic uncertainty. Even for the very best spectra, we believe the errors on  $T_{\text{eff}}$  are measured to no better than 50 K (where systematic uncertainty dominates), but can be as large as 400 K for the noisiest spectra. To estimate the error on  $T_{\text{eff}}$  ( $\sigma_T$ ) on a per-object basis, we combine the aforementioned systematic and statistical variances producing the simple relation

$$\sigma_T^2 = (50 \text{ K})^2 + \left( \frac{T_{\text{eff}}}{5 \text{ SN}} \right)^2. \quad (3)$$

The statistical component of  $\sigma_T$  (right-hand term) is assumed to be proportional to  $T_{\text{eff}}$  divided by the median spectral signal-to-noise ratio between 4500 and 5500 Å (SN). The scaling factor of 5 was chosen to give the expected distribution of errors as described above. The  $\sigma_T$  calculated from equation (3) are included in appendix Table A2, and are used for error propagation in Section 8.

Uncertainties on abundances are dependent on the element, the line strengths, and the spectral signal-to-noise ratio. We estimate these are typically in the range 0.05–0.3 dex from adjustment of the abundances in the models in comparison with the data. Ca is in general the most well measured element due to the large oscillator strengths of the H+K lines, which remain visible over the entire  $T_{\text{eff}}$  range of objects in our sample.

For the fitting described throughout this section, we assumed that interstellar reddening has a minor effect on the spectra, as these faint stars are within are estimated to lay within a few hundred parsecs from the Sun (see Section 8), and the SDSS footprint avoids the Galactic plane. We show this assumption to be reasonably justified, given the already moderate uncertainties for the more distant, and hence most affected systems. For each object, we calculated the maximum possible reddening along its line of sight using the [Schlegel et al. \(1998\)](#) Galactic dust map, and found the maximum  $E(B - V)$  values to have a median of 0.029. For three nearby, bright systems (SDSS J0116+2050, SDSS J1043+3516, and SDSS J1535+1247) which span a variety of  $T_{\text{eff}}$  and can be safely considered unreddened, we applied an artificial reddening of  $E(B - V) = 0.029$  and refit the spectra to quantify the effect.

We found the typical effect on  $T_{\text{eff}}$  to be a decrease of  $\simeq 130$  K, and abundances decreasing by  $\simeq 0.1$  dex. While this is comparable to our estimated errors for the brightest systems, for the more distant objects, where reddening reaches its maximum, our estimated  $T_{\text{eff}}$  and abundance uncertainties exceed the systematic effect from reddening. We therefore conclude that reddening does not significantly affect our results, due to the intrinsic faintness of these low  $T_{\text{eff}}$  objects. For white dwarfs hotter than 12000 K ([Genest-Beaulieu & Bergeron 2014](#)), reddening cannot be neglected

as high quality data can be obtained out to many hundreds of parsecs.

One exception in our sample is SDSS J0447+1124, which was observed in SDSS stripe 1374. This star has a maximum  $r$ -band extinction of 1.3 mag, and maximum  $E(B - V) = 0.47$ . Therefore our parameter estimates for this object should be treated with an appropriate degree of skepticism.

## 6 COMPARISON WITH OTHER DZ SAMPLES

Our sample of DZ white dwarfs focuses on high metallicities at low  $T_{\text{eff}}$ . We have compared our work with that of [Dufour et al. \(2007\)](#) and [Koester & Kepler \(2015\)](#), who investigated metal pollution in warmer helium atmosphere white dwarfs.

[Koester & Kepler \(2015\)](#) carried out a systematic analysis of 1107 DB stars in SDSS, and as part of that work measured Ca abundances. The authors obtained firm measurements of  $\log[\text{Ca}/\text{He}]$  for 77 objects in their sample, and upper limits for the remaining stars. These 77 DBZ span 11 000–18 000 K in  $T_{\text{eff}}$ .

The Dufour sample consists of 146 DZ white dwarfs with  $T_{\text{eff}}$  of 6000–12 000 K. One additional system (plate-MJD-fiber = 0301-51942-0030) is reported at  $T_{\text{eff}} = 4600$  K, however inspection of its spectrum shows this to be a K-type main-sequence star and we therefore remove it from our comparison. As this sample is intermediate in  $T_{\text{eff}}$  with respect to our sample and that of [Koester & Kepler \(2015\)](#), there is some minor overlap. One system is common to [Koester & Kepler \(2015\)](#) and [Dufour et al. \(2007\)](#), and four systems from [Dufour et al. \(2007\)](#) appear in our work (SDSS J0956+5912, SDSS J1038–0036, SDSS J1112+0700, SDSS J1218+0023). For these five stars we adopt the parameters from [Koester & Kepler \(2015\)](#) and our analysis here.

The minimal overlap between the samples is unsurprising. As [Koester & Kepler \(2015\)](#) and [Dufour et al. \(2007\)](#) search for DB(Z)s and DZs respectively, the presence of He lines in the SDSS spectra set apart these two samples. The *maximum*  $u - g$  colour-cut adopted by [Eisenstein et al. \(2006\)](#) (from which the DZs in [Dufour et al. \(2007\)](#) were selected), is only slightly higher than our *minimum*  $u - g$  colour-cut (see Section 2.1.2), and so as expected there are only a few objects common to both our sample and that of [Dufour et al. \(2007\)](#).

The distribution of these three samples in  $\log[\text{Ca}/\text{He}]$  vs.  $T_{\text{eff}}$  are displayed in Figure 11. Prominent upper and lower boundaries are observed for the combined distribution, with the objects from [Dufour et al. \(2007\)](#) joining smoothly with the other two samples. The lower bound simply reflects the detection limit for Ca as a function of  $T_{\text{eff}}$  in He dominated atmospheres, and thus has no physical interpretation. For systems with lower Ca abundances than this bound, only upper limits can be obtained. The upper boundary of the distribution contains significant structure which was not expected. For the DBZs in the [Koester & Kepler \(2015\)](#) sample and the warmest DZs of the [Dufour et al. \(2007\)](#) sample, the maximum observed  $\log[\text{Ca}/\text{He}]$  is seen to decrease with decreasing  $T_{\text{eff}}$ , reaching a minimum of  $\simeq -9$  dex between 10 000 K and 11 000 K.

At  $\simeq 10 000$  K, maximum Ca abundances are seen to

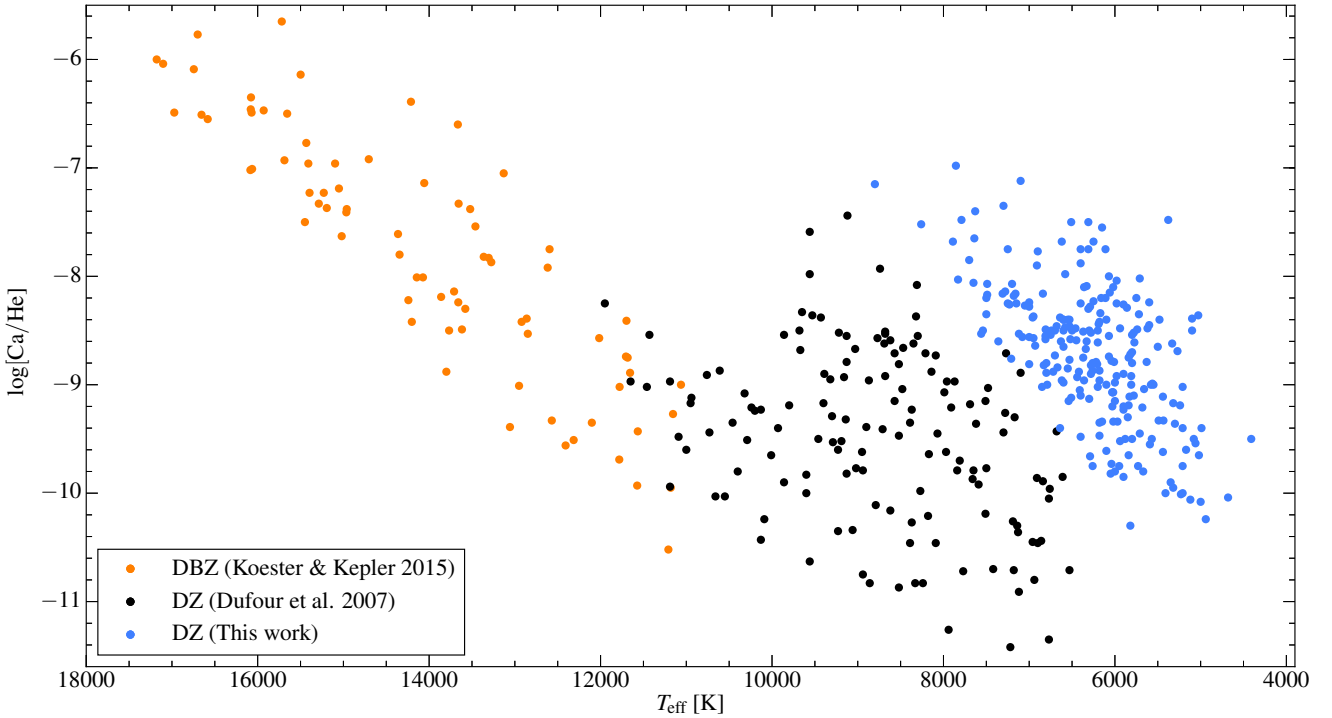


**Figure 11.** Atmospheric Ca abundances against  $T_{\text{eff}}$  for our DZ sample along with the DBZ/DZ samples of [Koester & Kepler \(2015\)](#) and [Dufour et al. \(2007\)](#).

rapidly increase by more than an order of magnitude over a narrow  $T_{\text{eff}}$  range, merging smoothly into our DZ distribution (blue points) where the maximum Ca abundances reach  $\simeq -7$  dex at about 8000 K. Interestingly, the [Dufour et al. \(2007\)](#) DZ sample appears to show both these effects.

Noticing the downwards trend within their DBZ sample, [Koester & Kepler \(2015\)](#) converted Ca abundances to accretion rates by considering the  $T_{\text{eff}}$ -dependence of the convection zone masses and Ca diffusion timescales (see their Figures 4, 10, and 11). The  $T_{\text{eff}}$ -dependence of the maximum Ca accretion rates remained in the resulting distribution, yet the authors note that no such trend is seen for DAZ white dwarfs over the same  $T_{\text{eff}}$  range ([Koester et al. 2014](#)). Because there is no reason to think the range of accretion rates should differ between hydrogen and helium atmosphere white dwarfs, [Koester & Kepler \(2015\)](#) concluded an incomplete understanding of deep convection zone formation may be responsible.

This decrease in  $\log[\text{Ca}/\text{He}]$  persists down to  $\simeq 10\,000$  K in the DZ sample of [Dufour et al. \(2007\)](#), demonstrating that it is not sensitive to differences in the input physics and numerical methods in the two different atmospheric codes.

The sharp increase in Ca abundances by two orders of magnitude between 10 000–8000 K seen in the [Dufour et al. \(2007\)](#) DZ sample before merging smoothly into our own sample suggests either a rapid decrease in convection zone sizes, an increase in diffusion timescales, or some combination of these two factors.

A further downwards trend in  $\log[\text{Ca}/\text{He}]$  is seen in the upper envelope of the blue points in Figure 11 from 4000 K <

$T_{\text{eff}} < 9000$  K. We address this in Paper II due to its specific relevance to remnant planetary system evolution.

## 7 HYDROGEN ABUNDANCES

The origin of trace hydrogen at white dwarfs with helium-dominated atmospheres is not fully understood, with proposed explanations including a primordial origin or accretion from the interstellar medium ([Bergeron et al. 2015](#); [Koester & Kepler 2015](#)), however an alternate hypothesis includes the accretion of water rich planetesimals. Oxygen excesses identified at the metal-polluted white dwarfs GD 61 ([Farihi et al. 2013](#)) and SDSSJ124231.07+522626.6 ([Raddi et al. 2015](#)), indicate that these systems must have accreted water-rich material as only partial fractions of their respective oxygen budgets could be associated with the other detected elements in the form of metal-oxides. Both [Farihi et al. \(2013\)](#) and [Raddi et al. \(2015\)](#) therefore suggested that the trace hydrogen present in the helium-dominated atmospheres of GD 61/SDSSJ124231.07+522626.6, could be explained by accretion of water-rich material. Furthermore, Gentile Fusillo et al. (submitted) find evidence that trace hydrogen is correlated with the presence of metals, potentially strengthening the argument for water accretion as the solution to DB white dwarfs with trace hydrogen. From a theoretical perspective, [Veras et al. \(2014b\)](#) found that hydrogen delivery from exo-Oort cloud comets is dynamically possible, and could provide the necessary hydrogen on Gyr timescales to explain observations.

Unlike metals which sink out of the white dwarf convec-

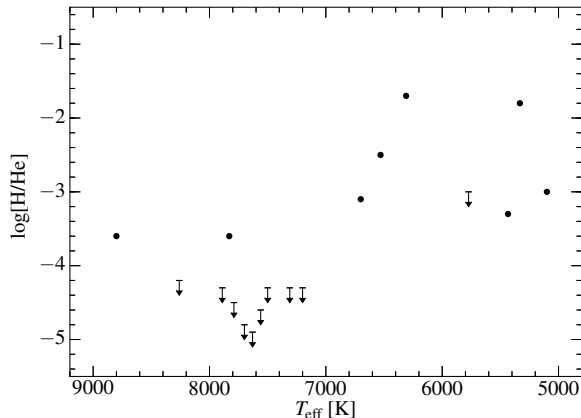


**Figure 12.** Hydrogen abundance as a function of  $T_{\text{eff}}$ . Firm measurements are indicated by dots, whereas arrows correspond to upper limits only. Hydrogen abundance uncertainties are estimated to be typically around 0.3 dex.

tion zone, hydrogen remains suspended indefinitely, thus observed abundances would correspond to the total mass from multiple accretion events, integrated over the cooling age of the white dwarf. This suggests that DB white dwarfs with trace hydrogen (but no metal contamination), may have accreted planetesimals in the past, but with the hydrogen as the only remaining evidence of such accretion events.

While not the focus of this work we do obtain hydrogen abundances and upper limits thereof for a handful of objects in our sample. As described in Section 5, we only attempted to constrain hydrogen abundances in our atmospheric modelling if there we found an obvious discrepancy between the model and observed spectra, where the default abundance was set to  $\log[\text{H}/\text{He}] = -4$  dex. One possibility was that the model showed a hydrogen line which was not present in the data, in which case an upper-limit estimation is made. These upper-limits depend both on the white dwarf  $T_{\text{eff}}$  and also the S/N of the spectrum. In the cases where the measurement is *not* an upper-limit, the detection may either correspond to an  $\text{H}\alpha$  detection or an increased hydrogen abundance may have been necessary to replicate the spectrum. For white dwarfs too cool to display  $\text{H}\alpha$  the presence of hydrogen still contributes significantly to the electron-pressure in the atmosphere. The resulting increase in atmospheric opacity leads to both a narrowing of the metal lines and a redder continuum, for a given  $T_{\text{eff}}$  and metal abundances. In principle this additional electron pressure may arise from elements other than hydrogen, e.g. sulfur, but because hydrogen is typically present at abundances orders of magnitude higher than metals, it is a reasonable assumption that hydrogen is the principal donor of additional electrons.

All objects where we were able to constrain hydrogen abundances are displayed in Figure 12. Additionally the spectrum of SDSS J0150+1354 which has the largest H abundance in our sample ( $\log[\text{H}/\text{He}] = -1.7$  dex) is shown in Figure 13, demonstrating the clear  $\text{H}\alpha$  detection, and narrow Mg I and Na I lines, even with a cool  $T_{\text{eff}}$  of 6300 K.

Our sample shows a clear increase in trace hydrogen towards lower  $T_{\text{eff}}$  within Figure 12. Above 7000 K, (cooling age of 1.5–2.0 Gyr), no objects are found with  $\log[\text{H}/\text{He}] >$

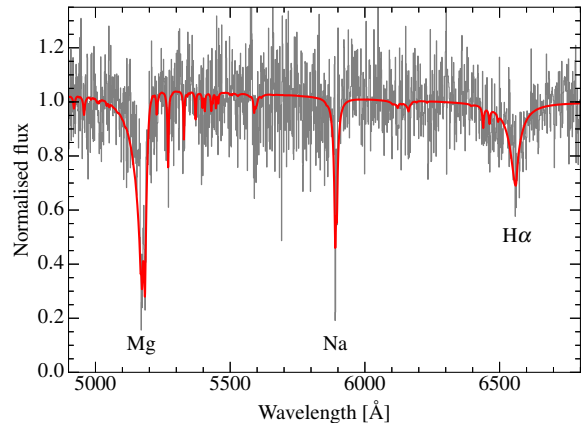


**Figure 13.** Normalised spectrum and best fit model to SDSS J0150+1354, demonstrating the large hydrogen abundance for this cool object. Strong lines are labelled.

–3 dex. Naively one may be inclined to think Figure 12 provides a strong case for trace hydrogen increasing with cooling age, however this is not the case. If hydrogen accumulation occurred at a constant rate then the inferred hydrogen masses diluted within the white dwarf convection zone should increase linearly with time. The distribution of temperatures in Figure 12 corresponds to cooling ages of about 1–6 Gyr (calculation of cooling ages is discussed in Section 8), or about 0.8 dex in the logarithm of cooling ages. As convection zone sizes (see appendix Table A3) are not calculated to change more than about 0.3 dex over the range of the plot, a constant rate of hydrogen accumulation cannot explain the  $\approx 2$  dex increase in abundance observed between the objects above and below  $T_{\text{eff}}$  of 7000 K in Figure 12.

It is much more plausible that this represents a selection bias related to our colour-cut. For instance, the white dwarf SDSS J1038–0036 has  $T_{\text{eff}} = 7700$  K and hydrogen upper-limit of  $\log[\text{H}/\text{He}] \leq -4.8$  dex from our spectroscopic fit. Recalculating the model spectrum with  $\log[\text{H}/\text{He}] = -2$  dex (and all other atmospheric parameters kept the same) results in flux redistribution towards blue wavelengths. This changes the  $u - g$  colour from 0.71 to 0.42 which falls outside of the colour-cut described in Section 2.1.2. It may well be the case that objects do exist with  $T_{\text{eff}} > 7000$  K and  $\log[\text{H}/\text{He}] > -3$  dex, but because of their blue colours, are absent in our sample.

The larger number of objects with  $\log[\text{H}/\text{He}]$  upper-limits for  $T_{\text{eff}} > 7000$  K is also a selection effect. Hotter objects are naturally brighter and thus more likely to have high S/N spectra. Additionally the strength of the  $\text{H}\alpha$  line increases with increasing  $T_{\text{eff}}$  and so observed spectra where  $\log[\text{H}/\text{He}]$  is noticeably less than the default model value of –4 dex are more likely to be identified. Conversely, below  $T_{\text{eff}}$  of 7000 K spectra become noisier,  $\text{H}\alpha$  lines become weaker, and so typically no visible disagreement is seen for  $\log[\text{H}/\text{He}] = -4$  dex.

None of the above is to say that trace hydrogen is unrelated to the accretion of water-rich objects, simply that the higher abundances seen for the cooler objects in Figure 12 *do not* indicate a time-dependent increase. In conclusion, these results neither favour nor rule out any of the hypotheses for



the source of trace hydrogen at white dwarfs with helium dominated atmospheres, i.e. water-rich planetesimals, ISM accretion, or a primordial origin.

## 8 SPATIAL DISTRIBUTION AND KINEMATICS

The calculation of model spectra for a given set of atmospheric parameters ( $T_{\text{eff}}$ ,  $\log g$ , chemical abundances), yields the emergent spectrum per unit area of the stellar surface. Given the radius of the white dwarf, the absolute spectral flux density can be calculated, which when compared with observational data can be used to infer the distance to the star. We estimate the distances to the DZ stars in our sample propagating the relevant uncertainties via a Monte-Carlo method.

White dwarf radii are a function of both mass and to a much lesser extent  $T_{\text{eff}}$ , however we have no direct spectral constraint on the masses of our white dwarf sample. Instead, we used the SDSS mass distribution (Kepler et al. 2015) as a prior on the white dwarf mass, and the uncertainties on  $T_{\text{eff}}$  from appendix Table A2. These were then propagated through a grid of DB cooling models<sup>5</sup> (Bergeron et al. 2001; Holberg & Bergeron 2006; Kowalski & Saumon 2006; Bergeron et al. 2011) to calculate posterior distributions on radii. We then calculated synthetic absolute  $r$ -band magnitudes from the best-fit models propagating uncertainties from the radii and  $T_{\text{eff}}$ . Finally, distance-moduli and hence distances were determined from the SDSS  $r$ -band photometry.

We acknowledge that our distance calculations are not entirely free from bias. Firstly we do not account for interstellar extinction. The SDSS footprint avoids the Galactic plane, minimizing extinction effects, however the most distant stars at a few hundred pc may suffer a small amount. Using the Galactic dust map of Schlegel et al. (1998) we determined the *maximum* extinction possible for each object in our sample, and found a median value of 0.08 mag in the  $r$ -band. For the furthest away objects, this implies a typical distance underestimate of four percent at most. As discussed in section 5, SDSS J0447+1124 is an exception, having a maximum  $r$ -band extinction of 1.3 mag, and so could be up to 80 percent further away than our calculation suggests.

Secondly, we do not account for Lutz-Kelker bias, which places greater statistical weight on larger distances as the prior distribution on distance  $d$  is proportional to  $d^2$  for nearby stars uniformly distributed in space. As our relative distance errors are all near 13 percent, Lutz-Kelker bias would lead to a typical underestimate of 3.5 percent. Finally there is some evidence that magnetic white dwarfs may be drawn from a different mass-distribution with higher mean than their non-magnetic counterparts (Liebert 1988; Liebert et al. 2003). If true, then magnetic systems may be closer than our estimates suggest. However considering the above, for vast majority of objects the distance uncertainties remain dominated by the poorly constrained white

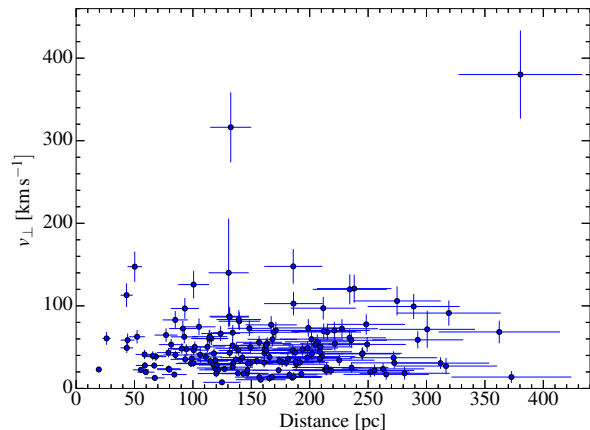


**Figure 14.** Tangential space-velocities against the estimated distance for the DZs in our sample for which a proper-motion measurement is available.

dwarf masses/radii resulting in relative distance errors of 12–14 percent.

Combining the distance estimates with proper-motions (and their uncertainties), we also calculated the tangential velocities for our DZ sample. As described in Section 2.1.1, not all objects have a proper-motion measured by SDSS. For a few bright objects with no proper-motion, we instead obtained values from PPMXL. These systems are SDSS J0044+0418, SDSS J0117+0021, SDSS J0842+1406, SDSS J1144+1218, SDSS J1329+1301, and SDSS J2225+2338.

Finally, the grid of cooling models also includes cooling ages for given masses and  $T_{\text{eff}}$ . Like radii, we used a Monte-Carlo method to calculate cooling ages and uncertainties. While we do not discuss ages in this section beyond their calculation they are covered in Paper II with relevance to remnant planetary systems.

In appendix Table A4 we list our calculated distances, (and where available) proper-motions,  $\mu$ , estimated tangential velocities,  $v_{\perp}$ , and cooling ages. Note that the calculated posterior-distributions for ages were often asymmetric, and so the quoted values and uncertainties correspond to the median and  $\pm 1\sigma$  percentiles. In Figure 14, we show  $v_{\perp}$  against distance (objects with no measured proper-motion are not displayed). Note that while both horizontal and vertical error-bars are shown,  $v_{\perp}$  is strongly correlated with the distance, and so the corresponding error-ellipses are narrow.

The two systems SDSS J0117+0021 and SDSS J1443+5833 stand out in Figure 14 as high  $v_{\perp}$  outliers, with tangential velocities  $316 \pm 42 \text{ km s}^{-1}$  and  $380 \pm 53 \text{ km s}^{-1}$  respectively. Such fast moving objects are certainly halo stars. While main-sequence halo stars are typically found with low metallicities, these two objects demonstrate that halo stars *are* hosts to planetary systems which survive stellar evolution to the white dwarf stage. This is further supported by Koester & Kepler (2015) who show two DBZ stars with heights exceeding 400 pc above the Galactic plane.

All other systems in Figure 14 have  $v_{\perp}$  below  $150 \text{ km s}^{-1}$  indicating these are Galactic disc members, and their distribution in  $v_{\perp}$  appears constant with distance, as would be ex-

<sup>5</sup> The DB cooling models we have used (accessed Sep 2016) can be found at <http://www.astro.umontreal.ca/~bergeron/CoolingModels/>.

pected out to only a few 100 pc. The mean  $v_{\perp}$  (still excluding the two probable halo white dwarfs) is  $30.14 \pm 0.44 \text{ km s}^{-1}$ . Although it is impossible to know the total-space velocities,  $v_{\text{tot}}$ , for any of these white dwarfs without measuring their radial-velocities, statistically the mean of  $v_{\text{tot}}$  is a factor  $\Gamma(3/2)^{-2} = 4/\pi$  larger than  $v_{\perp}$  as these are chi-distributed with 3 and 2 degrees of freedom respectively. Including the effect of low number statistics, we estimate the average  $v_{\text{tot}}$  for our sample to be  $38.4 \pm 1.1 \text{ km s}^{-1}$ .

One final object worth noting in this section is SDSS J1535+1247, otherwise known as WD1532+129 or G137-24. It was first recognised as a white dwarf by Eggen (1968) photometrically/astrometrically, but was not spectroscopically classed as a DZ until more recently (Kawka et al. 2004). This is by far the brightest DZ in our sample ( $r = 15.5$ ), and evidently from our calculations, the closest to the Sun. While previously known to be a member of the 25 pc local sample (Kawka et al. 2004; Kawka & Vennes 2006; Sion et al. 2014), our estimate of  $19.4 \pm 2.5 \text{ pc}$  suggests a moderate probability of it also being a member of the 20 pc local sample. The steady revision to closer distances (24 pc in Kawka et al. 2004; Kawka & Vennes 2006 and 22 pc in Sion et al. 2014) is however no great surprise as the spectroscopic  $T_{\text{eff}}$  have also decreased with improvements in both atomic physics and quality of the available spectra. We believe the “rapid cooling” of SDSS J1535+1247 within the recent literature is unlikely to continue, as our fit is strongly constrained by our WHT spectrum at blue wavelengths inaccessible to BOSS (See figure 5). The remaining uncertainty in the distance to SDSS J1535+1247 comes almost entirely from the unknown mass/radius – all of which will be significantly constrained by *Gaia* DR2.

## 9 CONCLUSIONS

We have identified a large sample of 231 cool DZ white dwarfs showing strong photospheric absorption features in their spectra. Our improved model atmospheres incorporate updated line profiles as well new transitions required to correctly model the observed spectra particularly below 3600 Å. Comparing our sample with other work on metal-rich helium atmosphere white dwarfs, we find an unexpected trend in the highest Ca abundances as a function of  $T_{\text{eff}}$  motivating further investigation into the structure of white dwarf convection zones. We also find several cool objects exhibiting large amounts of trace hydrogen, although we are unable to make any claims on the source of the hydrogen from the small number of systems. Finally we calculate distances and space-motions for the objects in our sample, with two objects clearly originating from the Galactic halo, providing compelling evidence for remnant planetary systems around halo objects.

## ACKNOWLEDGEMENTS

Funding for the Sloan Digital Sky Survey IV has been provided by the Alfred P. Sloan Foundation, the U.S. Department of Energy Office of Science, and the Participating Institutions. SDSS-IV acknowledges support and resources from

the Center for High-Performance Computing at the University of Utah. The SDSS web site is [www.sdss.org](http://www.sdss.org).

This work makes use of observations made with the William Herschel Telescope operated on the island of La Palma by the Isaac Newton Group in the Spanish Observatorio del Roque de los Muchachos of the Instituto de Astrofísica de Canarias.

## REFERENCES

- Aannestad P. A., Sion E. M., 1985, *AJ*, **90**, 1832  
Allard N. F., Alekseev V. A., 2014, *Adv. Space Res.*, **54**, 1248  
Allard N., Kielkopf J., 1982, *Rev. Mod. Phys.*, **54**, 1103  
Allard N. F., Royer A., Kielkopf J. F., Feautrier N., 1999, *Phys. Rev. A*, **60**, 1021  
Allard N. F., Leininger T., Gad  a F. X., Brousseau-Couture V., Dufour P., 2016a, *A&A*, **588**, A142  
Allard N. F., Guillon G., Alekseev V. A., Kielkopf J. F., 2016b, *A&A*, **593**, A13  
Alml  f J., Taylor P. R., 1987, *J. Chem. Phys.*, **86**, 4070  
Alonso R., Rappaport S., Deeg H. J., Palle E., 2016, *A&A*, **589**, L6  
Aquilante F., et al., 2010, *J. Comp. Chem.*, **31**, 224  
Becklin E. E., Farihi J., Jura M., Song I., Weinberger A. J., Zuckerman B., 2005, *ApJ Lett.*, **632**, L119  
Bergeron P., Ruiz M. T., Leggett S. K., 1997, *ApJS*, **108**, 339  
Bergeron P., Leggett S. K., Ruiz M., 2001, *ApJS*, **133**, 413  
Bergeron P., et al., 2011, *ApJ*, **737**, 28  
Bergeron P., Rolland B., Limoges M.-M., Giammichele N., S  guin-Charbonneau L., Green E. M., 2015, in Dufour P., Bergeron P., Fontaine G., eds, *Astronomical Society of the Pacific Conference Series Vol. 493, 19th European Workshop on White Dwarfs*. p. 33  
Czuchaj E., Rebentrost F., Stoll H., Preuss H., 1996, *Contemp. Phys.*, **207**, 51  
Dawson K. S., et al., 2013, *AJ*, **145**, 10  
Debes J. H., Sigurdsson S., 2002, *ApJ*, **572**, 556  
Demetropoulos I. N., Lawley K. P., 1982, *J. Phys. B*, **15**, 1855  
Dufour P., Bergeron P., Schmidt G. D., Liebert J., Harris H. C., Knapp G. R., Anderson S. F., Schneider D. P., 2006, *ApJ*, **651**, 1112  
Dufour P., et al., 2007, *ApJ*, **663**, 1291  
Dufour P., Kilic M., Fontaine G., Bergeron P., Melis C., Bochanski J., 2012, *ApJ*, **749**, 6  
Eggen O. J., 1968, *ApJS*, **16**, 97  
Eisenstein D. J., et al., 2006, *ApJS*, **167**, 40  
Farihi J., 2016, *New Astron. Rev.*, **71**, 9  
Farihi J., Barstow M. A., Redfield S., Dufour P., Hambly N. C., 2010, *MNRAS*, **404**, 2123  
Farihi J., G  nsicke B. T., Steele P. R., Girven J., Burleigh M. R., Breedt E., Koester D., 2012, *MNRAS*, **421**, 1635  
Farihi J., G  nsicke B. T., Koester D., 2013, *Science*, **342**, 218  
Finley J., Malmqvist P.-  ., Roos B. O., Serrano-Andr  s L., 1998, *Chem. Phys. Lett.*, **288**, 299  
G  nsicke B. T., Marsh T. R., Southworth J., Rebassa-Mansergas A., 2006, *Science*, **314**, 1908  
G  nsicke B. T., Koester D., Farihi J., Girven J., Parsons S. G., Breedt E., 2012, *MNRAS*, **424**, 333  
G  nsicke B. T., et al., 2016, *ApJ*, **818**, L7  
Gates E., et al., 2004, *ApJ*, **612**, L129  
Genest-Beaulieu C., Bergeron P., 2014, *ApJ*, **796**, 128  
Giusti-Suzor A., Roueff E., 1975, *J. Phys. B*, **8**, 2708  
Graham J. R., Matthews K., Neugebauer G., Soifer B. T., 1990, *ApJ*, **357**, 216  
Guo J., Tziamtzis A., Wang Z., Liu J., Zhao J., Wang S., 2015, *ApJ*, **810**, L17

- Harris M. J., Teegarden B. J., Cline T. L., Gehrels N., Palmer D. M., Ramaty R., Seifert H., 2000, *ApJ*, **542**, 1057
- Harris H. C., et al., 2001, *ApJ Lett.*, **549**, L109
- Harris H. C., et al., 2008, *ApJ*, **679**, 697
- Hintzen P., Tapia S., 1975, *ApJ*, **199**, L31
- Holberg J. B., Bergeron P., 2006, *AJ*, **132**, 1221
- Hollands M. A., Gänsicke B. T., Koester D., 2015, *MNRAS*, **450**, 681
- Jura M., 2003, *ApJ Lett.*, **584**, L91
- Kawka A., Vennes S., 2006, *ApJ*, **643**, 402
- Kawka A., Vennes S., Thorstensen J. R., 2004, *AJ*, **127**, 1702
- Kepler S. O., et al., 2015, *MNRAS*, **446**, 4078
- Kepler S. O., et al., 2016, *MNRAS*, **455**, 3413
- Kilic M., von Hippel T., Leggett S. K., Winget D. E., 2005, *ApJ Lett.*, **632**, L115
- Kleinman S. J., et al., 2004, *ApJ*, **607**, 426
- Kleinman S. J., et al., 2013, *ApJS*, **204**, 5
- Koester D., 2009, *A&A*, **498**, 517
- Koester D., 2010, *Memorie della Societa Astronomica Italiana*, **81**, 921
- Koester D., Kepler S. O., 2015, *A&A*, **583**, A86
- Koester D., Wilken D., 2006, *A&A*, **453**, 1051
- Koester D., Girven J., Gänsicke B. T., Dufour P., 2011, *A&A*, **530**, A114
- Koester D., Gänsicke B. T., Farihi J., 2014, *A&A*, **566**, A34
- Kowalski P. M., Saumon D., 2006, *ApJ*, **651**, L137
- Kramida A., Ralchenko Y., Reader J., NIST ASD Team 2016, NIST Atomic Spectra Database (version 5.4), [Online], <http://physics.nist.gov/asd>
- Kupka F., Piskunov N., Ryabchikova T. A., Stempels H. C., Weiss W. W., 1999, *A&AS*, **138**, 119
- Leininger T., Gadéa F. X., Allard N. F., 2015, in Martins F., Boissier S., Buat V., Cambrésy L., Petit P., eds, *SF2A-2015: Proceedings of the Annual meeting of the French Society of Astronomy and Astrophysics*. pp 397–399
- Li N., Thakar A. R., 2008, *Computing in Science and Engineering*, **10**, 18
- Liebert J., 1988, *PASP*, **100**, 1302
- Liebert J., Bergeron P., Holberg J. B., 2003, *AJ*, **125**, 348
- Malmqvist P. Å., Roos B. O., Schimmelpennig B., 2002, *Chem. Phys. Lett.*, **357**, 230
- Margala D., Kirkby D., Dawson K., Bailey S., Blanton M., Schneider D. P., 2015, preprint, ([arXiv:1506.04790](https://arxiv.org/abs/1506.04790))
- McDonough W., 2000, in Teisseyre R., Majewski E., eds, *Earthquake Thermodynamics and Phase Transformation in the Earth's Interior*. Elsevier Science Academic Press, pp 5–24
- Melis C., et al., 2012, *ApJ Lett.*, **751**, L4
- Monteiro T. S., Cooper I. L., Dickinson A. S., Lewis E. L., 1986, *J. Phys. B*, **19**, 4087
- Piskunov N. E., Kupka F., Ryabchikova T. A., Weiss W. W., Jeffery C. S., 1995, *A&AS*, **112**, 525
- Raddi R., Gänsicke B. T., Koester D., Farihi J., Hermes J. J., Scaringi S., Breedt E., Girven J., 2015, *MNRAS*, **450**, 2083
- Rappaport S., Gary B. L., Kaye T., Vanderburg A., Croll B., Benni P., Foote J., 2016, *MNRAS*, **458**, 3904
- Rebassa-Mansergas A., Gänsicke B. T., Rodríguez-Gil P., Schreiber M. R., Koester D., 2007, *MNRAS*, **382**, 1377
- Reid I. N., Liebert J., Schmidt G. D., 2001, *ApJ Lett.*, **550**, L61
- Roos B. O., Lindh R., Malmqvist P.-A., Veryazov V., Widmark P. O., 2004, *J. Chem. Phys.*, **108**, 2851
- Ross N. P., et al., 2012, *ApJS*, **199**, 3
- Ryabchikova T. A., Piskunov N. E., Kupka F., Weiss W. W., 1997, *Baltic Astronomy*, **6**, 244
- Schlegel D. J., Finkbeiner D. P., Davis M., 1998, *ApJ*, **500**, 525
- Schmidt G. D., et al., 2003, *ApJ*, **595**, 1101
- Shipman H. L., Greenstein J. L., Boksenberg A., 1977, *AJ*, **82**, 480
- Sion E. M., Greenstein J. L., Landstreet J. D., Liebert J., Shipman H. L., Wegner G. A., 1983, *ApJ*, **269**, 253
- Sion E. M., Holberg J. B., Oswalt T. D., McCook G. P., Wasatonic R., Myszkowski J., 2014, *AJ*, **147**, 129
- Vanderburg A., et al., 2015, *Nat*, **526**, 546
- Vauclair G., Vauclair S., Greenstein J. L., 1979, *A&A*, **80**, 79
- Veras D., 2016, *Royal Society Open Science*, **3**, 150571
- Veras D., Gänsicke B. T., 2015, *MNRAS*, **447**, 1049
- Veras D., Leinhardt Z. M., Bonsor A., Gänsicke B. T., 2014a, *MNRAS*, **445**, 2244
- Veras D., Shannon A., Gänsicke B. T., 2014b, *MNRAS*, **445**, 4175
- Walkup R., Stewart B., Pritchard D. E., 1984, *Phys. Rev. A*, **29**, 169
- Weidemann V., 1960, *ApJ*, **131**, 638
- Wilson D. J., Gänsicke B. T., Koester D., Raddi R., Breedt E., Southworth J., Parsons S. G., 2014, *MNRAS*, **445**, 1878
- Xu S., Jura M., Dufour P., Zuckerman B., 2016, *ApJ Lett.*, **816**, L22
- Zuckerman B., 2015, in Dufour P., Bergeron P., Fontaine G., eds, *Astronomical Society of the Pacific Conference Series Vol. 493, 19th European Workshop on White Dwarfs*. p. 291 ([arXiv:1410.2575](https://arxiv.org/abs/1410.2575))
- Zuckerman B., Becklin E. E., 1987, *Nat*, **330**, 138
- Zuckerman B., Reid I. N., 1998, *ApJ*, **505**, L143
- Zuckerman B., Koester D., Reid I. N., Hünsch M., 2003, *ApJ*, **596**, 477
- Zuckerman B., Koester D., Melis C., Hansen B. M., Jura M., 2007, *ApJ*, **671**, 872
- van Maanen A., 1917, *PASP*, **29**, 258

## APPENDIX A: ADDITIONAL TABLES

Table A1: SDSS PSF photometry for all white dwarfs in our sample. Plate-MJD-fib indicates the SDSS spectrum we used for fitting.  $N_{\text{SDSS}}$  is the number of SDSS spectra available per object.

SDSS J	Plate-MJD-Fib	$N_{\text{SDSS}}$	$u$	$g$	$r$	$i$	$z$
000215.64+320914.1	7144-56564-126	2	$21.830 \pm 0.120$	$20.530 \pm 0.024$	$20.346 \pm 0.022$	$20.381 \pm 0.034$	$20.329 \pm 0.114$
000418.68+081929.9	4534-55863-333	1	$24.871 \pm 0.704$	$22.133 \pm 0.067$	$21.648 \pm 0.058$	$21.757 \pm 0.092$	$21.701 \pm 0.299$
000614.53+052039.0	4415-55831-160	1	$22.142 \pm 0.261$	$20.507 \pm 0.029$	$20.240 \pm 0.035$	$20.154 \pm 0.046$	$20.282 \pm 0.200$
001052.56-043014.3	7035-56568-898	1	$21.553 \pm 0.137$	$20.317 \pm 0.028$	$20.112 \pm 0.025$	$20.218 \pm 0.040$	$20.285 \pm 0.123$
001309.43+110949.0	5648-55923-842	1	$23.397 \pm 0.488$	$21.612 \pm 0.049$	$21.263 \pm 0.054$	$21.373 \pm 0.095$	$21.537 \pm 0.339$
001949.25+220926.5	6175-56265-833	1	$21.948 \pm 0.217$	$20.394 \pm 0.043$	$19.958 \pm 0.035$	$20.043 \pm 0.041$	$20.140 \pm 0.202$
003708.41-052532.7	7039-56572-140	2	$22.933 \pm 0.388$	$20.087 \pm 0.027$	$19.634 \pm 0.024$	$19.682 \pm 0.024$	$19.784 \pm 0.070$
004451.68+041819.2	4305-55509-609	1	$19.902 \pm 0.042$	$18.773 \pm 0.020$	$18.486 \pm 0.019$	$18.459 \pm 0.022$	$18.564 \pm 0.035$
004634.22+271737.6	6253-56574-458	1	$21.139 \pm 0.109$	$20.372 \pm 0.026$	$20.258 \pm 0.032$	$20.412 \pm 0.051$	$20.780 \pm 0.290$
004757.06+162836.5	6204-56220-386	1	$25.126 \pm 0.786$	$20.865 \pm 0.036$	$20.393 \pm 0.033$	$20.518 \pm 0.041$	$20.380 \pm 0.141$
005247.16+184649.5	5702-56221-615	1	$25.922 \pm 0.716$	$21.571 \pm 0.073$	$21.118 \pm 0.057$	$21.062 \pm 0.069$	$20.745 \pm 0.172$
005304.14+311555.8	6872-56540-171	1	$22.704 \pm 0.512$	$21.298 \pm 0.048$	$21.056 \pm 0.052$	$21.105 \pm 0.080$	$21.141 \pm 0.298$
005649.27+245335.4	6278-56266-122	1	$24.797 \pm 0.853$	$21.536 \pm 0.049$	$21.009 \pm 0.041$	$20.948 \pm 0.059$	$21.431 \pm 0.341$
010728.47+265019.9	6255-56240-896	1	$23.268 \pm 0.643$	$19.359 \pm 0.022$	$18.828 \pm 0.015$	$18.671 \pm 0.018$	$18.783 \pm 0.050$
010825.79-053755.6	7045-56577-456	2	$22.046 \pm 0.215$	$20.392 \pm 0.031$	$20.124 \pm 0.024$	$20.021 \pm 0.048$	$20.363 \pm 0.109$
011421.17+350547.1	6598-56574-832	1	$23.250 \pm 0.578$	$20.958 \pm 0.031$	$20.596 \pm 0.033$	$20.659 \pm 0.051$	$20.387 \pm 0.138$
011646.10+205001.9	5134-55868-352	1	$19.883 \pm 0.033$	$18.209 \pm 0.018$	$17.987 \pm 0.010$	$18.081 \pm 0.014$	$18.187 \pm 0.027$
011759.83+002138.3	4227-55481-937	2	$20.192 \pm 0.047$	$19.316 \pm 0.028$	$19.116 \pm 0.017$	$19.169 \pm 0.022$	$19.368 \pm 0.059$
012620.47+253433.6	5694-56213-606	1	$22.651 \pm 0.531$	$20.639 \pm 0.041$	$20.205 \pm 0.036$	$20.101 \pm 0.040$	$20.308 \pm 0.155$
013504.11+130240.4	4661-55614-318	2	$20.842 \pm 0.073$	$19.311 \pm 0.022$	$18.997 \pm 0.019$	$18.932 \pm 0.019$	$18.985 \pm 0.054$
014300.52+011356.8	4231-55444-824	4	$20.313 \pm 0.053$	$19.410 \pm 0.033$	$19.215 \pm 0.029$	$19.235 \pm 0.021$	$19.403 \pm 0.056$
014415.12+192021.4	5121-55856-186	1	$24.291 \pm 1.603$	$20.690 \pm 0.049$	$20.398 \pm 0.043$	$20.339 \pm 0.063$	$20.364 \pm 0.184$
014441.64+030536.2	4272-55509-246	1	$22.806 \pm 0.304$	$21.302 \pm 0.040$	$21.166 \pm 0.049$	$21.218 \pm 0.074$	$21.379 \pm 0.298$
014834.00-011235.9	4232-55447-294	2	$21.808 \pm 0.118$	$20.752 \pm 0.029$	$20.610 \pm 0.033$	$20.644 \pm 0.043$	$20.683 \pm 0.133$
015008.55+135433.9	1899-53262-118	1	$21.033 \pm 0.079$	$20.152 \pm 0.026$	$19.919 \pm 0.026$	$19.887 \pm 0.030$	$19.849 \pm 0.098$
015748.14+003315.0	0700-52199-627	1	$21.299 \pm 0.074$	$19.591 \pm 0.023$	$19.189 \pm 0.017$	$19.213 \pm 0.020$	$19.359 \pm 0.050$
015849.02-094225.3	7184-56629-144	1	$21.663 \pm 0.169$	$20.408 \pm 0.033$	$20.199 \pm 0.026$	$20.200 \pm 0.038$	$20.472 \pm 0.166$
020018.74+164631.0	5119-55836-838	1	$22.587 \pm 0.259$	$20.891 \pm 0.033$	$20.391 \pm 0.030$	$20.492 \pm 0.047$	$20.489 \pm 0.151$
020128.66+201521.8	5110-55913-721	1	$21.714 \pm 0.236$	$20.392 \pm 0.034$	$20.040 \pm 0.035$	$20.183 \pm 0.069$	$20.325 \pm 0.178$
020809.93-054258.3	4398-55946-982	1	$23.635 \pm 0.773$	$21.179 \pm 0.056$	$20.786 \pm 0.043$	$20.739 \pm 0.051$	$20.836 \pm 0.191$
023407.46-051028.1	4399-55811-626	1	$22.605 \pm 0.301$	$21.103 \pm 0.044$	$20.885 \pm 0.042$	$20.979 \pm 0.066$	$21.010 \pm 0.257$
025206.06-040130.3	7054-56575-682	1	$21.424 \pm 0.117$	$20.280 \pm 0.027$	$20.095 \pm 0.024$	$20.212 \pm 0.035$	$20.423 \pm 0.134$
025253.19+005439.4	0708-52175-411	1	$20.636 \pm 0.055$	$19.863 \pm 0.030$	$19.784 \pm 0.017$	$19.834 \pm 0.025$	$19.950 \pm 0.076$
044751.20+112403.7	2673-54096-587	1	$21.231 \pm 0.088$	$20.364 \pm 0.022$	$20.065 \pm 0.023$	$19.981 \pm 0.028$	$20.124 \pm 0.106$
051212.78-050503.4		0	$20.722 \pm 0.155$	$17.913 \pm 0.017$	$17.437 \pm 0.017$	$17.424 \pm 0.017$	$17.492 \pm 0.021$
072144.23+392843.3	3655-55240-286	1	$22.767 \pm 0.431$	$20.555 \pm 0.029$	$20.282 \pm 0.039$	$20.383 \pm 0.053$	$20.341 \pm 0.160$
073549.19+205720.9	4480-55591-432	1	$23.084 \pm 0.344$	$20.527 \pm 0.025$	$19.979 \pm 0.020$	$19.922 \pm 0.024$	$20.089 \pm 0.092$
073635.22+411828.1	3664-55245-628	1	$25.470 \pm 0.604$	$20.317 \pm 0.025$	$19.418 \pm 0.026$	$19.272 \pm 0.050$	$19.313 \pm 0.058$
073953.46+311204.2	4448-55538-588	1	$23.832 \pm 0.605$	$21.377 \pm 0.043$	$20.778 \pm 0.037$	$20.652 \pm 0.043$	$20.441 \pm 0.169$
074153.45+314620.4	4443-55539-251	1	$22.581 \pm 0.227$	$20.501 \pm 0.028$	$20.125 \pm 0.022$	$20.120 \pm 0.026$	$20.189 \pm 0.076$
074414.66+464912.5	3665-55247-106	2	$23.021 \pm 0.344$	$19.473 \pm 0.028$	$18.517 \pm 0.012$	$18.316 \pm 0.016$	$18.261 \pm 0.026$
074444.03+440845.6	3671-55483-294	1	$22.612 \pm 0.290$	$21.176 \pm 0.037$	$21.010 \pm 0.052$	$20.978 \pm 0.067$	$21.210 \pm 0.349$
074450.24+270132.6	4462-55600-836	1	$20.980 \pm 0.075$	$20.278 \pm 0.026$	$20.180 \pm 0.030$	$20.410 \pm 0.043$	$20.493 \pm 0.167$
074456.21+164041.8	4492-55565-292	1	$24.635 \pm 0.898$	$20.880 \pm 0.029$	$20.185 \pm 0.022$	$20.027 \pm 0.024$	$20.067 \pm 0.080$
075853.46+101347.4	4510-55559-490	1	$23.820 \pm 0.726$	$21.418 \pm 0.044$	$20.711 \pm 0.032$	$20.751 \pm 0.045$	$20.956 \pm 0.196$
080003.90+224210.1	4471-55617-740	1	$22.321 \pm 0.224$	$20.712 \pm 0.029$	$20.587 \pm 0.040$	$20.561 \pm 0.039$	$20.742 \pm 0.191$
080626.70+305555.7	3755-55504-120	1	$22.001 \pm 0.153$	$20.670 \pm 0.029$	$20.495 \pm 0.027$	$20.598 \pm 0.038$	$20.629 \pm 0.115$
080643.94+405837.7	3803-55513-734	1	$20.563 \pm 0.055$	$19.078 \pm 0.018$	$18.771 \pm 0.015$	$18.773 \pm 0.017$	$18.863 \pm 0.044$
080740.69+493059.7	3684-55246-924	1	$25.311 \pm 0.993$	$21.308 \pm 0.052$	$20.522 \pm 0.036$	$20.330 \pm 0.043$	$20.193 \pm 0.142$
081606.19+233030.1	4468-55894-462	1	$22.021 \pm 0.234$	$20.958 \pm 0.033$	$20.818 \pm 0.035$	$21.073 \pm 0.057$	$20.871 \pm 0.181$
081828.12+124717.2	4504-55571-200	1	$22.060 \pm 0.196$	$21.000 \pm 0.034$	$20.853 \pm 0.039$	$21.021 \pm 0.063$	$21.231 \pm 0.276$
082303.82+054656.1		0	$19.526 \pm 0.033$	$17.500 \pm 0.014$	$17.155 \pm 0.013$	$17.179 \pm 0.016$	$17.261 \pm 0.022$
083033.65-031911.0	2828-54438-401	1	$20.794 \pm 0.080$	$19.687 \pm 0.016$	$19.491 \pm 0.019$	$19.555 \pm 0.027$	$19.680 \pm 0.112$
083200.38+410937.9	3808-55513-148	1	$23.623 \pm 0.794$	$21.321 \pm 0.050$	$20.631 \pm 0.033$	$20.695 \pm 0.045$	$20.755 \pm 0.138$
083858.56+232252.9	3373-54940-462	2	$20.187 \pm 0.046$	$19.212 \pm 0.020$	$18.860 \pm 0.015$	$18.819 \pm 0.017$	$18.835 \pm 0.036$
084223.14+140615.9	2427-53815-040	2	$19.286 \pm 0.027$	$18.312 \pm 0.022$	$18.166 \pm 0.026$	$18.271 \pm 0.018$	$18.439 \pm 0.028$
084239.85+153628.8	5286-56225-336	1	$22.017 \pm 0.136$	$20.761 \pm 0.037$	$20.479 \pm 0.036$	$20.451 \pm 0.052$	$20.365 \pm 0.131$
084300.22+561452.8	5153-56577-159	1	$21.822 \pm 0.187$	$20.522 \pm 0.037$	$20.306 \pm 0.034$	$20.377 \pm 0.051$	$20.407 \pm 0.186$
085100.23+154301.6	5292-55926-402	2	$20.282 \pm 0.053$	$19.033 \pm 0.014$	$18.726 \pm 0.020$	$18.785 \pm 0.033$	$18.844 \pm 0.052$
085217.60+340211.3	4602-55644-366	2	$23.720 \pm 0.564$	$21.253 \pm 0.041$	$20.438 \pm 0.028$	$20.434 \pm 0.035$	$20.124 \pm 0.090$
090146.86+075206.8	4868-55895-702	1	$21.541 \pm 0.115$	$20.012 \pm 0.020$	$19.800 \pm 0.021$	$19.903 \pm 0.030$	$20.047 \pm 0.126$



SDSS J	Plate-MJD-Fib	$N_{\text{SDSS}}$	$u$	$g$	$r$	$i$	$z$
090222.98+362539.6	4645-55623-596	2	$22.577 \pm 0.321$	$20.752 \pm 0.032$	$20.462 \pm 0.038$	$20.363 \pm 0.056$	$20.495 \pm 0.222$
090244.75+100459.6	5296-55922-260	1	$21.335 \pm 0.086$	$20.705 \pm 0.026$	$20.620 \pm 0.032$	$20.653 \pm 0.048$	$20.649 \pm 0.153$
090652.19+114149.9	5296-55922-944	1	$22.859 \pm 0.265$	$20.958 \pm 0.032$	$20.795 \pm 0.035$	$20.823 \pm 0.043$	$20.991 \pm 0.160$
090803.35+513633.1	5729-56598-406	2	$20.845 \pm 0.059$	$19.485 \pm 0.021$	$19.255 \pm 0.023$	$19.270 \pm 0.020$	$19.402 \pm 0.061$
090814.52+411918.3	4603-55999-334	1	$22.285 \pm 0.180$	$21.154 \pm 0.032$	$20.919 \pm 0.036$	$20.990 \pm 0.048$	$21.139 \pm 0.205$
091322.38+262752.0	5779-56338-164	2	$22.789 \pm 0.250$	$20.281 \pm 0.038$	$19.786 \pm 0.021$	$19.722 \pm 0.026$	$19.618 \pm 0.056$
091356.05+412728.6	4641-55947-678	1	$23.903 \pm 0.532$	$21.074 \pm 0.031$	$20.628 \pm 0.029$	$20.742 \pm 0.040$	$20.749 \pm 0.132$
091621.36+254028.4	2087-53415-166	1	$21.256 \pm 0.094$	$18.355 \pm 0.014$	$17.473 \pm 0.024$	$17.386 \pm 0.018$	$17.526 \pm 0.021$
092450.03+430136.4	4639-55944-860	1	$23.633 \pm 0.353$	$21.111 \pm 0.033$	$20.888 \pm 0.032$	$20.817 \pm 0.047$	$20.698 \pm 0.143$
092523.09+313019.0	1938-53379-608	2	$21.030 \pm 0.086$	$18.957 \pm 0.021$	$18.606 \pm 0.015$	$18.634 \pm 0.016$	$18.750 \pm 0.041$
092713.34+493109.3	5731-56363-684	1	$22.527 \pm 0.199$	$21.095 \pm 0.035$	$20.744 \pm 0.029$	$20.883 \pm 0.044$	$20.841 \pm 0.152$
092932.49+424757.9	4639-55944-034	2	$21.622 \pm 0.081$	$20.183 \pm 0.031$	$19.914 \pm 0.021$	$19.962 \pm 0.031$	$20.190 \pm 0.100$
093320.01+633441.2	7447-56746-366	1	$23.397 \pm 0.350$	$21.111 \pm 0.035$	$20.817 \pm 0.047$	$20.905 \pm 0.065$	$20.995 \pm 0.280$
093719.14+522802.2	2404-53764-197	3	$20.732 \pm 0.068$	$19.438 \pm 0.023$	$19.168 \pm 0.019$	$19.240 \pm 0.025$	$19.449 \pm 0.078$
093916.03+413612.9	4571-55629-621	1	$23.029 \pm 0.336$	$20.568 \pm 0.026$	$20.183 \pm 0.026$	$20.210 \pm 0.033$	$20.311 \pm 0.120$
093944.58+501917.6	0901-52641-584	1	$22.920 \pm 0.288$	$19.940 \pm 0.018$	$19.484 \pm 0.016$	$19.511 \pm 0.018$	$19.657 \pm 0.062$
094648.94+202423.2	5783-56017-824	2	$21.587 \pm 0.097$	$20.825 \pm 0.029$	$20.629 \pm 0.030$	$20.853 \pm 0.043$	$20.627 \pm 0.140$
094813.73+300851.2	5801-56328-728	1	$21.615 \pm 0.147$	$20.274 \pm 0.031$	$20.034 \pm 0.023$	$20.103 \pm 0.032$	$20.131 \pm 0.094$
095645.14+591240.6	0453-51915-621	1	$18.936 \pm 0.027$	$18.387 \pm 0.020$	$18.409 \pm 0.013$	$18.559 \pm 0.019$	$18.753 \pm 0.037$
100346.66-003123.1	3783-55246-902	1	$22.909 \pm 0.329$	$20.615 \pm 0.030$	$20.059 \pm 0.025$	$19.997 \pm 0.029$	$20.203 \pm 0.111$
100537.43+224403.1	6459-56273-144	1	$23.046 \pm 0.325$	$21.356 \pm 0.045$	$21.117 \pm 0.042$	$21.275 \pm 1.079$	$21.197 \pm 0.215$
100609.15+175221.3	5332-55981-544	1	$22.401 \pm 0.189$	$20.663 \pm 0.041$	$20.179 \pm 0.031$	$20.156 \pm 0.035$	$20.118 \pm 0.106$
101451.15+282701.6	6462-56326-444	1	$23.453 \pm 0.517$	$21.252 \pm 0.042$	$20.701 \pm 0.051$	$20.824 \pm 0.059$	$21.151 \pm 0.282$
101711.53+344710.5	4568-55600-124	2	$21.642 \pm 0.123$	$20.452 \pm 0.027$	$20.247 \pm 0.032$	$20.233 \pm 0.038$	$20.135 \pm 0.115$
101750.24+241911.6	6465-56279-332	1	$21.217 \pm 0.082$	$19.889 \pm 0.026$	$19.768 \pm 0.024$	$19.812 \pm 0.026$	$19.839 \pm 0.086$
101924.73+353527.6	4564-55570-466	2	$22.920 \pm 0.408$	$21.210 \pm 0.040$	$20.889 \pm 0.044$	$21.017 \pm 0.059$	$21.076 \pm 0.215$
101959.51+204553.4	5872-56027-268	1	$23.411 \pm 0.430$	$21.049 \pm 0.037$	$20.583 \pm 0.031$	$20.547 \pm 0.043$	$20.356 \pm 0.102$
102414.83+453109.9	6659-56607-412	1	$21.735 \pm 0.156$	$20.322 \pm 0.034$	$20.038 \pm 0.032$	$20.009 \pm 0.032$	$20.190 \pm 0.108$
102438.05+101410.5	1598-53033-081	1	$23.057 \pm 0.385$	$20.591 \pm 0.029$	$20.031 \pm 0.026$	$20.129 \pm 0.053$	$20.186 \pm 0.129$
103205.15+133833.4	5343-55999-834	1	$24.857 \pm 0.782$	$21.195 \pm 0.038$	$20.784 \pm 0.039$	$20.617 \pm 0.052$	$21.316 \pm 0.349$
103352.89+180935.3	2593-54175-225	1	$21.466 \pm 0.109$	$19.810 \pm 0.018$	$19.447 \pm 0.022$	$19.462 \pm 0.029$	$19.718 \pm 0.104$
103809.19-003622.4	0274-51913-265	1	$17.714 \pm 0.013$	$17.006 \pm 0.020$	$16.942 \pm 0.014$	$17.084 \pm 0.013$	$17.313 \pm 0.016$
103839.00+043223.8	4773-55648-618	1	$22.431 \pm 0.241$	$20.665 \pm 0.031$	$20.303 \pm 0.031$	$20.305 \pm 0.033$	$20.439 \pm 0.140$
104046.48+240759.5	3250-54883-505	2	$21.521 \pm 0.100$	$19.329 \pm 0.018$	$18.829 \pm 0.015$	$18.834 \pm 0.017$	$18.995 \pm 0.042$
104130.65+343240.7	4635-55615-408	2	$21.356 \pm 0.108$	$20.625 \pm 0.036$	$20.590 \pm 0.037$	$20.643 \pm 0.054$	$20.632 \pm 0.206$
104319.84+351641.6	2025-53431-328	2	$20.651 \pm 0.069$	$18.963 \pm 0.017$	$18.648 \pm 0.022$	$18.612 \pm 0.017$	$18.672 \pm 0.035$
104658.12+132911.3	5350-56009-118	2	$23.915 \pm 0.630$	$20.698 \pm 0.026$	$20.069 \pm 0.026$	$20.005 \pm 0.029$	$19.890 \pm 0.082$
105533.73+372542.7	4630-55623-900	1	$22.756 \pm 0.280$	$20.332 \pm 0.031$	$19.751 \pm 0.021$	$19.825 \pm 0.026$	$19.965 \pm 0.083$
105826.60+314358.3	6445-56366-988	2	$19.807 \pm 0.039$	$19.093 \pm 0.023$	$18.949 \pm 0.022$	$19.012 \pm 0.020$	$19.183 \pm 0.058$
110216.09+282730.7	6435-56341-510	1	$23.454 \pm 0.510$	$21.286 \pm 0.047$	$20.868 \pm 0.044$	$20.955 \pm 0.073$	$20.873 \pm 0.210$
110234.21+021459.2	3243-54910-298	2	$21.220 \pm 0.077$	$19.525 \pm 0.024$	$19.196 \pm 0.020$	$19.165 \pm 0.023$	$19.299 \pm 0.063$
110304.15+414434.9	4620-55652-506	2	$21.677 \pm 0.159$	$19.747 \pm 0.022$	$19.397 \pm 0.019$	$19.395 \pm 0.022$	$19.421 \pm 0.057$
110513.62+500652.6	6700-56384-146	1	$21.127 \pm 0.100$	$20.252 \pm 0.028$	$20.190 \pm 0.024$	$20.312 \pm 0.049$	$20.159 \pm 0.140$
110556.17+022849.0	4741-55704-652	1	$22.056 \pm 0.212$	$20.552 \pm 0.034$	$20.174 \pm 0.029$	$20.127 \pm 0.038$	$19.889 \pm 0.139$
110644.27+673708.6	7111-56741-676	1	$22.310 \pm 0.258$	$20.113 \pm 0.026$	$19.673 \pm 0.023$	$19.731 \pm 0.030$	$19.819 \pm 0.098$
111215.05+070052.3	1004-52723-111	1	$20.179 \pm 0.046$	$19.272 \pm 0.018$	$19.243 \pm 0.023$	$19.346 \pm 0.021$	$19.414 \pm 0.060$
111330.26+275131.4	6435-56341-036	1	$22.262 \pm 0.167$	$20.751 \pm 0.030$	$20.415 \pm 0.031$	$20.501 \pm 0.048$	$20.350 \pm 0.144$
113209.59+332353.0	4619-55599-069	2	$24.582 \pm 0.909$	$21.115 \pm 0.044$	$20.756 \pm 0.037$	$20.847 \pm 0.057$	$21.036 \pm 0.227$
113410.85+154245.9	5373-56010-938	1	$22.526 \pm 0.220$	$21.132 \pm 0.034$	$20.978 \pm 0.043$	$21.031 \pm 0.074$	$20.715 \pm 0.212$
114333.46+661532.0	7114-56748-973	1	$22.386 \pm 0.229$	$20.560 \pm 0.027$	$20.013 \pm 0.026$	$19.955 \pm 0.035$	$20.128 \pm 0.121$
114408.04+372007.8	4653-55622-700	1	$21.081 \pm 0.076$	$20.292 \pm 0.025$	$20.194 \pm 0.031$	$20.290 \pm 0.035$	$20.262 \pm 0.133$
114441.92+121829.2	1608-53138-515	1	$20.715 \pm 0.079$	$18.422 \pm 0.017$	$17.849 \pm 0.020$	$17.758 \pm 0.019$	$17.762 \pm 0.024$
114709.09+542940.8	6697-56419-035	1	$25.843 \pm 0.540$	$21.547 \pm 0.053$	$21.030 \pm 0.049$	$20.923 \pm 0.058$	$20.953 \pm 0.257$
114944.94+051947.7	4848-55955-088	1	$20.503 \pm 0.049$	$19.602 \pm 0.024$	$19.480 \pm 0.021$	$19.636 \pm 0.020$	$19.736 \pm 0.073$
115015.73+492843.7	6684-56412-006	1	$20.495 \pm 0.067$	$19.956 \pm 0.027$	$19.887 \pm 0.028$	$19.928 \pm 0.034$	$19.971 \pm 0.105$
115029.52+453314.0	6642-56396-549	2	$24.280 \pm 0.927$	$21.658 \pm 0.057$	$21.066 \pm 0.060$	$21.018 \pm 0.068$	$20.982 \pm 0.199$
115207.15+510126.2	6683-56416-348	1	$24.857 \pm 0.807$	$21.438 \pm 0.046$	$20.845 \pm 0.040$	$20.698 \pm 0.049$	$20.672 \pm 0.165$
115224.51+160546.7	5383-56013-772	2	$21.733 \pm 0.116$	$20.175 \pm 0.025$	$19.952 \pm 0.020$	$20.016 \pm 0.032$	$20.076 \pm 0.090$
115748.34+613845.9	7106-56663-173	1	$22.472 \pm 0.391$	$21.420 \pm 0.059$	$21.266 \pm 0.064$	$21.244 \pm 0.124$	$21.192 \pm 0.415$
115809.38+184557.3	5881-56038-014	1	$21.550 \pm 0.115$	$20.041 \pm 0.025$	$19.883 \pm 0.025$	$19.951 \pm 0.029$	$20.109 \pm 0.093$
115809.88+594210.3	7098-56661-152	1	$22.138 \pm 0.189$	$20.593 \pm 0.024$	$20.304 \pm 0.024$	$20.295 \pm 0.033$	$20.094 \pm 0.110$
115818.76+045447.5	4747-55652-590	1	$23.094 \pm 0.320$	$20.957 \pm 0.035$	$20.255 \pm 0.027$	$20.129 \pm 0.028$	$20.274 \pm 0.091$
115822.31+471214.9	6644-56384-812	1	$21.309 \pm 0.088$	$20.666 \pm 0.033$	$20.624 \pm 0.037$	$20.716 \pm 0.055$	$20.809 \pm 0.219$
115844.35+544837.5	6839-56425-090	1	$22.781 \pm 0.352$	$21.020 \pm 0.042$	$20.774 \pm 0.042$	$20.797 \pm 0.058$	$20.772 \pm 0.237$
120548.97+353642.4	4610-55621-722	2	$24.075 \pm 1.094$	$20.393 \pm 0.034$	$20.095 \pm 0.035$	$20.110 \pm 0.047$	$20.398 \pm 0.141$
121106.42+232623.0	5974-56314-668	1	$22.285 \pm 0.294$	$20.796 \pm 0.034$	$20.524 \pm 0.042$	$20.561 \pm 0.056$	$20.489 \pm 0.136$
121456.39-023402.7	0333-52313-399	1	$20.872 \pm 0.062$	$18.324 \pm 0.017$	$17.749 \pm 0.013$	$17.561 \pm 0.012$	$17.509 \pm 0.021$

SDSS J	Plate-MJD-Fib	$N_{\text{SDSS}}$	$u$	$g$	$r$	$i$	$z$
121731.31+115715.9	5394-56001-974	2	$22.032 \pm 0.245$	$20.256 \pm 0.036$	$20.066 \pm 0.037$	$20.106 \pm 0.037$	$20.274 \pm 0.120$
121837.12+002303.7	2568-54153-352	3	$20.418 \pm 0.045$	$19.524 \pm 0.017$	$19.350 \pm 0.016$	$19.324 \pm 0.021$	$19.465 \pm 0.059$
122035.75+092948.1	5396-55947-158	1	$22.109 \pm 0.259$	$20.885 \pm 0.038$	$20.644 \pm 0.042$	$20.712 \pm 0.052$	$20.786 \pm 0.184$
122437.07+283853.0	5976-56356-818	2	$22.404 \pm 0.261$	$19.774 \pm 0.020$	$19.224 \pm 0.029$	$19.080 \pm 0.025$	$19.011 \pm 0.047$
122656.39+293643.9	2234-53823-273	2	$23.087 \pm 0.468$	$20.550 \pm 0.029$	$19.737 \pm 0.023$	$19.604 \pm 0.025$	$19.626 \pm 0.089$
122943.92+074311.8	5402-55927-698	2	$23.308 \pm 0.584$	$20.419 \pm 0.036$	$20.072 \pm 0.028$	$20.075 \pm 0.033$	$20.328 \pm 0.146$
123024.03+314339.7	6479-56364-318	1	$21.559 \pm 0.135$	$20.370 \pm 0.025$	$20.182 \pm 0.029$	$20.209 \pm 0.038$	$20.201 \pm 0.121$
123415.21+520808.1	0885-52379-269	1	$19.541 \pm 0.036$	$18.418 \pm 0.027$	$18.298 \pm 0.016$	$18.423 \pm 0.015$	$18.682 \pm 0.032$
123826.92+214937.7	5985-56089-738	2	$24.211 \pm 0.671$	$20.801 \pm 0.043$	$20.316 \pm 0.029$	$20.209 \pm 0.033$	$20.162 \pm 0.090$
124547.10+082231.4	5407-55926-966	1	$22.559 \pm 0.283$	$20.941 \pm 0.035$	$20.524 \pm 0.030$	$20.496 \pm 0.040$	$20.973 \pm 0.231$
124937.50+651407.6	6963-56724-634	1	$21.159 \pm 0.097$	$20.444 \pm 0.028$	$20.392 \pm 0.035$	$20.463 \pm 0.044$	$21.019 \pm 0.269$
125454.93+355145.7	3975-55321-364	1	$21.808 \pm 0.168$	$20.597 \pm 0.025$	$20.450 \pm 0.031$	$20.409 \pm 0.042$	$20.510 \pm 0.134$
125710.13+323848.5	6485-56342-980	1	$24.020 \pm 0.874$	$21.607 \pm 0.054$	$20.962 \pm 0.052$	$20.901 \pm 0.082$	$20.951 \pm 0.234$
125720.87-031025.1	3794-55241-204	1	$22.173 \pm 0.219$	$20.645 \pm 0.037$	$20.281 \pm 0.030$	$20.345 \pm 0.045$	$20.744 \pm 0.224$
125922.03+311215.2	1994-53845-010	1	$21.501 \pm 0.112$	$19.783 \pm 0.021$	$19.444 \pm 0.019$	$19.423 \pm 0.023$	$19.504 \pm 0.058$
125945.32+472953.6	6618-56401-742	1	$23.538 \pm 0.796$	$20.852 \pm 0.051$	$20.578 \pm 0.045$	$20.714 \pm 0.083$	$20.809 \pm 0.318$
130328.06+405545.5	4706-55705-506	1	$20.930 \pm 0.098$	$19.735 \pm 0.039$	$19.539 \pm 0.056$	$19.511 \pm 0.031$	$19.623 \pm 0.093$
130826.36+095724.0	5421-55980-840	1	$21.692 \pm 0.151$	$21.046 \pm 0.039$	$20.994 \pm 0.044$	$21.078 \pm 0.066$	$21.128 \pm 0.268$
130830.03+025844.5	4007-55327-584	1	$22.520 \pm 0.263$	$20.827 \pm 0.034$	$20.502 \pm 0.038$	$20.424 \pm 0.049$	$20.543 \pm 0.172$
131420.49+374806.5	3978-55330-030	1	$22.740 \pm 0.296$	$20.829 \pm 0.035$	$20.477 \pm 0.031$	$20.443 \pm 0.035$	$20.522 \pm 0.109$
131612.86+191806.5	5867-56034-712	2	$23.892 \pm 0.579$	$21.017 \pm 0.038$	$20.546 \pm 0.034$	$20.506 \pm 0.041$	$20.427 \pm 0.112$
131900.18+364149.8	3979-55597-929	1	$20.947 \pm 0.070$	$20.205 \pm 0.029$	$20.153 \pm 0.022$	$20.262 \pm 0.033$	$20.471 \pm 0.152$
132005.53+020419.0	4006-55328-686	1	$21.950 \pm 0.194$	$21.040 \pm 0.044$	$20.899 \pm 0.046$	$21.099 \pm 0.080$	$21.355 \pm 0.389$
132144.04-023751.4	4049-55591-276	1	$22.497 \pm 0.273$	$20.725 \pm 0.033$	$20.126 \pm 0.032$	$20.041 \pm 0.035$	$19.988 \pm 0.117$
132941.79+130131.9	5432-56008-689	1	$21.127 \pm 0.106$	$19.952 \pm 0.028$	$19.829 \pm 0.023$	$19.894 \pm 0.028$	$20.124 \pm 0.098$
133059.26+302953.2	2110-53467-148	1	$18.276 \pm 0.019$	$16.316 \pm 0.022$	$15.888 \pm 0.014$	$15.905 \pm 0.024$	$16.092 \pm 0.029$
133624.26+354751.2	2101-53858-254	1	$19.485 \pm 0.029$	$17.849 \pm 0.020$	$17.642 \pm 0.013$	$17.714 \pm 0.026$	$17.826 \pm 0.018$
133905.97+264322.9	6002-56104-590	1	$19.997 \pm 0.035$	$18.978 \pm 0.021$	$18.775 \pm 0.014$	$18.821 \pm 0.019$	$18.946 \pm 0.037$
134050.31+270219.0	6002-56104-622	1	$21.523 \pm 0.119$	$20.858 \pm 0.031$	$20.811 \pm 0.037$	$20.890 \pm 0.057$	$20.983 \pm 0.218$
134203.60+181332.8	5439-56045-828	1	$23.609 \pm 0.516$	$21.128 \pm 0.036$	$20.609 \pm 0.042$	$20.528 \pm 0.038$	$20.670 \pm 0.135$
134520.99+115357.6	1701-53142-440	1	$22.638 \pm 0.299$	$19.923 \pm 0.018$	$19.387 \pm 0.020$	$19.453 \pm 0.023$	$19.545 \pm 0.058$
134711.47+141528.0	5441-56017-258	1	$21.201 \pm 0.074$	$19.703 \pm 0.014$	$19.497 \pm 0.021$	$19.514 \pm 0.020$	$19.530 \pm 0.062$
135054.01+105808.0	5440-55983-996	1	$24.400 \pm 0.941$	$20.969 \pm 0.044$	$20.374 \pm 0.031$	$20.313 \pm 0.032$	$20.337 \pm 0.110$
135123.86+264546.5	6006-56105-212	2	$22.995 \pm 0.396$	$20.383 \pm 0.023$	$19.874 \pm 0.020$	$19.861 \pm 0.029$	$19.863 \pm 0.111$
135632.62+241606.0	2119-53792-216	1	$20.378 \pm 0.049$	$19.049 \pm 0.016$	$18.731 \pm 0.017$	$18.779 \pm 0.025$	$18.867 \pm 0.039$
135654.01+023641.5	4036-55330-762	1	$20.441 \pm 0.056$	$19.534 \pm 0.016$	$19.504 \pm 0.022$	$19.605 \pm 0.028$	$19.467 \pm 0.088$
140137.31+365909.9	1642-53115-198	1	$19.941 \pm 0.031$	$18.811 \pm 0.018$	$18.534 \pm 0.019$	$18.522 \pm 0.016$	$18.554 \pm 0.034$
140410.72+362056.8	2931-54590-302	2	$20.013 \pm 0.037$	$18.826 \pm 0.033$	$18.455 \pm 0.016$	$18.512 \pm 0.021$	$18.701 \pm 0.034$
140525.20+254212.4	6008-56093-808	1	$23.292 \pm 0.413$	$20.956 \pm 0.034$	$20.719 \pm 0.031$	$20.719 \pm 0.048$	$20.781 \pm 0.188$
140557.09+154940.5	2744-54272-586	2	$20.003 \pm 0.037$	$18.935 \pm 0.020$	$18.779 \pm 0.019$	$18.911 \pm 0.016$	$19.107 \pm 0.037$
141140.27+341039.4	3863-55280-502	1	$24.960 \pm 0.815$	$20.790 \pm 0.030$	$20.084 \pm 0.023$	$20.021 \pm 0.029$	$19.843 \pm 0.106$
141211.53+283618.7	6497-56329-380	1	$24.999 \pm 0.896$	$21.386 \pm 0.051$	$20.590 \pm 0.033$	$20.519 \pm 0.045$	$20.290 \pm 0.127$
142120.11+184351.6	5897-56042-460	2	$22.057 \pm 0.144$	$20.351 \pm 0.028$	$20.083 \pm 0.023$	$20.190 \pm 0.037$	$20.340 \pm 0.111$
142833.77+440346.1	2907-54580-126	1	$17.900 \pm 0.020$	$17.055 \pm 0.016$	$16.878 \pm 0.016$	$16.938 \pm 0.016$	$17.053 \pm 0.022$
142939.38+384113.2	4713-56044-876	1	$22.256 \pm 0.158$	$20.642 \pm 0.028$	$20.399 \pm 0.025$	$20.332 \pm 0.033$	$20.384 \pm 0.100$
143007.15-015129.5	0919-52409-358	1	$21.484 \pm 0.121$	$19.477 \pm 0.022$	$19.033 \pm 0.021$	$18.994 \pm 0.019$	$19.102 \pm 0.057$
144301.55+583301.6	6806-56419-314	1	$22.498 \pm 0.287$	$21.347 \pm 0.041$	$21.262 \pm 0.065$	$21.339 \pm 0.101$	$22.078 \pm 0.727$
144354.13+301413.3	3874-55280-732	1	$22.674 \pm 0.248$	$21.478 \pm 0.047$	$21.273 \pm 0.051$	$21.402 \pm 0.083$	$21.361 \pm 0.248$
144535.03+091340.4	5472-55976-842	1	$22.544 \pm 0.368$	$21.314 \pm 0.047$	$21.033 \pm 0.046$	$21.197 \pm 0.069$	$21.493 \pm 0.356$
144804.49+104709.0	5475-56011-394	2	$20.185 \pm 0.042$	$18.814 \pm 0.016$	$18.651 \pm 0.016$	$18.673 \pm 0.019$	$18.748 \pm 0.033$
150028.02+231554.0	6020-56087-828	1	$24.096 \pm 0.883$	$21.596 \pm 0.051$	$21.381 \pm 0.060$	$21.460 \pm 0.098$	$21.819 \pm 0.564$
150228.70+374452.9	5168-56035-732	2	$21.576 \pm 0.092$	$19.788 \pm 0.018$	$19.455 \pm 0.023$	$19.418 \pm 0.029$	$19.511 \pm 0.047$
150739.03+403408.9	6054-56089-176	1	$22.151 \pm 0.204$	$21.081 \pm 0.043$	$20.941 \pm 0.046$	$21.081 \pm 0.089$	$21.429 \pm 0.393$
151835.63+050627.4	1834-54562-231	1	$21.942 \pm 0.174$	$19.451 \pm 0.019$	$18.861 \pm 0.018$	$18.786 \pm 0.018$	$18.771 \pm 0.040$
152449.58+404938.1	2936-54626-537	4	$21.788 \pm 0.110$	$20.150 \pm 0.024$	$19.760 \pm 0.023$	$19.800 \pm 0.029$	$19.921 \pm 0.095$
153407.58+124254.4	4891-55736-812	1	$23.178 \pm 0.537$	$21.594 \pm 0.059$	$21.151 \pm 0.054$	$21.099 \pm 0.071$	$20.988 \pm 0.262$
153505.75+124744.2	2754-54240-570	1	$18.043 \pm 0.021$	$15.981 \pm 0.020$	$15.498 \pm 0.017$	$15.453 \pm 0.021$	$15.497 \pm 0.014$
153642.53+420519.2	6050-56089-620	1	$23.322 \pm 0.650$	$20.840 \pm 0.043$	$20.303 \pm 0.031$	$20.172 \pm 0.041$	$20.334 \pm 0.159$
153745.52+360818.6	4974-56038-738	1	$23.360 \pm 0.417$	$21.112 \pm 0.032$	$20.674 \pm 0.031$	$20.658 \pm 0.041$	$20.854 \pm 0.140$
154022.79+535239.8	6708-56452-298	1	$22.890 \pm 0.282$	$21.156 \pm 0.035$	$20.952 \pm 0.042$	$20.990 \pm 0.054$	$21.255 \pm 0.239$
154201.75+465020.2	6032-56067-716	1	$23.013 \pm 0.532$	$20.853 \pm 0.045$	$20.424 \pm 0.033$	$20.416 \pm 0.041$	$20.704 \pm 0.188$
154349.79+202442.9	3943-55336-100	1	$23.081 \pm 0.437$	$21.471 \pm 0.043$	$21.089 \pm 0.046$	$21.205 \pm 0.080$	$21.215 \pm 0.336$
154510.31+523618.4	6715-56449-768	1	$21.589 \pm 0.105$	$20.055 \pm 0.028$	$19.697 \pm 0.021$	$19.711 \pm 0.025$	$19.795 \pm 0.068$
154625.33+300946.2	4726-55712-632	2	$21.430 \pm 0.077$	$19.802 \pm 0.022$	$19.530 \pm 0.018$	$19.641 \pm 0.022$	$19.802 \pm 0.064$
154913.45+263301.1	3946-55659-698	1	$21.447 \pm 0.102$	$20.592 \pm 0.031$	$20.548 \pm 0.043$	$20.409 \pm 0.039$	$20.586 \pm 0.194$
154933.23+190646.7	3931-55350-572	1	$22.631 \pm 0.332$	$21.321 \pm 0.045$	$20.949 \pm 0.047$	$20.971 \pm 0.065$	$20.851 \pm 0.262$
155429.00+173545.9	2170-53875-154	1	$18.674 \pm 0.023$	$17.592 \pm 0.016$	$17.418 \pm 0.011$	$17.468 \pm 0.011$	$17.654 \pm 0.023$

SDSS J	Plate-MJD-Fib	$N_{\text{SDSS}}$	$u$	$g$	$r$	$i$	$z$
160429.80+183035.4	3289-54910-379	1	$20.702 \pm 0.063$	$19.701 \pm 0.020$	$19.552 \pm 0.018$	$19.607 \pm 0.023$	$19.765 \pm 0.087$
161026.10+400619.7	6052-56092-036	1	$22.578 \pm 0.211$	$21.000 \pm 0.029$	$20.749 \pm 0.033$	$20.915 \pm 0.049$	$21.093 \pm 0.237$
161248.17+353434.8	4964-55749-238	1	$22.381 \pm 0.209$	$21.306 \pm 0.042$	$21.305 \pm 0.052$	$21.311 \pm 0.071$	$21.257 \pm 0.972$
161603.00+330301.3	4960-55747-224	2	$21.021 \pm 0.082$	$19.251 \pm 0.020$	$18.976 \pm 0.021$	$19.070 \pm 0.021$	$19.152 \pm 0.047$
162408.57+331019.0	4955-55750-650	1	$22.261 \pm 0.179$	$21.125 \pm 0.035$	$20.963 \pm 0.037$	$21.061 \pm 0.060$	$20.759 \pm 0.147$
162612.73+330308.2	4955-55750-774	1	$22.129 \pm 0.248$	$20.989 \pm 0.038$	$20.786 \pm 0.041$	$20.876 \pm 0.064$	$20.505 \pm 0.151$
162703.34+464658.2	6029-56099-975	2	$22.015 \pm 0.148$	$20.422 \pm 0.023$	$20.129 \pm 0.023$	$20.152 \pm 0.034$	$20.343 \pm 0.109$
163601.33+161907.1	4063-55364-316	2	$23.428 \pm 0.508$	$20.636 \pm 0.028$	$19.535 \pm 0.019$	$19.292 \pm 0.018$	$19.303 \pm 0.049$
164104.94+185602.1	4062-55383-728	1	$21.832 \pm 0.133$	$20.223 \pm 0.021$	$19.848 \pm 0.018$	$19.750 \pm 0.022$	$19.806 \pm 0.069$
164939.22+223807.2	4182-55446-900	1	$23.670 \pm 0.461$	$21.000 \pm 0.029$	$20.349 \pm 0.023$	$20.137 \pm 0.026$	$20.160 \pm 0.085$
165101.72+424955.5	6031-56091-046	1	$22.511 \pm 0.231$	$19.796 \pm 0.018$	$19.196 \pm 0.015$	$19.021 \pm 0.015$	$19.119 \pm 0.048$
170638.11+254111.7	5014-55717-420	1	$25.149 \pm 1.586$	$20.981 \pm 0.040$	$20.912 \pm 0.061$	$20.957 \pm 0.092$	$20.537 \pm 0.237$
210916.51-003921.6	0985-52431-104	1	$21.864 \pm 0.147$	$20.058 \pm 0.019$	$19.763 \pm 0.017$	$19.758 \pm 0.025$	$19.672 \pm 0.066$
211045.34+051214.8	4078-55358-358	1	$23.319 \pm 0.389$	$21.531 \pm 0.044$	$21.147 \pm 0.043$	$21.072 \pm 0.051$	$21.099 \pm 0.212$
212312.20+001653.5	4192-55469-974	3	$22.403 \pm 0.182$	$20.322 \pm 0.021$	$19.902 \pm 0.020$	$19.762 \pm 0.030$	$19.616 \pm 0.075$
215752.30+120603.1	5063-55831-628	1	$21.257 \pm 0.096$	$19.739 \pm 0.021$	$19.406 \pm 0.018$	$19.346 \pm 0.024$	$19.383 \pm 0.049$
222503.70+233855.1	6299-56478-666	1	$21.188 \pm 0.162$	$19.486 \pm 0.023$	$19.269 \pm 0.023$	$19.273 \pm 0.035$	$19.536 \pm 0.124$
223014.70+190514.4	5025-55836-498	1	$23.215 \pm 0.557$	$20.869 \pm 0.038$	$20.256 \pm 0.034$	$20.172 \pm 0.042$	$20.271 \pm 0.153$
223101.11+090635.1	5057-56209-944	2	$20.701 \pm 0.087$	$19.288 \pm 0.016$	$18.937 \pm 0.014$	$18.838 \pm 0.015$	$18.781 \pm 0.043$
223507.65-005607.7	4203-55447-092	1	$22.269 \pm 0.221$	$20.492 \pm 0.031$	$20.209 \pm 0.024$	$20.296 \pm 0.036$	$20.418 \pm 0.145$
223811.10+021352.9	4295-55858-413	1	$21.575 \pm 0.136$	$20.734 \pm 0.033$	$20.544 \pm 0.034$	$20.550 \pm 0.039$	$20.316 \pm 0.120$
223815.97-011336.9	4204-55470-321	1	$22.381 \pm 0.265$	$20.784 \pm 0.040$	$20.587 \pm 0.035$	$20.617 \pm 0.049$	$20.681 \pm 0.172$
225448.83+303107.1	6507-56478-276	1	$22.457 \pm 0.277$	$19.861 \pm 0.020$	$19.326 \pm 0.022$	$19.236 \pm 0.021$	$19.300 \pm 0.059$
230414.48+241554.0	6589-56536-655	1	$22.017 \pm 0.162$	$19.847 \pm 0.021$	$19.172 \pm 0.015$	$19.037 \pm 0.016$	$18.958 \pm 0.045$
231937.39+301848.4	6583-56566-754	2	$21.670 \pm 0.141$	$20.870 \pm 0.029$	$20.811 \pm 0.040$	$20.861 \pm 0.062$	$20.715 \pm 0.185$
232538.93+044813.1	4408-55888-256	1	$21.438 \pm 0.151$	$19.882 \pm 0.025$	$19.578 \pm 0.029$	$19.682 \pm 0.035$	$19.688 \pm 0.114$
232833.31+083028.4	6164-56181-140	1	$23.212 \pm 0.563$	$21.591 \pm 0.053$	$21.010 \pm 0.046$	$21.044 \pm 0.098$	$21.076 \pm 0.299$
233054.31+280517.4	6514-56487-489	1	$22.075 \pm 0.263$	$20.773 \pm 0.032$	$20.556 \pm 0.042$	$20.526 \pm 0.064$	$20.349 \pm 0.188$
233056.81+295652.6	6501-56563-406	1	$21.341 \pm 0.090$	$19.842 \pm 0.020$	$19.644 \pm 0.017$	$19.712 \pm 0.022$	$19.951 \pm 0.097$
233320.38+105830.2	6157-56238-852	1	$23.395 \pm 0.885$	$21.457 \pm 0.041$	$21.179 \pm 0.044$	$21.272 \pm 0.072$	$21.306 \pm 0.269$
234034.61+012416.6	4280-55503-444	1	$21.098 \pm 0.076$	$19.401 \pm 0.024$	$19.079 \pm 0.021$	$19.148 \pm 0.021$	$19.199 \pm 0.045$
234048.74+081753.3	2628-54326-108	3	$22.677 \pm 1.028$	$20.246 \pm 0.021$	$19.806 \pm 0.022$	$19.858 \pm 0.026$	$19.932 \pm 0.074$
234307.67-001016.3	4214-55451-438	1	$22.109 \pm 0.170$	$20.459 \pm 0.029$	$20.073 \pm 0.024$	$20.110 \pm 0.030$	$20.081 \pm 0.104$
235224.26+192247.3	6127-56274-424	1	$24.800 \pm 1.329$	$21.350 \pm 0.046$	$20.912 \pm 0.049$	$20.994 \pm 0.074$	$21.483 \pm 0.917$
235249.13+334439.2	7143-56572-070	1	$21.741 \pm 0.114$	$20.954 \pm 0.027$	$20.746 \pm 0.029$	$20.816 \pm 0.043$	$20.713 \pm 0.172$
235715.03+234848.9	6513-56543-314	1	$23.001 \pm 0.553$	$21.263 \pm 0.051$	$20.906 \pm 0.048$	$20.920 \pm 0.073$	$21.200 \pm 0.316$

Table A2: Derived parameters from atmospheric modelling of the SDSS and WHT spectra. Abundances relative to helium are given in dex.

SDSS J	$T_{\text{eff}}$ [K]	Ca	Mg	Fe	Na	Cr	Ti	Ni	H
0002+3209	6410 $\pm$ 180	-9.05	-8.14	-7.84	-	-	-	-	-
0004+0819	5820 $\pm$ 380	-8.72	-7.51	-7.51	-8.80	-	-	-	-
0006+0520	6790 $\pm$ 170	-9.00	-8.09	-8.39	-	-	-	-	-
0010-0430	6960 $\pm$ 160	-8.38	-6.92	-7.12	-	-	-	-	-
0013+1109	5830 $\pm$ 320	-9.11	-8.20	-8.10	-	-	-	-	-
0019+2209	5970 $\pm$ 150	-9.34	-8.53	-8.58	-9.42	-	-	-	-
0037-0525	5630 $\pm$ 120	-8.79	-7.58	-7.68	-9.07	-	-	-	-
0044+0418	6050 $\pm$ 70	-9.82	-8.81	-8.71	-	-	-	-	-
0046+2717	7640 $\pm$ 290	-7.65	-6.19	-6.84	-	-7.80	-	-	-
0047+1628	6620 $\pm$ 180	-7.68	-6.77	-6.47	-8.66	-8.53	-	-	-
0052+1846	5660 $\pm$ 290	-9.04	-7.83	-7.53	-	-9.59	-	-	-
0053+3115	6180 $\pm$ 320	-8.87	-8.26	-8.66	-	-	-	-	-
0056+2453	5440 $\pm$ 310	-9.62	-8.61	-8.71	-	-	-	-	-
0107+2650	6190 $\pm$ 140	-8.44	-7.93	-7.73	-8.22	-	-	-	-
0108-0537	6010 $\pm$ 130	-8.79	-8.18	-8.08	-9.27	-	-	-	-
0114+3505	6370 $\pm$ 210	-8.51	-7.30	-7.20	-	-9.06	-	-	-
0116+2050	6207 $\pm$ 80	-8.81	-7.65	-7.60	-9.29	-	-9.74	-8.76	-
0117+0021	6800 $\pm$ 80	-8.80	-7.50	-7.60	-	-9.48	-	-	-
0126+2534	5320 $\pm$ 120	-9.95	-8.94	-8.64	-	-	-	-	-
0135+1302	5800 $\pm$ 100	-9.50	-8.70	-8.69	-	-	-	-	-
0143+0113	6700 $\pm$ 80	-8.50	-7.10	-7.30	-8.68	-	-	-	-3.1
0144+1920	6500 $\pm$ 190	-8.50	-7.34	-7.39	-8.18	-	-	-	-
0144+0305	6950 $\pm$ 330	-8.37	-7.21	-7.26	-	-	-	-	-
0148-0112	6830 $\pm$ 210	-8.82	-7.56	-7.31	-	-	-	-	-
0150+1354	6310 $\pm$ 160	-7.75	-6.54	-7.24	-8.03	-10.10	-	-	-1.7
0157+0033	6110 $\pm$ 140	-8.20	-7.39	-7.69	-	-	-	-	-
0158-0942	5940 $\pm$ 170	-9.52	-8.61	-8.41	-	-	-	-	-
0200+1646	5810 $\pm$ 180	-8.92	-7.61	-7.91	-9.00	-	-	-	-
0201+2015	6180 $\pm$ 140	-8.96	-7.65	-8.25	-	-	-	-	-
0208-0542	5800 $\pm$ 350	-8.54	-7.53	-7.33	-8.82	-	-	-	-
0234-0510	7050 $\pm$ 340	-8.27	-6.91	-7.21	-	-	-	-	-
0252-0401	6950 $\pm$ 160	-8.57	-6.96	-7.46	-8.25	-8.62	-	-	-
0252+0054	7500 $\pm$ 190	-8.35	-7.24	-7.14	-7.83	-	-	-	$\leq -4.3$
0447+1124	6530 $\pm$ 190	-8.77	-7.26	-8.06	-	-	-	-	-2.5
0512-0505	5563 $\pm$ 60	-8.99	-8.05	-7.79	-9.65	-10.09	-	-	-
0721+3928	6280 $\pm$ 150	-8.90	-7.79	-8.09	-	-	-	-	-
0735+2057	6110 $\pm$ 180	-7.75	-6.74	-6.84	-8.33	-	-	-	-
0736+4118	5100 $\pm$ 100	-8.50	-7.69	-7.69	-9.68	-8.95	-	-	-3.0
0739+3112	5080 $\pm$ 320	-9.50	-8.29	-8.39	-	-	-	-	-
0741+3146	5592 $\pm$ 140	-9.55	-8.94	-7.50	-	-9.60	-10.06	-9.09	-
0744+4649	5028 $\pm$ 70	-8.36	-7.99	-8.17	-9.26	-9.69	-9.38	-	-
0744+4408	6370 $\pm$ 230	-8.75	-7.64	-7.54	-9.23	-	-	-	-
0744+2701	7890 $\pm$ 210	-7.68	-6.92	-6.87	-	-	-	-	$\leq -4.3$
0744+1640	4940 $\pm$ 190	-10.24	-8.63	-9.33	-	-	-	-	-
0758+1013	5500 $\pm$ 290	-8.65	-7.54	-7.34	-8.73	-9.20	-	-	-
0800+2242	6260 $\pm$ 260	-9.75	-8.69	-8.69	-	-	-	-	-
0806+3055	6900 $\pm$ 250	-7.77	-7.01	-7.16	-	-8.47	-	-	-
0806+4058	6808 $\pm$ 80	-8.49	-7.38	-7.49	-8.33	-9.11	-	-9.00	-
0807+4930	5100 $\pm$ 250	-8.39	-7.58	-7.28	-9.27	-9.34	-9.06	-	-
0816+2330	7790 $\pm$ 300	-7.48	-6.27	-6.37	-	-7.68	-8.65	-	$\leq -4.5$
0818+1247	6810 $\pm$ 270	-8.58	-7.87	-7.77	-	-	-	-	-
0823+0546	6019 $\pm$ 60	-9.34	-8.51	-7.36	-	-	-9.90	-8.59	-
0830-0319	6400 $\pm$ 110	-9.10	-8.49	-8.29	-	-	-	-	-
0832+4109	6070 $\pm$ 190	-8.00	-7.04	-7.04	-8.73	-8.80	-	-	-
0838+2322	5670 $\pm$ 80	-9.80	-8.89	-9.30	-	-	-	-	-
0842+1406	7160 $\pm$ 90	-8.16	-7.20	-7.30	-	-	-	-	-
0842+1536	6180 $\pm$ 220	-9.47	-8.46	-8.46	-	-	-	-	-
0843+5614	6600 $\pm$ 170	-8.65	-7.44	-7.74	-8.23	-	-	-	-
0851+1543	6300 $\pm$ 90	-8.50	-7.89	-8.20	-	-	-	-	-
0852+3402	5580 $\pm$ 180	-9.00	-8.39	-7.79	-9.58	-9.75	-	-	-
0901+0752	7100 $\pm$ 120	-7.12	-6.21	-6.21	-7.70	-8.07	-8.79	-	-
0902+3625	6330 $\pm$ 210	-8.60	-7.54	-7.64	-8.53	-	-	-	-
0902+1004	7250 $\pm$ 250	-8.25	-7.29	-8.19	-	-	-	-	-
0906+1141	6910 $\pm$ 270	-7.90	-6.64	-6.94	-8.43	-	-8.62	-	-



SDSS J	$T_{\text{eff}}$ [K]	Ca	Mg	Fe	Na	Cr	Ti	Ni	H
0908+5136	6180 $\pm$ 90	-9.35	-8.50	-8.24	-	-	-	-	-
0908+4119	6700 $\pm$ 300	-8.73	-7.07	-7.12	-	-	-	-	-
0913+2627	5210 $\pm$ 180	-9.75	-8.74	-8.64	-	-	-	-	-
0913+4127	5780 $\pm$ 290	-8.52	-7.86	-7.16	-	-9.42	-9.04	-	-
0916+2540	5378 $\pm$ 70	-7.48	-6.83	-7.09	-9.32	-8.90	-8.75	-	-
0924+4301	5950 $\pm$ 240	-9.75	-8.44	-8.54	-	-	-	-	-
0925+3130	5810 $\pm$ 90	-9.00	-7.79	-7.99	-9.68	-	-	-	-
0927+4931	6200 $\pm$ 230	-8.61	-7.20	-7.50	-9.09	-	-	-	-
0929+4247	6530 $\pm$ 160	-8.46	-6.85	-7.15	-8.64	-9.01	-	-	-
0933+6334	6290 $\pm$ 370	-8.28	-7.17	-6.77	-	-8.83	-	-	-
0937+5228	6600 $\pm$ 100	-8.40	-7.09	-7.50	-8.98	-9.25	-	-	-
0939+4136	6310 $\pm$ 180	-8.30	-7.09	-6.79	-8.58	-8.55	-	-	-
0939+5019	5980 $\pm$ 190	-8.25	-7.04	-7.14	-9.23	-8.70	-	-	-
0946+2024	7490 $\pm$ 390	-8.07	-6.66	-7.06	-	-	-	-	-
0948+3008	6000 $\pm$ 130	-9.15	-8.04	-8.44	-	-	-	-	-
0956+5912	8800 $\pm$ 110	-7.15	-5.30	-6.14	-6.60	-7.50	-	-	-3.6
1003-0031	5740 $\pm$ 140	-8.49	-7.28	-7.28	-8.97	-	-	-	-
1005+2244	6360 $\pm$ 320	-8.96	-8.10	-7.40	-	-	-	-	-
1006+1752	5710 $\pm$ 190	-9.45	-8.94	-8.34	-	-	-	-	-
1014+2827	6250 $\pm$ 330	-7.68	-6.47	-6.47	-7.86	-8.43	-9.05	-	-
1017+3447	6150 $\pm$ 190	-9.34	-8.43	-8.33	-	-	-	-	-
1017+2419	7200 $\pm$ 150	-8.07	-6.86	-6.96	-8.15	-	-	-	$\leq -4.3$
1019+3535	5840 $\pm$ 270	-8.75	-7.64	-7.74	-	-	-	-	-
1019+2045	5300 $\pm$ 220	-9.36	-8.65	-8.25	-	-	-	-	-
1024+4531	5980 $\pm$ 160	-8.92	-8.06	-8.11	-	-	-	-	-
1024+1014	6310 $\pm$ 280	-7.50	-6.54	-6.64	-8.63	-8.40	-8.52	-	-
1032+1338	5490 $\pm$ 240	-9.33	-7.82	-8.02	-9.01	-	-	-	-
1033+1809	6070 $\pm$ 230	-8.55	-8.84	-8.04	-	-	-	-	-
1038-0036	7700 $\pm$ 60	-7.85	-6.80	-7.40	-8.60	-	-9.60	-	$\leq -4.8$
1038+0432	6510 $\pm$ 170	-7.50	-6.84	-6.99	-9.13	-8.70	-	-	-
1040+2407	5750 $\pm$ 90	-8.20	-7.29	-7.59	-8.88	-9.35	-9.27	-	-
1041+3432	7500 $\pm$ 220	-8.20	-7.49	-7.29	-	-	-	-	-
1043+3516	6720 $\pm$ 120	-8.88	-8.00	-7.20	-	-8.92	-10.54	-8.55	-
1046+1329	5170 $\pm$ 230	-9.60	-8.39	-8.29	-	-	-	-	-
1055+3725	5600 $\pm$ 120	-8.24	-8.23	-7.83	-	-9.19	-	-	-
1058+3143	6850 $\pm$ 100	-9.02	-7.81	-8.01	-	-	-	-	-
1102+2827	6400 $\pm$ 380	-7.75	-6.24	-6.44	-7.73	-8.30	-	-	-
1102+0214	5730 $\pm$ 90	-9.75	-8.84	-8.74	-	-	-	-	-
1103+4144	5850 $\pm$ 100	-9.30	-7.94	-8.04	-9.13	-	-	-	-
1105+5006	7280 $\pm$ 190	-8.14	-6.83	-6.93	-	-	-	-	-
1105+0228	5780 $\pm$ 260	-9.10	-7.84	-8.14	-	-	-	-	-
1106+6737	6400 $\pm$ 170	-7.88	-6.87	-7.67	-9.36	-	-	-	-
1112+0700	7560 $\pm$ 170	-8.53	-7.12	-7.37	-8.76	-	-	-	$\leq -4.6$
1113+2751	6180 $\pm$ 210	-8.42	-7.41	-7.51	-9.20	-	-	-	-
1132+3323	6250 $\pm$ 270	-8.23	-6.82	-7.32	-8.71	-8.88	-8.70	-	-
1134+1542	6680 $\pm$ 250	-8.46	-7.25	-7.35	-8.44	-	-	-	-
1144+3720	7490 $\pm$ 190	-8.17	-6.96	-7.16	-8.25	-	-	-	-
1144+1218	5434 $\pm$ 100	-9.33	-8.13	-8.37	-	-10.22	-	-10.13	-3.3
1147+5429	5320 $\pm$ 340	-9.17	-8.16	-8.06	-9.85	-	-	-	-
1149+0519	7310 $\pm$ 140	-8.16	-7.30	-7.60	-	-	-	-	$\leq -4.3$
1150+4928	7210 $\pm$ 160	-8.76	-7.95	-7.65	-	-	-	-	-
1150+4533	5720 $\pm$ 320	-8.35	-7.14	-7.14	-8.53	-	-	-	-
1152+5101	5000 $\pm$ 240	-10.08	-8.67	-8.97	-	-	-	-	-
1152+1605	6550 $\pm$ 160	-8.40	-7.19	-7.19	-8.28	-	-	-	-
1157+6138	6540 $\pm$ 380	-9.15	-7.44	-7.64	-	-	-	-	-
1158+1845	7250 $\pm$ 170	-7.75	-5.74	-6.84	-	-	-	-	-
1158+5942	6000 $\pm$ 170	-8.98	-8.72	-8.02	-	-	-	-	-
1158+0454	5270 $\pm$ 180	-8.69	-7.68	-7.58	-8.97	-9.34	-9.46	-	-
1158+4712	7650 $\pm$ 210	-8.06	-6.90	-6.85	-	-	-	-	-
1158+5448	6280 $\pm$ 340	-8.82	-7.61	-7.61	-	-	-	-	-
1205+3536	6070 $\pm$ 150	-8.74	-7.43	-7.63	-8.72	-	-	-	-
1211+2326	6450 $\pm$ 230	-8.59	-7.28	-7.28	-8.57	-	-	-	-
1214-0234	5210 $\pm$ 100	-9.40	-8.19	-8.49	-8.98	-	-	-	-
1217+1157	6440 $\pm$ 150	-8.93	-7.52	-7.92	-	-	-	-	-
1218+0023	6100 $\pm$ 90	-9.61	-9.20	-8.90	-	-	-	-	-
1220+0929	6640 $\pm$ 150	-8.38	-7.07	-7.37	-8.46	-8.93	-	-	-
1224+2838	5210 $\pm$ 110	-10.00	-8.69	-8.89	-	-	-	-	-

SDSS J	$T_{\text{eff}}$ [K]	Ca	Mg	Fe	Na	Cr	Ti	Ni	H
1226+2936	4680 $\pm$ 240	-10.04	-8.63	-8.93	-	-	-	-	-
1229+0743	6160 $\pm$ 130	-8.20	-7.29	-7.09	-8.48	-8.85	-9.87	-	-
1230+3143	6510 $\pm$ 160	-9.12	-8.41	-8.21	-	-	-	-	-
1234+5208	7630 $\pm$ 100	-7.40	-6.00	-6.39	-7.90	-7.95	-8.87	-	$\leq -4.9$
1238+2149	5440 $\pm$ 190	-9.11	-8.10	-8.00	-8.89	-	-	-	-
1245+0822	6360 $\pm$ 190	-8.10	-7.34	-7.59	-8.68	-	-	-	-
1249+6514	7540 $\pm$ 170	-8.50	-6.89	-7.49	-	-	-	-	-
1254+3551	6620 $\pm$ 210	-8.96	-7.55	-7.75	-	-	-	-	-
1257+3238	5210 $\pm$ 340	-9.02	-7.81	-7.61	-9.70	-	-	-	-
1257-0310	6280 $\pm$ 230	-8.52	-7.26	-7.31	-	-	-	-	-
1259+3112	5840 $\pm$ 240	-9.65	-8.74	-8.14	-	-	-	-	-
1259+4729	6260 $\pm$ 290	-8.80	-8.29	-7.99	-	-	-	-	-
1303+4055	6200 $\pm$ 120	-9.02	-7.71	-8.11	-	-	-	-	-
1308+0957	7830 $\pm$ 320	-8.03	-7.52	-6.62	-	-	-	-	-3.6
1308+0258	6030 $\pm$ 210	-9.07	-8.16	-7.66	-	-	-	-	-
1314+3748	5940 $\pm$ 320	-8.48	-7.42	-7.52	-8.71	-	-	-	-
1316+1918	5350 $\pm$ 190	-9.90	-8.49	-8.99	-	-	-	-	-
1319+3641	7360 $\pm$ 190	-8.60	-7.59	-7.49	-	-	-	-	-
1320+0204	7000 $\pm$ 310	-8.28	-7.37	-7.17	-7.96	-	-	-	-
1321-0237	5620 $\pm$ 240	-8.48	-7.47	-7.47	-8.36	-9.33	-	-	-
1329+1301	6810 $\pm$ 150	-8.55	-7.34	-7.44	-9.23	-	-	-	-
1330+3029	6100 $\pm$ 60	-8.40	-7.15	-7.30	-8.80	-9.00	-9.70	-8.66	-
1336+3547	6600 $\pm$ 70	-8.50	-7.10	-7.39	-9.00	-9.40	-	-	-
1339+2643	6300 $\pm$ 70	-9.13	-8.30	-8.60	-	-	-	-	-
1340+2702	7855 $\pm$ 260	-6.98	-5.73	-6.27	-7.41	-	-	-	-
1342+1813	5240 $\pm$ 220	-9.19	-8.68	-8.58	-	-	-	-	-
1345+1153	6020 $\pm$ 200	-8.10	-7.49	-6.89	-	-8.70	-9.07	-	-
1347+1415	6740 $\pm$ 120	-8.50	-7.19	-7.29	-	-8.75	-	-	-
1350+1058	5120 $\pm$ 170	-10.06	-8.85	-8.75	-	-	-	-	-
1351+2645	5980 $\pm$ 160	-8.04	-8.33	-7.53	-9.72	-9.19	-8.61	-	-
1356+2416	6030 $\pm$ 120	-9.20	-7.84	-8.54	-	-	-	-	-
1356+0236	8260 $\pm$ 180	-7.52	-6.21	-6.41	-8.00	-	-	-	$\leq -4.2$
1401+3659	6000 $\pm$ 110	-9.80	-8.84	-8.94	-	-	-	-	-
1404+3620	5900 $\pm$ 70	-9.20	-7.90	-8.50	-	-	-	-	-
1405+2542	5880 $\pm$ 190	-9.50	-8.49	-8.39	-	-	-	-	-
1405+1549	7150 $\pm$ 110	-8.25	-7.14	-7.14	-8.93	-	-	-	-
1411+3410	5480 $\pm$ 210	-8.40	-7.24	-7.39	-9.28	-9.15	-	-	-
1412+2836	4990 $\pm$ 160	-9.40	-8.39	-7.99	-9.58	-	-	-	-
1421+1843	7300 $\pm$ 210	-7.35	-5.89	-6.19	-	-	-	-	-
1428+4403	6600 $\pm$ 60	-8.98	-8.20	-8.40	-	-	-	-	-
1429+3841	6040 $\pm$ 270	-9.73	-8.72	-8.72	-	-	-	-	-
1430-0151	6150 $\pm$ 160	-7.55	-6.54	-6.99	-8.13	-8.50	-8.80	-	-
1443+5833	7080 $\pm$ 340	-8.56	-7.15	-7.25	-	-	-	-	-
1443+3014	6840 $\pm$ 300	-8.16	-6.90	-7.15	-	-	-	-	-
1445+0913	6580 $\pm$ 230	-7.98	-6.77	-6.77	-7.81	-8.58	-	-	-
1448+1047	6550 $\pm$ 100	-8.85	-7.77	-7.80	-	-	-	-	-
1500+2315	6530 $\pm$ 430	-8.40	-6.89	-7.19	-	-	-	-	-
1502+3744	5410 $\pm$ 100	-10.00	-8.99	-8.99	-	-	-	-	-
1507+4034	7180 $\pm$ 330	-8.18	-6.57	-7.17	-	-	-	-	-
1518+0506	5020 $\pm$ 100	-9.65	-8.64	-8.74	-10.03	-	-	-	-
1524+4049	5900 $\pm$ 120	-8.90	-7.69	-7.79	-9.18	-9.65	-	-	-
1534+1242	5860 $\pm$ 340	-8.29	-7.78	-7.48	-	-	-	-	-
1535+1247	5773 $\pm$ 50	-8.61	-7.36	-7.57	-8.72	-9.25	-9.62	-8.90	$\leq -3.0$
1536+4205	5800 $\pm$ 140	-8.70	-7.49	-7.59	-8.78	-8.90	-8.90	-	-
1537+3608	5570 $\pm$ 270	-9.50	-8.19	-8.49	-	-	-	-	-
1540+5352	6520 $\pm$ 360	-8.58	-7.07	-7.47	-	-	-	-	-
1542+4650	6060 $\pm$ 220	-8.15	-6.94	-7.04	-8.18	-8.70	-	-	-
1543+2024	6330 $\pm$ 360	-8.09	-7.33	-7.38	-	-	-	-	-
1545+5236	5840 $\pm$ 120	-9.19	-8.28	-8.18	-	-	-	-	-
1546+3009	6600 $\pm$ 120	-8.40	-7.19	-7.19	-8.78	-8.65	-	-	-
1549+2633	6290 $\pm$ 180	-9.66	-7.95	-8.25	-	-	-	-	-
1549+1906	6460 $\pm$ 290	-8.48	-7.17	-7.22	-9.11	-8.78	-	-	-
1554+1735	6630 $\pm$ 70	-8.60	-7.54	-7.64	-8.90	-	-	-	-
1604+1830	6400 $\pm$ 120	-9.48	-8.47	-8.57	-	-	-	-	-
1610+4006	6580 $\pm$ 280	-8.47	-7.46	-7.11	-	-	-	-	-
1612+3534	6750 $\pm$ 400	-8.54	-7.43	-7.53	-	-	-	-	-
1616+3303	6400 $\pm$ 80	-8.25	-6.95	-7.14	-8.93	-8.80	-9.62	-	-

SDSS J	$T_{\text{eff}}$ [K]	Ca	Mg	Fe	Na	Cr	Ti	Ni	H
1624+3310	6930 $\pm$ 340	−8.64	−7.28	−7.53	-	-	-	-	-
1626+3303	6260 $\pm$ 250	−8.87	−7.41	−7.61	-	-	−9.04	-	-
1627+4646	6420 $\pm$ 200	−8.88	−8.07	−7.62	-	−8.73	-	-	-
1636+1619	4410 $\pm$ 150	−9.50	−8.29	−8.79	−10.18	-	-	-	-
1641+1856	5820 $\pm$ 100	−10.30	−9.49	−9.59	-	-	-	-	-
1649+2238	5332 $\pm$ 160	−8.62	−6.89	−7.21	−8.29	−8.83	-	-	−1.8
1651+4249	5710 $\pm$ 200	−8.02	−6.91	−7.31	−8.20	-	-	-	-
1706+2541	6640 $\pm$ 260	−9.40	−8.49	−8.89	-	-	-	-	-
2109−0039	6040 $\pm$ 240	−8.78	−8.42	−7.67	-	-	-	-	-
2110+0512	5680 $\pm$ 260	−9.21	−8.10	−8.00	-	-	-	-	-
2123+0016	5230 $\pm$ 140	−10.01	−8.50	−8.50	−9.19	-	-	-	-
2157+1206	6100 $\pm$ 100	−9.00	−7.79	−8.09	−9.18	-	-	-	-
2225+2338	7000 $\pm$ 130	−8.81	−7.40	−7.80	-	-	-	-	-
2230+1905	5600 $\pm$ 250	−8.45	−7.14	−7.24	−8.73	−8.90	-	-	-
2231+0906	5900 $\pm$ 90	−9.85	−9.24	−8.84	-	-	-	-	-
2235−0056	6340 $\pm$ 200	−8.67	−7.66	−7.26	−8.85	-	-	-	-
2238+0213	7000 $\pm$ 250	−8.56	−7.55	−7.30	-	-	-	-	-
2238−0113	6800 $\pm$ 260	−8.89	−7.73	−7.78	-	-	-	-	-
2254+3031	5900 $\pm$ 90	−8.26	−6.95	−7.25	−8.54	−9.01	-	-	-
2304+2415	5060 $\pm$ 100	−9.54	−7.98	−8.93	-	-	-	-	-
2319+3018	7120 $\pm$ 200	−8.53	−7.42	−7.37	−7.71	-	-	-	-
2325+0448	6020 $\pm$ 100	−9.07	−8.06	−8.06	−8.95	-	-	-	-
2328+0830	5800 $\pm$ 330	−8.80	−7.69	−7.59	-	-	-	-	-
2330+2805	6670 $\pm$ 210	−8.84	−7.73	−7.63	-	-	-	-	-
2330+2956	7000 $\pm$ 110	−8.24	−6.63	−7.13	−8.02	-	-	-	-
2333+1058	6220 $\pm$ 300	−8.79	−7.28	−7.38	−8.67	-	-	-	-
2340+0124	6200 $\pm$ 100	−8.50	−7.54	−7.90	-	-	-	-	-
2340+0817	5550 $\pm$ 120	−9.00	−7.99	−7.69	-	-	-	-	-
2343−0010	5900 $\pm$ 290	−9.23	−7.82	−8.22	-	-	-	-	-
2352+1922	6170 $\pm$ 310	−8.34	−7.13	−7.03	-	-	-	-	-
2352+3344	7230 $\pm$ 220	−8.26	−6.85	−7.05	−8.34	-	-	-	-
2357+2348	6030 $\pm$ 240	−9.07	−7.66	−7.76	-	-	-	-	-

Table A3: The mass fraction of the convection zone,  $q$ , and logarithm of the diffusion timescale in years for each element.

SDSS J	$\log(q)$	Ca	Mg	Fe	Na	Cr	Ti	Ni
0002+3209	-5.34	6.18	6.62	6.17	6.57	6.15	6.13	6.21
0004+0819	-5.51	6.05	6.51	6.05	6.46	6.03	6.01	6.09
0006+0520	-5.27	6.20	6.65	6.21	6.60	6.19	6.16	6.25
0010-0430	-5.32	6.15	6.58	6.16	6.53	6.13	6.11	6.19
0013+1109	-5.44	6.16	6.58	6.11	6.53	6.09	6.07	6.15
0019+2209	-5.38	6.25	6.63	6.16	6.58	6.14	6.12	6.19
0037-0525	-5.54	6.05	6.51	6.04	6.46	6.02	6.00	6.08
0044+0418	-5.30	6.39	6.71	6.23	6.66	6.20	6.18	6.26
0046+2717	-5.32	6.11	6.54	6.14	6.49	6.11	6.09	6.17
0047+1628	-5.51	6.01	6.43	6.02	6.39	6.00	5.97	6.06
0052+1846	-5.49	6.13	6.56	6.08	6.51	6.06	6.04	6.12
0053+3115	-5.41	6.12	6.58	6.12	6.53	6.10	6.08	6.16
0056+2453	-5.41	6.33	6.65	6.15	6.60	6.13	6.11	6.19
0107+2650	-5.48	6.06	6.51	6.06	6.46	6.04	6.02	6.10
0108-0537	-5.46	6.09	6.54	6.09	6.49	6.06	6.04	6.12
0114+3505	-5.43	6.09	6.54	6.10	6.49	6.08	6.05	6.13
0116+2050	-5.42	6.11	6.57	6.12	6.52	6.09	6.07	6.15
0117+0021	-5.30	6.18	6.63	6.19	6.58	6.17	6.14	6.22
0126+2534	-5.37	6.44	6.70	6.19	6.65	6.17	6.17	6.22
0135+1302	-5.38	6.30	6.65	6.16	6.60	6.14	6.12	6.20
0143+0113	-5.36	6.13	6.57	6.14	6.53	6.12	6.09	6.18
0144+1920	-5.40	6.11	6.55	6.12	6.50	6.09	6.07	6.15
0144+0305	-5.33	6.14	6.58	6.16	6.53	6.13	6.11	6.19
0148-0112	-5.29	6.19	6.63	6.19	6.58	6.17	6.15	6.23
0150+1354	-5.56	5.97	6.41	5.99	6.36	5.97	5.94	6.02
0157+0033	-5.54	6.01	6.45	6.02	6.41	6.00	5.97	6.05
0158-0942	-5.35	6.32	6.66	6.18	6.61	6.16	6.14	6.21
0200+1646	-5.48	6.09	6.55	6.08	6.50	6.06	6.04	6.12
0201+2015	-5.40	6.13	6.59	6.13	6.54	6.11	6.09	6.17
0208-0542	-5.55	6.02	6.48	6.02	6.43	6.00	5.98	6.06
0234-0510	-5.32	6.14	6.58	6.16	6.53	6.13	6.11	6.19
0252-0401	-5.30	6.17	6.60	6.18	6.56	6.16	6.13	6.21
0252+0054	-5.23	6.19	6.62	6.21	6.58	6.19	6.16	6.25
0447+1124	-5.35	6.15	6.59	6.15	6.55	6.13	6.11	6.19
0512-0505	-5.51	6.11	6.54	6.07	6.49	6.04	6.02	6.10
0721+3928	-5.39	6.13	6.59	6.14	6.54	6.12	6.09	6.17
0735+2057	-5.61	5.95	6.38	5.96	6.34	5.93	5.91	5.99
0736+4118	-5.68	5.95	6.42	5.95	6.37	5.92	5.90	5.98
0739+3112	-5.48	6.29	6.62	6.11	6.56	6.09	6.07	6.14
0741+3146	-5.40	6.31	6.65	6.15	6.59	6.13	6.11	6.19
0744+4649	-5.72	5.92	6.39	5.92	6.34	5.89	5.87	5.95
0744+4408	-5.39	6.12	6.57	6.13	6.53	6.11	6.08	6.16
0744+2701	-5.28	6.14	6.56	6.16	6.51	6.14	6.11	6.20
0744+1640	-5.38	6.55	6.73	6.19	6.67	6.18	6.23	6.23
0758+1013	-5.59	6.01	6.48	6.01	6.43	5.99	5.96	6.04
0800+2242	-5.27	6.38	6.71	6.24	6.66	6.21	6.19	6.27
0806+3055	-5.43	6.06	6.49	6.08	6.44	6.05	6.03	6.11
0806+4058	-5.34	6.14	6.58	6.15	6.53	6.13	6.11	6.19
0807+4930	-5.70	5.93	6.40	5.93	6.35	5.91	5.89	5.96
0816+2330	-5.33	6.10	6.52	6.13	6.47	6.10	6.07	6.16
0818+1247	-5.32	6.15	6.60	6.17	6.55	6.14	6.12	6.20
0823+0546	-5.37	6.26	6.64	6.16	6.59	6.14	6.12	6.20
0830-0319	-5.33	6.19	6.63	6.18	6.58	6.15	6.13	6.21
0832+4109	-5.58	5.98	6.42	5.99	6.37	5.96	5.94	6.02
0838+2322	-5.35	6.38	6.69	6.19	6.64	6.17	6.16	6.23
0842+1406	-5.32	6.14	6.57	6.16	6.53	6.13	6.11	6.19
0842+1536	-5.32	6.30	6.67	6.20	6.61	6.17	6.15	6.23
0843+5614	-5.36	6.14	6.59	6.15	6.54	6.12	6.10	6.18
0851+1543	-5.45	6.08	6.53	6.09	6.48	6.06	6.04	6.12
0852+3402	-5.51	6.11	6.54	6.07	6.49	6.05	6.03	6.10
0901+0752	-5.51	5.98	6.40	6.00	6.35	5.98	5.95	6.04
0902+3625	-5.42	6.10	6.55	6.10	6.50	6.08	6.06	6.14
0902+1004	-5.29	6.16	6.59	6.18	6.55	6.15	6.13	6.21
0906+1141	-5.41	6.08	6.51	6.09	6.46	6.07	6.04	6.13



SDSS J	$\log(q)$	Ca	Mg	Fe	Na	Cr	Ti	Ni
0908+5136	-5.34	6.26	6.65	6.18	6.60	6.16	6.14	6.22
0908+4119	-5.33	6.16	6.61	6.17	6.56	6.15	6.12	6.20
0913+2627	-5.42	6.37	6.67	6.16	6.61	6.14	6.12	6.19
0913+4127	-5.56	6.02	6.47	6.02	6.42	6.00	5.97	6.05
0916+2540	-5.82	5.81	6.25	5.82	6.21	5.80	5.77	5.85
0924+4301	-5.32	6.37	6.70	6.21	6.64	6.19	6.17	6.24
0925+3130	-5.47	6.11	6.56	6.09	6.51	6.07	6.05	6.13
0927+4931	-5.45	6.08	6.53	6.09	6.49	6.07	6.04	6.12
0929+4247	-5.40	6.11	6.55	6.12	6.50	6.09	6.07	6.15
0933+6334	-5.48	6.05	6.49	6.06	6.44	6.03	6.01	6.09
0937+5228	-5.39	6.11	6.55	6.12	6.50	6.09	6.07	6.15
0939+4136	-5.48	6.05	6.50	6.06	6.45	6.04	6.02	6.10
0939+5019	-5.56	6.00	6.45	6.01	6.40	5.99	5.96	6.04
0946+2024	-5.27	6.16	6.59	6.18	6.54	6.15	6.13	6.21
0948+3008	-5.40	6.18	6.60	6.14	6.55	6.11	6.09	6.17
0956+5912	-5.30	6.11	6.51	6.14	6.47	6.11	6.08	6.18
1003-0031	-5.57	6.01	6.46	6.01	6.41	5.99	5.96	6.04
1005+2244	-5.36	6.15	6.61	6.15	6.56	6.13	6.11	6.19
1006+1752	-5.40	6.28	6.64	6.15	6.58	6.13	6.11	6.18
1014+2827	-5.59	5.96	6.39	5.97	6.34	5.95	5.92	6.01
1017+3447	-5.35	6.26	6.65	6.18	6.59	6.16	6.13	6.21
1017+2419	-5.32	6.13	6.56	6.15	6.52	6.13	6.10	6.19
1019+3535	-5.51	6.06	6.52	6.06	6.47	6.04	6.02	6.09
1019+2045	-5.48	6.25	6.60	6.10	6.55	6.08	6.06	6.14
1024+4531	-5.45	6.10	6.56	6.10	6.51	6.08	6.06	6.14
1024+1014	-5.61	5.94	6.37	5.96	6.32	5.93	5.91	5.99
1032+1338	-5.46	6.24	6.60	6.11	6.55	6.09	6.07	6.15
1033+1809	-5.49	6.06	6.51	6.06	6.46	6.04	6.02	6.10
1038-0036	-5.28	6.15	6.57	6.17	6.52	6.14	6.12	6.21
1038+0432	-5.56	5.97	6.39	5.98	6.35	5.96	5.93	6.02
1040+2407	-5.62	5.96	6.41	5.97	6.36	5.95	5.92	6.00
1041+3432	-5.25	6.18	6.61	6.20	6.56	6.17	6.14	6.23
1043+3516	-5.30	6.18	6.63	6.19	6.58	6.17	6.14	6.22
1046+1329	-5.45	6.32	6.64	6.13	6.59	6.11	6.09	6.16
1055+3725	-5.65	5.95	6.41	5.96	6.36	5.93	5.91	5.99
1058+3143	-5.26	6.21	6.66	6.22	6.61	6.20	6.17	6.25
1102+2827	-5.54	5.99	6.42	6.00	6.37	5.98	5.95	6.04
1102+0214	-5.35	6.37	6.69	6.19	6.63	6.17	6.15	6.23
1103+4144	-5.41	6.24	6.62	6.14	6.57	6.12	6.10	6.18
1105+5006	-5.30	6.15	6.58	6.17	6.53	6.14	6.12	6.20
1105+0228	-5.46	6.15	6.58	6.11	6.53	6.08	6.06	6.14
1106+6737	-5.52	6.01	6.44	6.02	6.40	6.00	5.97	6.06
1112+0700	-5.20	6.22	6.65	6.24	6.60	6.21	6.19	6.27
1113+2751	-5.49	6.05	6.50	6.06	6.45	6.04	6.01	6.09
1132+3323	-5.50	6.03	6.48	6.04	6.43	6.02	6.00	6.08
1134+1542	-5.37	6.12	6.57	6.14	6.52	6.11	6.09	6.17
1144+3720	-5.26	6.17	6.60	6.19	6.55	6.17	6.14	6.23
1144+1218	-5.47	6.24	6.60	6.11	6.55	6.09	6.07	6.14
1147+5429	-5.52	6.18	6.57	6.07	6.51	6.05	6.03	6.11
1149+0519	-5.29	6.15	6.58	6.17	6.54	6.15	6.12	6.21
1150+4928	-5.23	6.22	6.66	6.23	6.61	6.21	6.18	6.26
1150+4533	-5.60	5.98	6.44	5.99	6.39	5.96	5.94	6.02
1152+5101	-5.40	6.49	6.71	6.18	6.65	6.16	6.19	6.22
1152+1605	-5.40	6.10	6.54	6.11	6.50	6.09	6.06	6.15
1157+6138	-5.30	6.21	6.65	6.20	6.60	6.17	6.15	6.23
1158+1845	-5.36	6.09	6.52	6.12	6.47	6.09	6.06	6.15
1158+5942	-5.43	6.12	6.57	6.11	6.52	6.09	6.07	6.15
1158+0454	-5.62	6.01	6.47	5.99	6.42	5.97	5.95	6.03
1158+4712	-5.25	6.17	6.60	6.19	6.55	6.17	6.14	6.23
1158+5448	-5.40	6.12	6.58	6.13	6.53	6.10	6.08	6.16
1205+3536	-5.46	6.08	6.54	6.09	6.49	6.07	6.04	6.12
1211+2326	-5.40	6.11	6.56	6.12	6.51	6.10	6.07	6.16
1214-0234	-5.49	6.26	6.61	6.10	6.55	6.08	6.06	6.14
1217+1157	-5.35	6.16	6.61	6.16	6.56	6.14	6.11	6.19
1218+0023	-5.32	6.34	6.68	6.21	6.63	6.18	6.16	6.24
1220+0929	-5.39	6.11	6.55	6.12	6.50	6.10	6.07	6.16
1224+2838	-5.38	6.46	6.71	6.19	6.65	6.17	6.18	6.22

SDSS J	$\log(q)$	Ca	Mg	Fe	Na	Cr	Ti	Ni
1226+2936	-5.44	6.49	6.70	6.16	6.64	6.14	6.18	6.19
1229+0743	-5.53	6.02	6.46	6.03	6.41	6.00	5.98	6.06
1230+3143	-5.31	6.20	6.64	6.19	6.59	6.17	6.15	6.23
1234+5208	-5.37	6.08	6.49	6.10	6.45	6.08	6.05	6.14
1238+2149	-5.51	6.16	6.56	6.07	6.51	6.05	6.03	6.11
1245+0822	-5.50	6.03	6.47	6.04	6.43	6.02	6.00	6.08
1249+6514	-5.21	6.21	6.65	6.23	6.60	6.21	6.18	6.27
1254+3551	-5.31	6.18	6.63	6.19	6.58	6.16	6.14	6.22
1257+3238	-5.56	6.13	6.53	6.04	6.48	6.02	6.00	6.07
1257-0310	-5.45	6.08	6.53	6.09	6.48	6.06	6.04	6.12
1259+3112	-5.35	6.34	6.67	6.19	6.62	6.17	6.15	6.22
1259+4729	-5.41	6.12	6.57	6.12	6.52	6.10	6.08	6.16
1303+4055	-5.39	6.15	6.60	6.14	6.55	6.12	6.10	6.18
1308+0957	-5.23	6.18	6.61	6.21	6.56	6.18	6.15	6.24
1308+0258	-5.41	6.15	6.59	6.13	6.54	6.11	6.08	6.16
1314+3748	-5.53	6.03	6.48	6.03	6.43	6.01	5.99	6.07
1316+1918	-5.38	6.42	6.70	6.18	6.64	6.16	6.16	6.22
1319+3641	-5.22	6.21	6.65	6.23	6.60	6.20	6.18	6.26
1320+0204	-5.33	6.14	6.57	6.15	6.53	6.13	6.10	6.19
1321-0237	-5.60	5.99	6.45	5.99	6.40	5.97	5.95	6.03
1329+1301	-5.33	6.15	6.59	6.16	6.54	6.14	6.11	6.20
1330+3029	-5.51	6.04	6.49	6.05	6.44	6.02	6.00	6.08
1336+3547	-5.38	6.12	6.56	6.13	6.52	6.11	6.08	6.17
1339+2643	-5.35	6.18	6.63	6.17	6.58	6.15	6.12	6.20
1340+2702	-5.43	6.03	6.44	6.06	6.39	6.03	6.00	6.09
1342+1813	-5.52	6.19	6.57	6.07	6.51	6.05	6.03	6.11
1345+1153	-5.58	5.98	6.43	5.99	6.38	5.97	5.95	6.03
1347+1415	-5.35	6.14	6.58	6.15	6.53	6.12	6.10	6.18
1350+1058	-5.38	6.48	6.71	6.19	6.66	6.17	6.19	6.22
1351+2645	-5.59	5.97	6.41	5.98	6.37	5.96	5.93	6.01
1356+2416	-5.39	6.20	6.61	6.15	6.56	6.13	6.10	6.18
1356+0236	-5.27	6.14	6.55	6.17	6.50	6.14	6.11	6.20
1401+3659	-5.31	6.38	6.70	6.22	6.65	6.20	6.18	6.25
1404+3620	-5.41	6.20	6.61	6.13	6.55	6.11	6.09	6.17
1405+2542	-5.37	6.31	6.65	6.17	6.60	6.15	6.13	6.21
1405+1549	-5.30	6.15	6.58	6.17	6.54	6.14	6.12	6.20
1411+3410	-5.64	5.96	6.43	5.97	6.38	5.94	5.92	6.00
1412+2836	-5.52	6.26	6.60	6.09	6.54	6.07	6.05	6.12
1421+1843	-5.43	6.04	6.46	6.06	6.41	6.04	6.01	6.10
1428+4403	-5.31	6.18	6.63	6.18	6.58	6.16	6.14	6.22
1429+3841	-5.31	6.37	6.70	6.21	6.64	6.19	6.17	6.25
1430-0151	-5.64	5.92	6.35	5.94	6.31	5.91	5.89	5.97
1443+5833	-5.28	6.18	6.62	6.19	6.57	6.17	6.14	6.23
1443+3014	-5.38	6.10	6.54	6.12	6.49	6.09	6.07	6.15
1445+0913	-5.46	6.05	6.48	6.06	6.43	6.04	6.01	6.09
1448+1047	-5.34	6.16	6.61	6.16	6.56	6.14	6.12	6.20
1500+2315	-5.41	6.10	6.54	6.11	6.49	6.08	6.06	6.14
1502+3744	-5.36	6.45	6.71	6.20	6.66	6.18	6.18	6.24
1507+4034	-5.31	6.15	6.58	6.16	6.53	6.14	6.11	6.20
1518+0506	-5.47	6.34	6.64	6.13	6.59	6.11	6.09	6.16
1524+4049	-5.47	6.09	6.55	6.09	6.50	6.07	6.05	6.12
1534+1242	-5.58	5.99	6.44	6.00	6.39	5.97	5.95	6.03
1535+1247	-5.54	6.03	6.49	6.03	6.44	6.01	5.99	6.07
1536+4205	-5.52	6.05	6.51	6.05	6.46	6.03	6.00	6.08
1537+3608	-5.42	6.30	6.64	6.15	6.58	6.12	6.11	6.18
1540+5352	-5.38	6.12	6.57	6.13	6.52	6.11	6.08	6.16
1542+4650	-5.56	6.00	6.44	6.01	6.39	5.98	5.96	6.04
1543+2024	-5.50	6.03	6.47	6.04	6.42	6.01	5.99	6.07
1545+5236	-5.43	6.19	6.60	6.13	6.55	6.10	6.08	6.16
1546+3009	-5.39	6.11	6.55	6.12	6.50	6.09	6.07	6.15
1549+2633	-5.28	6.35	6.70	6.23	6.65	6.21	6.19	6.26
1549+1906	-5.41	6.10	6.54	6.11	6.50	6.08	6.06	6.14
1554+1735	-5.36	6.14	6.58	6.15	6.53	6.12	6.10	6.18
1604+1830	-5.28	6.31	6.68	6.22	6.63	6.20	6.18	6.25
1610+4006	-5.39	6.11	6.56	6.12	6.51	6.10	6.08	6.16
1612+3534	-5.34	6.14	6.58	6.15	6.54	6.13	6.11	6.19
1616+3303	-5.46	6.06	6.50	6.07	6.46	6.05	6.02	6.11

SDSS J	$\log(q)$	Ca	Mg	Fe	Na	Cr	Ti	Ni
1624+3310	-5.29	6.17	6.61	6.18	6.57	6.16	6.14	6.22
1626+3303	-5.40	6.13	6.58	6.13	6.53	6.11	6.09	6.17
1627+4646	-5.36	6.15	6.60	6.15	6.55	6.13	6.11	6.19
1636+1619	-5.56	6.32	6.61	6.07	6.56	6.05	6.05	6.10
1641+1856	-5.27	6.52	6.76	6.26	6.71	6.24	6.24	6.29
1649+2238	-5.62	5.99	6.46	5.99	6.41	5.97	5.94	6.02
1651+4249	-5.66	5.93	6.37	5.94	6.33	5.91	5.89	5.97
1706+2541	-5.25	6.27	6.69	6.23	6.64	6.21	6.19	6.27
2109-0039	-5.46	6.09	6.54	6.09	6.49	6.07	6.04	6.12
2110+0512	-5.45	6.20	6.59	6.11	6.54	6.09	6.07	6.15
2123+0016	-5.38	6.46	6.71	6.19	6.65	6.17	6.18	6.22
2157+1206	-5.41	6.13	6.59	6.13	6.54	6.11	6.08	6.16
2225+2338	-5.26	6.20	6.64	6.21	6.59	6.19	6.16	6.25
2230+1905	-5.61	5.99	6.45	5.99	6.40	5.96	5.94	6.02
2231+0906	-5.31	6.39	6.71	6.22	6.65	6.20	6.18	6.25
2235-0056	-5.41	6.11	6.56	6.12	6.51	6.09	6.07	6.15
2238+0213	-5.29	6.17	6.61	6.18	6.56	6.16	6.13	6.22
2238-0113	-5.28	6.19	6.64	6.20	6.59	6.18	6.15	6.23
2254+3031	-5.58	5.99	6.44	6.00	6.39	5.97	5.95	6.03
2304+2415	-5.48	6.30	6.63	6.11	6.57	6.09	6.07	6.15
2319+3018	-5.27	6.18	6.62	6.20	6.57	6.17	6.15	6.23
2325+0448	-5.41	6.15	6.59	6.13	6.54	6.11	6.08	6.16
2328+0830	-5.50	6.07	6.52	6.06	6.47	6.04	6.02	6.10
2330+2805	-5.32	6.17	6.62	6.18	6.57	6.15	6.13	6.21
2330+2956	-5.33	6.13	6.57	6.15	6.52	6.12	6.10	6.18
2333+1058	-5.42	6.11	6.57	6.12	6.52	6.09	6.07	6.15
2340+0124	-5.47	6.07	6.52	6.07	6.47	6.05	6.03	6.11
2340+0817	-5.51	6.11	6.54	6.07	6.49	6.04	6.02	6.10
2343-0010	-5.41	6.21	6.61	6.14	6.56	6.12	6.09	6.17
2352+1922	-5.50	6.04	6.49	6.05	6.44	6.02	6.00	6.08
2352+3344	-5.29	6.16	6.59	6.18	6.55	6.15	6.13	6.21
2357+2348	-5.41	6.15	6.59	6.13	6.54	6.11	6.08	6.16

Table A4: Distances  $d$ , proper-motions  $\mu$ , transverse motions  $v_{\perp}$ , and white dwarf cooling ages for our DZ sample.

SDSS J	$d$ [pc]	$\mu$ [mas yr <sup>-1</sup> ]	$v_{\perp}$ [km s <sup>-1</sup> ]	Age [Gyr]	SDSS J	$d$ [pc]	$\mu$ [mas yr <sup>-1</sup> ]	$v_{\perp}$ [km s <sup>-1</sup> ]	Age [Gyr]
0002+3209	210 ± 28	38.4 ± 5.3	38.5 ± 7.6	2.6 <sup>+0.8</sup> <sub>-0.6</sub>	0004+0819	336 ± 46	-	-	3.7 <sup>+1.6</sup> <sub>-1.2</sub>
0006+0520	216 ± 28	-	-	2.1 <sup>+0.6</sup> <sub>-0.5</sub>	0010-0430	221 ± 30	66.7 ± 4.2	70 ± 11	2.0 <sup>+0.5</sup> <sub>-0.4</sub>
0013+1109	277 ± 36	-	-	3.7 <sup>+1.4</sup> <sub>-1.1</sub>	0019+2209	155 ± 20	45.4 ± 3.3	33.4 ± 5.0	3.3 <sup>+1.0</sup> <sub>-0.9</sub>
0037-0525	125 ± 16	12.5 ± 3.5	7.4 ± 2.3	4.2 <sup>+1.0</sup> <sub>-1.1</sub>	0044+0418	79 ± 10	63.1 ± 6.6	23.8 ± 4.0	3.2 <sup>+0.9</sup> <sub>-0.8</sub>
0046+2717	272 ± 37	28.7 ± 4.6	37.2 ± 7.8	1.5 <sup>+0.4</sup> <sub>-0.3</sub>	0047+1628	246 ± 32	-	-	2.3 <sup>+0.7</sup> <sub>-0.5</sub>
0052+1846	250 ± 33	-	-	4.2 <sup>+1.4</sup> <sub>-1.3</sub>	0053+3115	276 ± 37	-	-	2.9 <sup>+1.1</sup> <sub>-0.8</sub>
0056+2453	214 ± 28	-	-	4.9 <sup>+1.2</sup> <sub>-1.5</sub>	0107+2650	101 ± 13	262.5 ± 3.1	126 ± 17	2.9 <sup>+0.8</sup> <sub>-0.8</sub>
0108-0537	173 ± 23	26.7 ± 3.4	22.1 ± 4.0	3.2 <sup>+0.9</sup> <sub>-0.9</sub>	0114+3505	243 ± 32	-	-	2.6 <sup>+0.8</sup> <sub>-0.7</sub>
0116+2050	68.3 ± 8.9	118.4 ± 2.8	38.5 ± 5.1	2.9 <sup>+0.8</sup> <sub>-0.5</sub>	0117+0021	132 ± 18	501.8 ± 7.4	316 ± 42	2.1 <sup>+0.5</sup> <sub>-0.5</sub>
0126+2534	140 ± 18	122.4 ± 4.7	81 ± 11	5.5 <sup>+0.6</sup> <sub>-1.3</sub>	0135+1302	94 ± 12	105.5 ± 3.6	47.4 ± 6.2	3.7 <sup>+1.0</sup> <sub>-1.0</sub>
0143+0113	137 ± 18	74.4 ± 3.8	48.6 ± 6.9	2.2 <sup>+0.6</sup> <sub>-0.5</sub>	0144+1920	225 ± 30	31.9 ± 4.5	34.2 ± 6.7	2.5 <sup>+0.8</sup> <sub>-0.6</sub>
0144+0305	356 ± 48	-	-	2.0 <sup>+0.7</sup> <sub>-0.5</sub>	0148-0112	266 ± 36	13.4 ± 4.8	17.0 ± 6.5	2.1 <sup>+0.6</sup> <sub>-0.5</sub>
0150+1354	167 ± 22	96.8 ± 3.8	77 ± 11	2.7 <sup>+0.8</sup> <sub>-0.7</sub>	0157+0033	120 ± 16	31.5 ± 6.7	18.0 ± 4.5	3.1 <sup>+0.9</sup> <sub>-0.8</sub>
0158-0942	171 ± 22	86.3 ± 5.0	70 ± 10	3.4 <sup>+1.0</sup> <sub>-0.9</sub>	0200+1646	186 ± 24	52.0 ± 4.6	46.0 ± 7.3	3.7 <sup>+1.1</sup> <sub>-1.0</sub>
0201+2015	174 ± 23	-	-	2.9 <sup>+0.9</sup> <sub>-0.8</sub>	0208-0542	227 ± 30	-	-	3.8 <sup>+1.5</sup> <sub>-1.2</sub>
0234-0510	321 ± 44	-	-	1.9 <sup>+0.6</sup> <sub>-0.5</sub>	0252-0401	215 ± 29	66.7 ± 4.2	68 ± 10	2.0 <sup>+0.5</sup> <sub>-0.4</sub>
0252+0054	206 ± 28	57.4 ± 4.7	56.5 ± 8.9	1.6 <sup>+0.3</sup> <sub>-0.3</sub>	0447+1124	188 ± 25	32.7 ± 5.0	29.3 ± 5.9	2.4 <sup>+0.7</sup> <sub>-0.6</sub>
0512-0505	55.5 ± 6.9	85.2 ± 3.1	22.5 ± 2.9	4.5 <sup>+0.8</sup> <sub>-1.1</sub>	0721+3928	199 ± 26	-	-	2.8 <sup>+0.8</sup> <sub>-0.7</sub>
0735+2057	176 ± 23	38.2 ± 5.5	32.1 ± 6.2	3.1 <sup>+0.9</sup> <sub>-1.0</sub>	0736+4118	93 ± 12	141.7 ± 3.1	62.5 ± 7.9	6.1 <sup>+0.5</sup> <sub>-1.1</sub>
0739+3112	169 ± 21	-	-	6.1 <sup>+1.0</sup> <sub>-1.6</sub>	0741+3146	153 ± 19	-	-	4.4 <sup>+1.0</sup> <sub>-1.1</sub>
0744+4649	59.7 ± 7.3	69.4 ± 3.3	19.7 ± 2.6	6.4 <sup>+0.4</sup> <sub>-1.1</sub>	0744+4408	289 ± 39	72.1 ± 4.9	99 ± 15	2.6 <sup>+0.9</sup> <sub>-0.7</sub>
0744+2701	272 ± 37	23.9 ± 4.0	31.0 ± 6.8	1.4 <sup>+0.3</sup> <sub>-0.3</sub>	0744+1640	118 ± 15	-	-	6.6 <sup>+0.5</sup> <sub>-1.2</sub>
0758+1013	197 ± 26	-	-	4.7 <sup>+1.2</sup> <sub>-1.4</sub>	0800+2242	220 ± 30	-	-	2.8 <sup>+1.0</sup> <sub>-0.8</sub>
0806+3055	266 ± 36	-	-	2.0 <sup>+0.5</sup> <sub>-0.5</sub>	0806+4058	114 ± 16	111 ± 11	60 ± 10	2.1 <sup>+0.5</sup> <sub>-0.5</sub>
0807+4930	156 ± 20	-	-	6.1 <sup>+0.8</sup> <sub>-1.4</sub>	0816+2330	369 ± 51	-	-	1.4 <sup>+0.4</sup> <sub>-0.3</sub>
0818+1247	294 ± 41	-	-	2.1 <sup>+0.7</sup> <sub>-0.5</sub>	0823+0546	52.2 ± 6.7	251.9 ± 2.7	62.6 ± 8.1	3.2 <sup>+0.9</sup> <sub>-0.9</sub>
0830-0319	140 ± 19	51.9 ± 3.4	34.6 ± 5.2	2.6 <sup>+0.7</sup> <sub>-0.7</sub>	0832+4109	234 ± 31	55.0 ± 5.4	61 ± 10	3.1 <sup>+1.0</sup> <sub>-0.9</sub>
0838+2322	84 ± 10	41.9 ± 3.3	16.8 ± 2.5	4.1 <sup>+0.9</sup> <sub>-1.0</sub>	0842+1406	93 ± 12	79.3 ± 4.8	35.3 ± 5.2	1.8 <sup>+0.4</sup> <sub>-0.4</sub>
0842+1536	209 ± 28	36.3 ± 3.6	36.0 ± 6.0	2.9 <sup>+1.0</sup> <sub>-0.8</sub>	0843+5614	218 ± 30	20.9 ± 4.1	21.7 ± 5.2	2.3 <sup>+0.7</sup> <sub>-0.5</sub>
0851+1543	99 ± 13	76.4 ± 3.0	36.0 ± 5.0	2.8 <sup>+0.7</sup> <sub>-0.7</sub>	0852+3402	176 ± 22	-	-	4.4 <sup>+1.1</sup> <sub>-1.2</sub>
0901+0752	209 ± 28	44.7 ± 3.9	44.4 ± 7.0	1.9 <sup>+0.4</sup> <sub>-0.4</sub>	0902+3625	222 ± 29	-	-	2.7 <sup>+0.9</sup> <sub>-0.7</sub>
0902+1004	290 ± 40	-	-	1.8 <sup>+0.5</sup> <sub>-0.4</sub>	0906+1141	306 ± 41	-	-	2.0 <sup>+0.6</sup> <sub>-0.5</sub>
0908+5136	119 ± 15	43.8 ± 3.7	24.8 ± 3.9	3.0 <sup>+0.8</sup> <sub>-0.8</sub>	0908+4119	303 ± 42	-	-	2.2 <sup>+0.8</sup> <sub>-0.3</sub>
0913+2627	111 ± 14	72.1 ± 4.8	38.1 ± 5.4	5.8 <sup>+0.7</sup> <sub>-1.3</sub>	0913+4127	212 ± 28	-	-	3.8 <sup>+1.1</sup> <sub>-1.1</sub>
0916+2540	43.4 ± 5.4	237.8 ± 2.8	49.1 ± 6.2	5.3 <sup>+0.6</sup> <sub>-1.2</sub>	0924+4301	236 ± 31	52.0 ± 4.8	58.3 ± 9.3	3.4 <sup>+1.1</sup> <sub>-1.0</sub>
0925+3130	81 ± 10	137.0 ± 3.3	53.1 ± 6.9	3.7 <sup>+1.0</sup> <sub>-0.9</sub>	0927+4931	248 ± 33	65.6 ± 5.5	78 ± 12	2.9 <sup>+1.0</sup> <sub>-0.8</sub>
0929+4247	185 ± 25	15.0 ± 3.7	13.2 ± 3.7	2.4 <sup>+0.7</sup> <sub>-0.6</sub>	0933+6334	269 ± 36	-	-	2.8 <sup>+1.2</sup> <sub>-0.8</sub>
0937+5228	132 ± 18	69.0 ± 3.6	43.2 ± 6.2	2.3 <sup>+0.6</sup> <sub>-0.5</sub>	0939+4136	202 ± 27	43.7 ± 5.4	42.0 ± 7.7	2.7 <sup>+0.8</sup> <sub>-0.7</sub>
0939+5019	134 ± 17	81.6 ± 5.5	52.1 ± 7.6	3.3 <sup>+1.0</sup> <sub>-0.9</sub>	0946+2024	311 ± 43	-	-	1.6 <sup>+0.5</sup> <sub>-0.4</sub>
0948+3008	164 ± 21	70.0 ± 3.6	54.5 ± 7.4	3.3 <sup>+0.9</sup> <sub>-0.9</sub>	0956+5912	139 ± 19	125.8 ± 3.0	83 ± 12	1.0 <sup>+0.1</sup> <sub>-0.2</sub>
1003-0031	161 ± 20	40.7 ± 5.8	31.2 ± 5.9	3.9 <sup>+1.0</sup> <sub>-1.0</sub>	1005+2244	301 ± 41	50 ± 14	72 ± 22	2.6 <sup>+1.0</sup> <sub>-0.7</sub>
1006+1752	159 ± 20	-	-	4.0 <sup>+1.1</sup> <sub>-1.1</sub>	1014+2827	257 ± 35	-	-	2.8 <sup>+1.1</sup> <sub>-0.8</sub>
1017+3447	186 ± 25	115.9 ± 3.6	103 ± 14	3.0 <sup>+0.9</sup> <sub>-0.8</sub>	1017+2419	199 ± 27	77.4 ± 3.6	73 ± 11	1.8 <sup>+0.4</sup> <sub>-0.4</sub>
1019+3535	239 ± 31	-	-	3.7 <sup>+1.3</sup> <sub>-1.1</sub>	1019+2045	169 ± 22	84.5 ± 5.4	68.0 ± 9.7	5.5 <sup>+0.9</sup> <sub>-1.5</sub>
1024+4531	166 ± 21	15.7 ± 5.4	12.3 ± 4.5	3.3 <sup>+1.0</sup> <sub>-0.9</sub>	1024+1014	194 ± 26	51.3 ± 4.8	47.4 ± 7.6	2.7 <sup>+1.0</sup> <sub>-0.7</sub>
1032+1338	198 ± 25	-	-	4.8 <sup>+1.1</sup> <sub>-1.4</sub>	1033+1809	131 ± 17	225 ± 99	140 ± 66	3.1 <sup>+1.1</sup> <sub>-0.9</sub>
1038-0036	58.9 ± 7.8	99.1 ± 2.9	27.8 ± 3.8	1.5 <sup>+0.2</sup> <sub>-0.3</sub>	1038+0432	228 ± 30	-	-	2.4 <sup>+0.7</sup> <sub>-0.6</sub>
1040+2407	91 ± 12	166.6 ± 3.4	72.5 ± 9.4	3.9 <sup>+0.9</sup> <sub>-1.0</sub>	1041+3432	299 ± 41	-	-	1.6 <sup>+0.4</sup> <sub>-0.3</sub>
1043+3516	105 ± 14	148.9 ± 3.2	75 ± 10	2.2 <sup>+0.8</sup> <sub>-0.5</sub>	1046+1329	126 ± 16	-	-	5.9 <sup>+0.3</sup> <sub>-1.4</sub>
1055+3725	134 ± 17	105.7 ± 5.1	67.5 ± 9.4	4.4 <sup>+1.0</sup> <sub>-1.1</sub>	1058+3143	122 ± 16	38.8 ± 4.5	22.5 ± 4.0	2.1 <sup>+0.5</sup> <sub>-0.5</sub>
1102+2827	288 ± 39	-	-	2.6 <sup>+1.1</sup> <sub>-0.7</sub>	1102+0214	101 ± 13	96.5 ± 3.6	46.3 ± 6.2	3.9 <sup>+0.9</sup> <sub>-1.0</sub>
1103+4144	117 ± 15	53.0 ± 3.8	29.6 ± 4.3	3.6 <sup>+0.9</sup> <sub>-0.9</sub>	1105+5006	245 ± 33	35.8 ± 4.0	41.8 ± 7.4	1.7 <sup>+0.4</sup> <sub>-0.4</sub>
1105+0228	166 ± 21	-	-	3.8 <sup>+1.3</sup> <sub>-1.1</sub>	1106+6737	161 ± 22	62.1 ± 3.9	47.8 ± 7.1	2.6 <sup>+0.8</sup> <sub>-0.7</sub>
1112+0700	163 ± 22	67.7 ± 3.9	52.4 ± 7.7	1.5 <sup>+0.3</sup> <sub>-0.3</sub>	1113+2751	213 ± 28	22.4 ± 4.6	22.7 ± 5.5	2.9 <sup>+0.9</sup> <sub>-0.8</sub>
1132+3323	257 ± 35	-	-	2.8 <sup>+1.0</sup> <sub>-0.8</sub>	1134+1542	309 ± 41	-	-	2.2 <sup>+0.8</sup> <sub>-0.5</sub>
1144+3720	252 ± 34	16.5 ± 4.7	19.8 ± 6.2	1.6 <sup>+0.4</sup> <sub>-0.3</sub>	1144+1218	50.2 ± 6.2	617.1 ± 5.8	147 ± 18	5.0 <sup>+0.7</sup> <sub>-1.2</sub>
1147+5429	212 ± 28	96.5 ± 5.2	97 ± 14	5.4 <sup>+1.2</sup> <sub>-1.7</sub>	1149+0519	174 ± 23	40.1 ± 3.5	33.3 ± 5.3	1.7 <sup>+0.4</sup> <sub>-0.4</sub>
1150+4928	202 ± 27	62.2 ± 3.9	59.7 ± 8.8	1.8 <sup>+0.4</sup> <sub>-0.4</sub>	1150+4533	253 ± 33	-	-	4.0 <sup>+1.5</sup> <sub>-1.2</sub>
1152+5101	165 ± 21	-	-	6.4 <sup>+0.7</sup> <sub>-1.3</sub>	1152+1605	188 ± 26	48.7 ± 3.9	43.5 ± 6.9	2.4 <sup>+0.7</sup> <sub>-0.6</sub>



SDSS J	$d$ [pc]	$\mu$ [mas yr <sup>-1</sup> ]	$v_{\perp}$ [km s <sup>-1</sup> ]	Age [Gyr]	SDSS J	$d$ [pc]	$\mu$ [mas yr <sup>-1</sup> ]	$v_{\perp}$ [km s <sup>-1</sup> ]	Age [Gyr]
1157+6138	335 ± 46	-	-	2.4 <sup>+1.0</sup> <sub>-0.6</sub>	1158+1845	212 ± 28	68.5 ± 3.4	69.1 ± 9.7	1.8 <sup>+0.4</sup> <sub>-0.4</sub>
1158+5942	186 ± 24	16.3 ± 5.2	14.5 ± 5.0	3.3 <sup>+1.0</sup> <sub>-0.9</sub>	1158+0454	146 ± 19	26.1 ± 5.0	18.2 ± 4.2	5.6 <sup>+0.8</sup> <sub>-1.3</sub>
1158+4712	319 ± 44	60.1 ± 5.5	91 ± 15	1.5 <sup>+0.3</sup> <sub>-0.3</sub>	1158+5448	254 ± 35	-	-	2.8 <sup>+1.1</sup> <sub>-0.8</sub>
1205+3536	176 ± 23	-	-	3.1 <sup>+0.9</sup> <sub>-0.8</sub>	1211+2326	238 ± 32	106.6 ± 4.8	121 ± 17	2.5 <sup>+0.8</sup> <sub>-0.6</sub>
1214-0234	43.2 ± 5.3	550 ± 19	113 ± 14	5.8 <sup>+0.5</sup> <sub>-1.2</sub>	1217+1157	188 ± 25	36.4 ± 5.2	32.6 ± 6.3	2.5 <sup>+0.7</sup> <sub>-0.6</sub>
1218+0023	119 ± 16	59.8 ± 4.0	33.9 ± 5.0	3.1 <sup>+0.8</sup> <sub>-0.8</sub>	1220+0929	263 ± 35	18.9 ± 4.9	23.6 ± 7.0	2.3 <sup>+0.7</sup> <sub>-0.5</sub>
1224+2838	85 ± 11	99.9 ± 3.5	40.5 ± 5.2	5.8 <sup>+0.6</sup> <sub>-1.2</sub>	1226+2936	85 ± 11	205.2 ± 5.1	83 ± 11	7.1 <sup>+0.5</sup> <sub>-1.1</sub>
1229+0743	183 ± 24	18.9 ± 4.9	16.5 ± 4.8	3.0 <sup>+0.8</sup> <sub>-0.8</sub>	1230+3143	198 ± 27	39.8 ± 4.7	37.5 ± 6.8	2.4 <sup>+0.7</sup> <sub>-0.6</sub>
1234+5208	112 ± 15	94.1 ± 3.2	50.3 ± 7.1	1.5 <sup>+0.3</sup> <sub>-0.3</sub>	1238+2149	157 ± 20	74.9 ± 4.9	55.9 ± 7.9	5.0 <sup>+0.9</sup> <sub>-1.3</sub>
1245+0822	236 ± 31	-	-	2.7 <sup>+0.8</sup> <sub>-0.7</sub>	1249+6514	275 ± 37	81.0 ± 7.8	106 ± 18	1.6 <sup>+0.3</sup> <sub>-0.3</sub>
1254+3551	234 ± 32	107.6 ± 7.4	120 ± 18	2.3 <sup>+0.7</sup> <sub>-0.5</sub>	1257+3238	198 ± 26	51.9 ± 4.8	49.0 ± 7.9	5.7 <sup>+1.1</sup> <sub>-1.7</sub>
1257-0310	206 ± 28	-	-	2.8 <sup>+0.9</sup> <sub>-0.7</sub>	1259+3112	118 ± 15	75.6 ± 3.8	42.5 ± 5.9	3.7 <sup>+1.2</sup> <sub>-1.0</sub>
1259+4729	228 ± 31	66.7 ± 5.5	72 ± 12	2.8 <sup>+1.0</sup> <sub>-0.8</sub>	1303+4055	139 ± 18	27.7 ± 3.4	18.3 ± 3.4	2.9 <sup>+0.8</sup> <sub>-0.9</sub>
1308+0957	386 ± 54	-	-	1.4 <sup>+0.4</sup> <sub>-0.3</sub>	1308+0258	208 ± 27	-	-	3.2 <sup>+1.0</sup> <sub>-0.9</sub>
1314+3748	205 ± 28	54.3 ± 4.9	52.9 ± 8.6	3.4 <sup>+1.3</sup> <sub>-1.0</sub>	1316+1918	166 ± 21	48.3 ± 3.5	38.0 ± 5.5	5.3 <sup>+0.8</sup> <sub>-1.4</sub>
1319+3641	236 ± 32	22.4 ± 4.8	25.1 ± 6.4	1.7 <sup>+0.4</sup> <sub>-0.4</sub>	1320+0204	317 ± 44	18.0 ± 6.0	27.1 ± 9.8	1.9 <sup>+0.6</sup> <sub>-0.5</sub>
1321-0237	156 ± 20	-	-	4.3 <sup>+1.2</sup> <sub>-1.3</sub>	1329+1301	186 ± 25	167.0 ± 7.6	148 ± 21	2.1 <sup>+0.6</sup> <sub>-0.5</sub>
1330+3029	26.1 ± 3.4	487.0 ± 2.4	60.6 ± 7.8	3.1 <sup>+0.8</sup> <sub>-0.8</sub>	1336+3547	65.6 ± 8.9	126.5 ± 2.6	39.5 ± 5.4	2.3 <sup>+0.6</sup> <sub>-0.6</sub>
1339+2643	98 ± 13	64.3 ± 3.0	30.1 ± 4.3	2.8 <sup>+0.7</sup> <sub>-0.7</sub>	1340+2702	373 ± 51	7.8 ± 3.8	13.8 ± 7.1	1.4 <sup>+0.3</sup> <sub>-0.3</sub>
1342+1813	168 ± 21	74.3 ± 5.1	59.5 ± 8.6	5.7 <sup>+0.9</sup> <sub>-1.4</sub>	1345+1153	131 ± 17	139.9 ± 3.8	87 ± 11	3.2 <sup>+1.0</sup> <sub>-0.9</sub>
1347+1415	158 ± 21	14.0 ± 3.5	10.5 ± 3.0	2.2 <sup>+0.6</sup> <sub>-0.5</sub>	1350+1058	139 ± 17	69.7 ± 5.0	46.1 ± 6.5	6.0 <sup>+0.7</sup> <sub>-1.2</sub>
1351+2645	161 ± 20	55.4 ± 4.4	42.5 ± 6.4	3.3 <sup>+1.0</sup> <sub>-0.9</sub>	1356+2416	90 ± 12	112.2 ± 3.2	48.3 ± 6.3	3.2 <sup>+0.9</sup> <sub>-0.9</sub>
1356+0236	214 ± 30	24.9 ± 5.2	25.4 ± 6.5	1.2 <sup>+0.2</sup> <sub>-0.2</sub>	1401+3659	80 ± 10	59.8 ± 2.9	22.7 ± 3.1	3.3 <sup>+0.9</sup> <sub>-0.9</sub>
1404+3620	77.0 ± 9.8	176.2 ± 3.0	64.6 ± 8.3	3.5 <sup>+0.9</sup> <sub>-0.9</sub>	1405+2542	214 ± 28	21.1 ± 4.9	21.6 ± 5.8	3.5 <sup>+1.1</sup> <sub>-1.0</sub>
1405+1549	124 ± 17	112.8 ± 3.1	66.4 ± 9.1	1.8 <sup>+0.4</sup> <sub>-0.4</sub>	1411+3410	149 ± 19	70.3 ± 4.8	49.9 ± 7.1	4.8 <sup>+1.0</sup> <sub>-1.3</sub>
1412+2836	148 ± 19	103.0 ± 3.6	72.8 ± 9.5	6.5 <sup>+0.5</sup> <sub>-1.1</sub>	1421+1843	245 ± 34	36.4 ± 3.8	42.5 ± 7.3	1.7 <sup>+0.4</sup> <sub>-0.4</sub>
1428+4403	44.1 ± 6.0	278.8 ± 2.5	58.5 ± 8.0	2.3 <sup>+0.6</sup> <sub>-0.6</sub>	1429+3841	192 ± 25	34.7 ± 3.7	31.7 ± 5.3	3.2 <sup>+1.1</sup> <sub>-0.9</sub>
1430-0151	115 ± 15	60.4 ± 3.7	33.1 ± 4.8	3.0 <sup>+0.9</sup> <sub>-0.8</sub>	1443+5833	380 ± 53	209.9 ± 4.2	380 ± 53	1.9 <sup>+0.6</sup> <sub>-0.4</sub>
1443+3014	370 ± 51	-	-	2.1 <sup>+0.7</sup> <sub>-0.5</sub>	1445+0913	317 ± 43	-	-	2.3 <sup>+0.8</sup> <sub>-0.6</sub>
1448+1047	100 ± 13	63.9 ± 3.2	30.6 ± 4.3	2.4 <sup>+0.6</sup> <sub>-0.6</sub>	1500+2315	363 ± 52	-	-	2.4 <sup>+1.1</sup> <sub>-0.7</sub>
1502+3744	102 ± 13	104.0 ± 3.8	50.3 ± 6.6	5.1 <sup>+0.7</sup> <sub>-1.2</sub>	1507+4034	338 ± 46	-	-	1.8 <sup>+0.6</sup> <sub>-0.4</sub>
1518+0506	67.4 ± 8.4	39.7 ± 3.8	12.7 ± 2.0	6.4 <sup>+0.5</sup> <sub>-1.1</sub>	1524+4049	143 ± 19	26.2 ± 3.9	17.8 ± 3.6	3.5 <sup>+1.0</sup> <sub>-0.9</sub>
1534+1242	276 ± 37	-	-	3.6 <sup>+1.4</sup> <sub>-1.1</sub>	1535+1247	19.4 ± 2.4	247.8 ± 2.3	22.9 ± 2.9	3.8 <sup>+0.9</sup> <sub>-0.9</sub>
1536+4205	181 ± 23	41.4 ± 5.6	35.7 ± 6.7	3.7 <sup>+1.0</sup> <sub>-1.0</sub>	1537+3608	193 ± 24	-	-	4.5 <sup>+1.3</sup> <sub>-1.3</sub>
1540+5352	294 ± 40	-	-	2.4 <sup>+1.0</sup> <sub>-0.6</sub>	1542+4650	209 ± 27	50.5 ± 5.5	50.3 ± 8.5	3.2 <sup>+1.0</sup> <sub>-0.9</sub>
1543+2024	306 ± 42	-	-	2.7 <sup>+1.1</sup> <sub>-0.8</sub>	1545+5236	134 ± 18	47.2 ± 5.9	30.2 ± 5.4	3.6 <sup>+1.0</sup> <sub>-1.0</sub>
1546+3009	157 ± 21	18.4 ± 3.4	13.7 ± 3.1	2.3 <sup>+0.6</sup> <sub>-0.6</sub>	1549+2633	222 ± 30	51.3 ± 3.6	54.1 ± 8.2	2.8 <sup>+0.8</sup> <sub>-0.7</sub>
1549+1906	292 ± 39	42.2 ± 4.9	59 ± 10	2.5 <sup>+0.9</sup> <sub>-0.6</sub>	1554+1735	58.6 ± 7.7	147.5 ± 2.5	41.2 ± 5.4	2.3 <sup>+0.6</sup> <sub>-0.5</sub>
1604+1830	142 ± 19	55.1 ± 3.1	37.4 ± 5.4	2.6 <sup>+0.7</sup> <sub>-0.9</sub>	1610+4006	274 ± 38	-	-	2.3 <sup>+0.8</sup> <sub>-0.6</sub>
1612+3534	362 ± 52	39.6 ± 5.5	68 ± 14	2.2 <sup>+0.9</sup> <sub>-0.6</sub>	1616+3303	117 ± 15	52.0 ± 3.5	29.1 ± 4.3	2.6 <sup>+0.7</sup> <sub>-0.7</sub>
1624+3310	319 ± 44	-	-	2.0 <sup>+0.7</sup> <sub>-0.5</sub>	1626+3303	256 ± 34	17.9 ± 5.2	21.8 ± 7.0	2.8 <sup>+1.0</sup> <sub>-0.8</sub>
1627+4646	193 ± 26	19.0 ± 4.0	17.5 ± 4.4	2.6 <sup>+0.8</sup> <sub>-0.7</sub>	1636+1619	66.9 ± 8.0	87.0 ± 4.1	27.7 ± 3.6	7.7 <sup>+0.3</sup> <sub>-0.9</sub>
1641+1856	137 ± 17	53.9 ± 3.4	35.1 ± 5.0	3.7 <sup>+1.0</sup> <sub>-1.0</sub>	1649+2238	147 ± 18	31.8 ± 4.0	22.2 ± 4.0	5.4 <sup>+0.7</sup> <sub>-1.4</sub>
1651+4249	106 ± 14	80 ± 16	41 ± 10	4.0 <sup>+1.2</sup> <sub>-1.1</sub>	1706+2541	281 ± 38	13.7 ± 5.2	18.4 ± 7.6	2.3 <sup>+0.8</sup> <sub>-0.5</sub>
2109-0039	149 ± 19	42.8 ± 5.0	30.5 ± 5.4	3.2 <sup>+1.1</sup> <sub>-0.9</sub>	2110+0512	252 ± 33	-	-	4.1 <sup>+1.3</sup> <sub>-1.2</sub>
2123+0016	116 ± 14	109.5 ± 4.8	60.4 ± 8.0	5.7 <sup>+0.7</sup> <sub>-1.3</sub>	2157+1206	127 ± 17	38.9 ± 3.6	23.5 ± 3.8	3.1 <sup>+0.8</sup> <sub>-0.8</sub>
2225+2338	147 ± 20	43.2 ± 7.0	30.2 ± 6.3	2.0 <sup>+0.4</sup> <sub>-0.4</sub>	2230+1905	168 ± 22	17.3 ± 3.1	13.8 ± 3.1	4.4 <sup>+1.3</sup> <sub>-1.3</sub>
2231+0906	93 ± 12	218.4 ± 3.0	97 ± 13	3.5 <sup>+0.9</sup> <sub>-0.9</sub>	2235-0056	200 ± 27	-	-	2.7 <sup>+0.8</sup> <sub>-0.7</sub>
2238+0213	267 ± 36	-	-	1.9 <sup>+0.6</sup> <sub>-0.3</sub>	2238-0113	258 ± 35	-	-	2.1 <sup>+0.7</sup> <sub>-0.5</sub>
2254+3031	120 ± 15	49.4 ± 3.1	28.3 ± 4.0	3.5 <sup>+0.9</sup> <sub>-0.9</sub>	2304+2415	79.1 ± 9.8	115.2 ± 3.6	43.4 ± 5.5	6.3 <sup>+1.1</sup> <sub>-1.1</sub>
2319+3018	306 ± 41	-	-	1.9 <sup>+0.4</sup> <sub>-0.4</sub>	2325+0448	134 ± 17	40.3 ± 3.2	25.8 ± 3.9	3.2 <sup>+0.9</sup> <sub>-0.9</sub>
2328+0830	251 ± 34	-	-	3.8 <sup>+1.4</sup> <sub>-1.2</sub>	2330+2805	249 ± 33	44.9 ± 4.5	53.3 ± 8.9	2.2 <sup>+0.7</sup> <sub>-0.5</sub>
2330+2956	180 ± 24	36.2 ± 3.6	31.0 ± 5.1	2.0 <sup>+0.4</sup> <sub>-0.4</sub>	2333+1058	302 ± 40	-	-	2.9 <sup>+1.1</sup> <sub>-0.8</sub>
2340+0124	114 ± 15	115.1 ± 3.0	62.7 ± 8.4	2.9 <sup>+0.8</sup> <sub>-0.8</sub>	2340+0817	132 ± 16	138.1 ± 3.6	86 ± 11	4.5 <sup>+1.0</sup> <sub>-1.1</sub>
2343-0010	163 ± 22	59.1 ± 5.2	45.9 ± 7.2	3.5 <sup>+1.0</sup> <sub>-1.0</sub>	2352+1922	272 ± 37	-	-	3.0 <sup>+1.1</sup> <sub>-0.9</sub>
2352+3344	312 ± 42	20.6 ± 3.8	30.6 ± 7.0	1.8 <sup>+0.4</sup> <sub>-0.4</sub>	2357+2348	251 ± 33	-	-	3.2 <sup>+1.1</sup> <sub>-0.9</sub>

## APPENDIX B: ADDITIONAL FIGURES

This paper has been typeset from a  $\text{\TeX}/\text{\LaTeX}$  file prepared by the author.

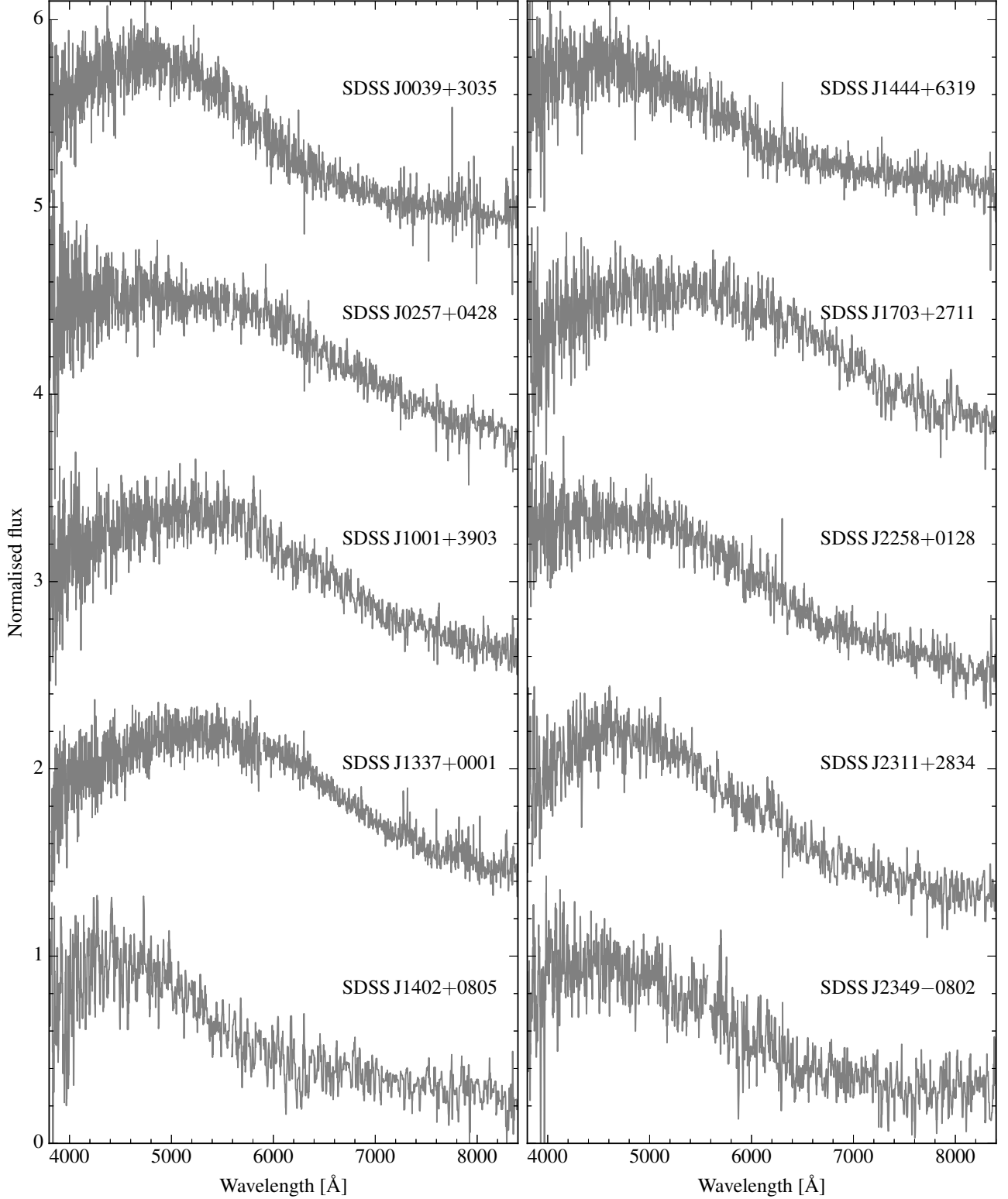


**Figure B1.** Ultracool white dwarf spectra. Each spectrum is normalised to 1, and offset by 1.2 from one another. Smoothing is applied according to the spectral signal-to-noise. Full coordinates and plate-MJD-fiber identifiers are provided in Table 1.

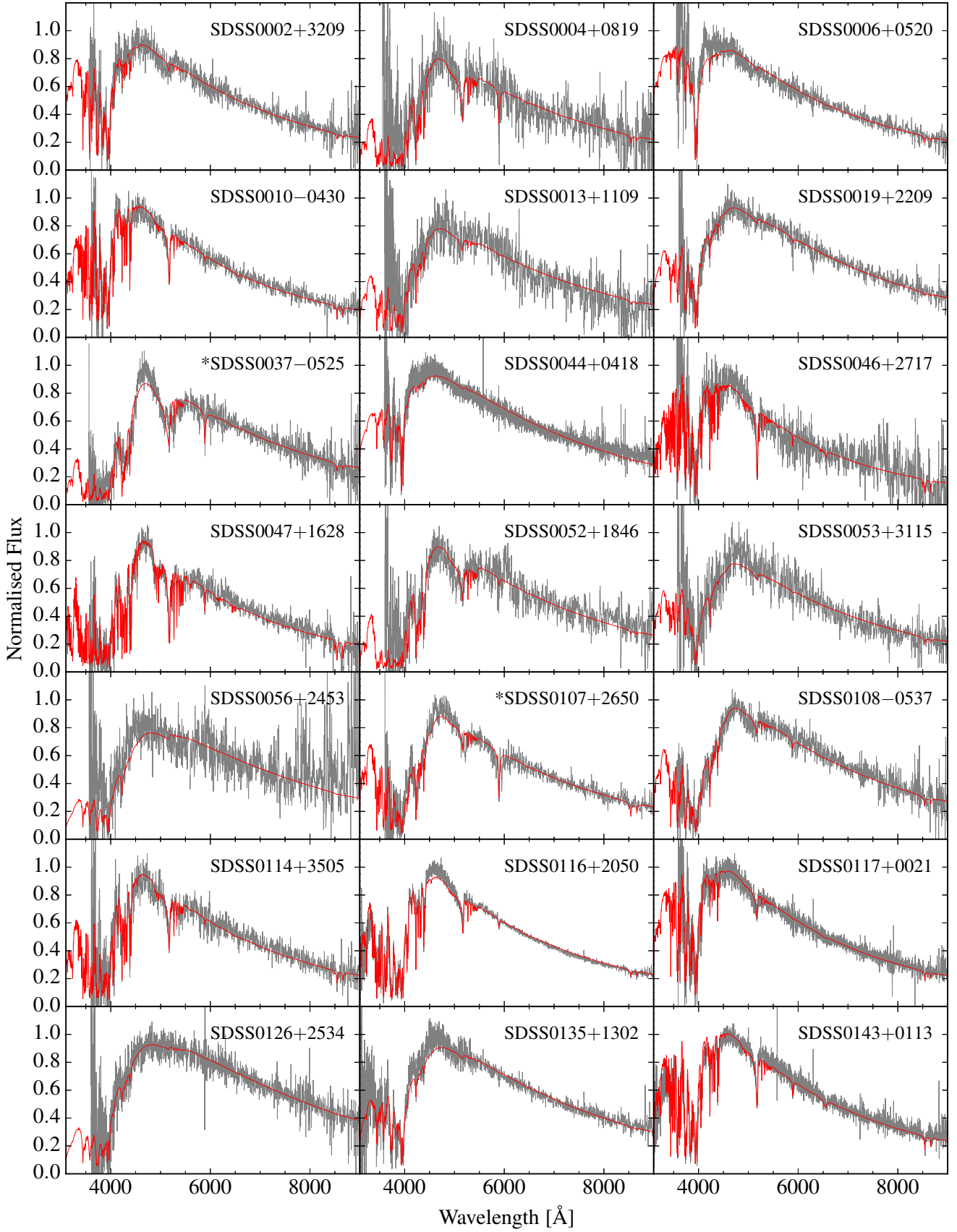


**Figure B2.** DZ spectra with best fitting models. Asterisks precede the name of magnetic systems.



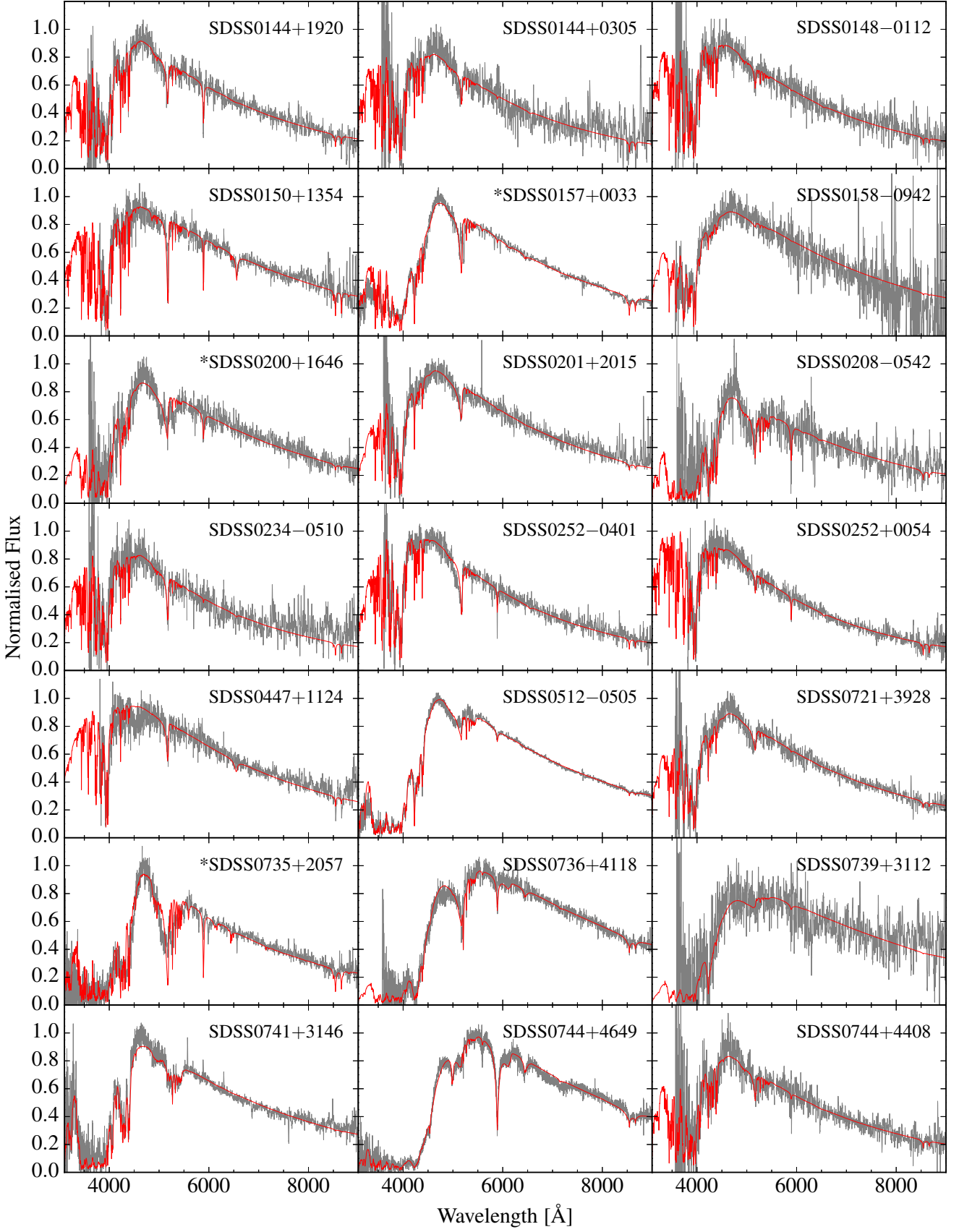


Figure B3. Figure B2 continued.

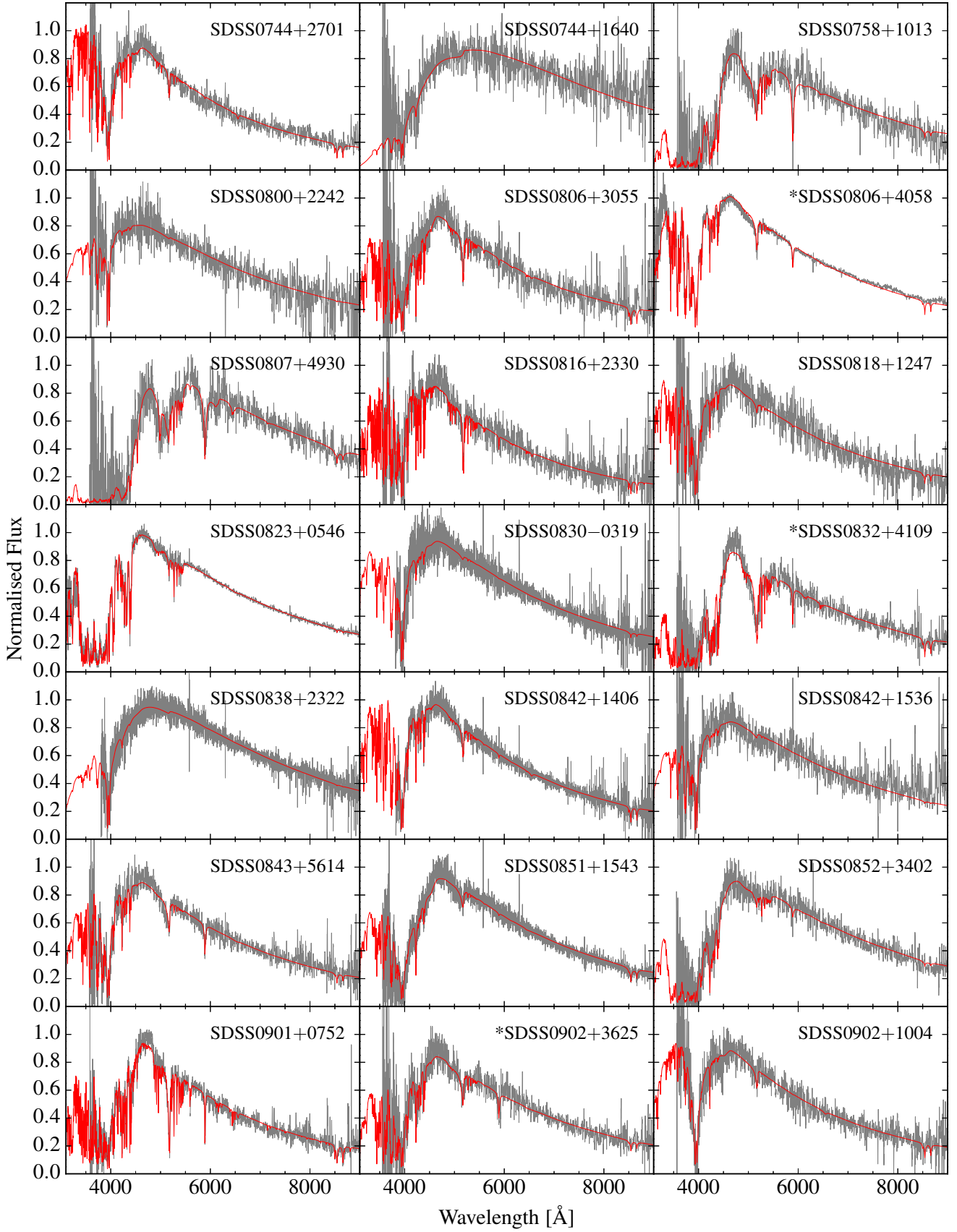


Figure B4. Figure B2 continued.

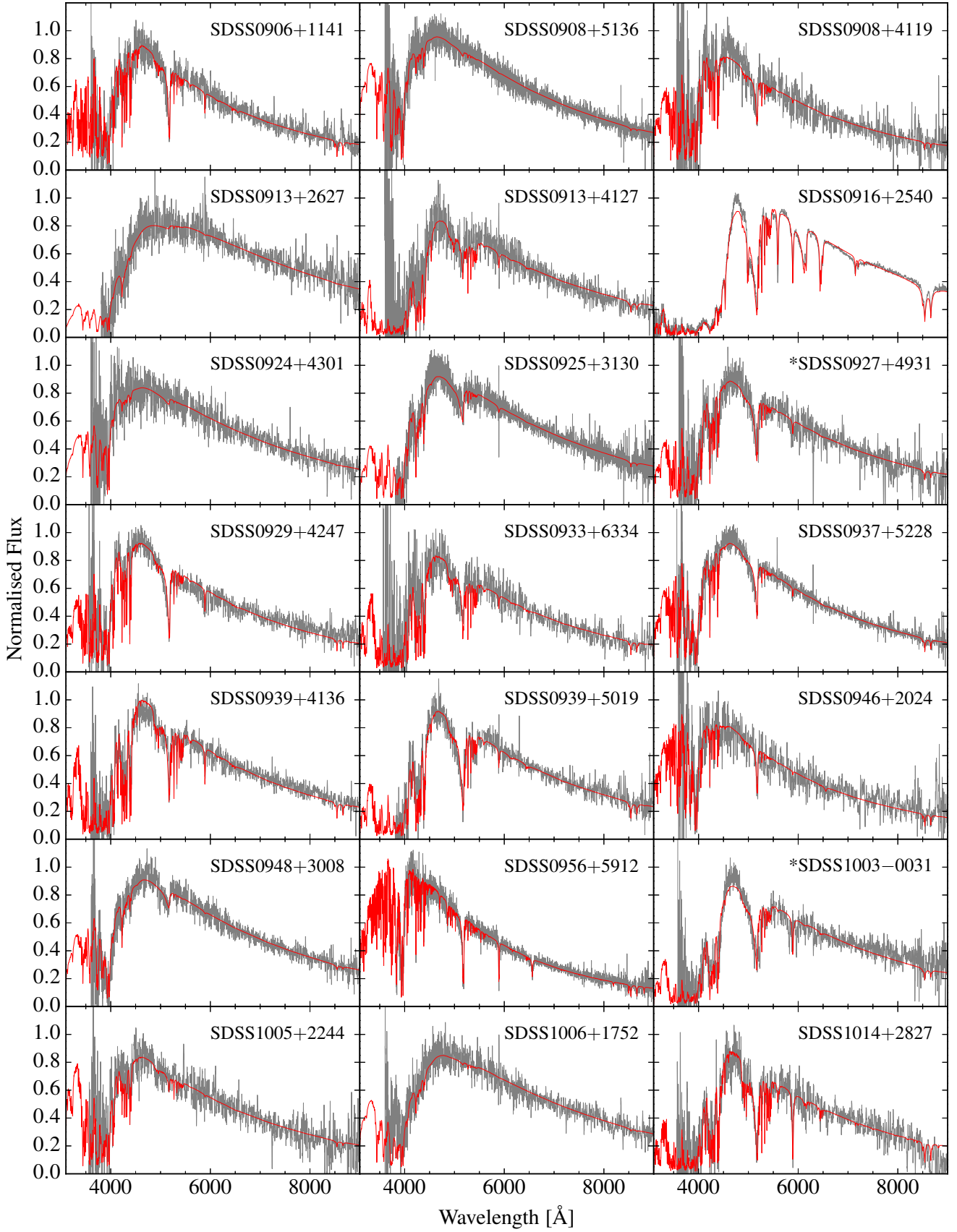


Figure B5. Figure B2 continued.

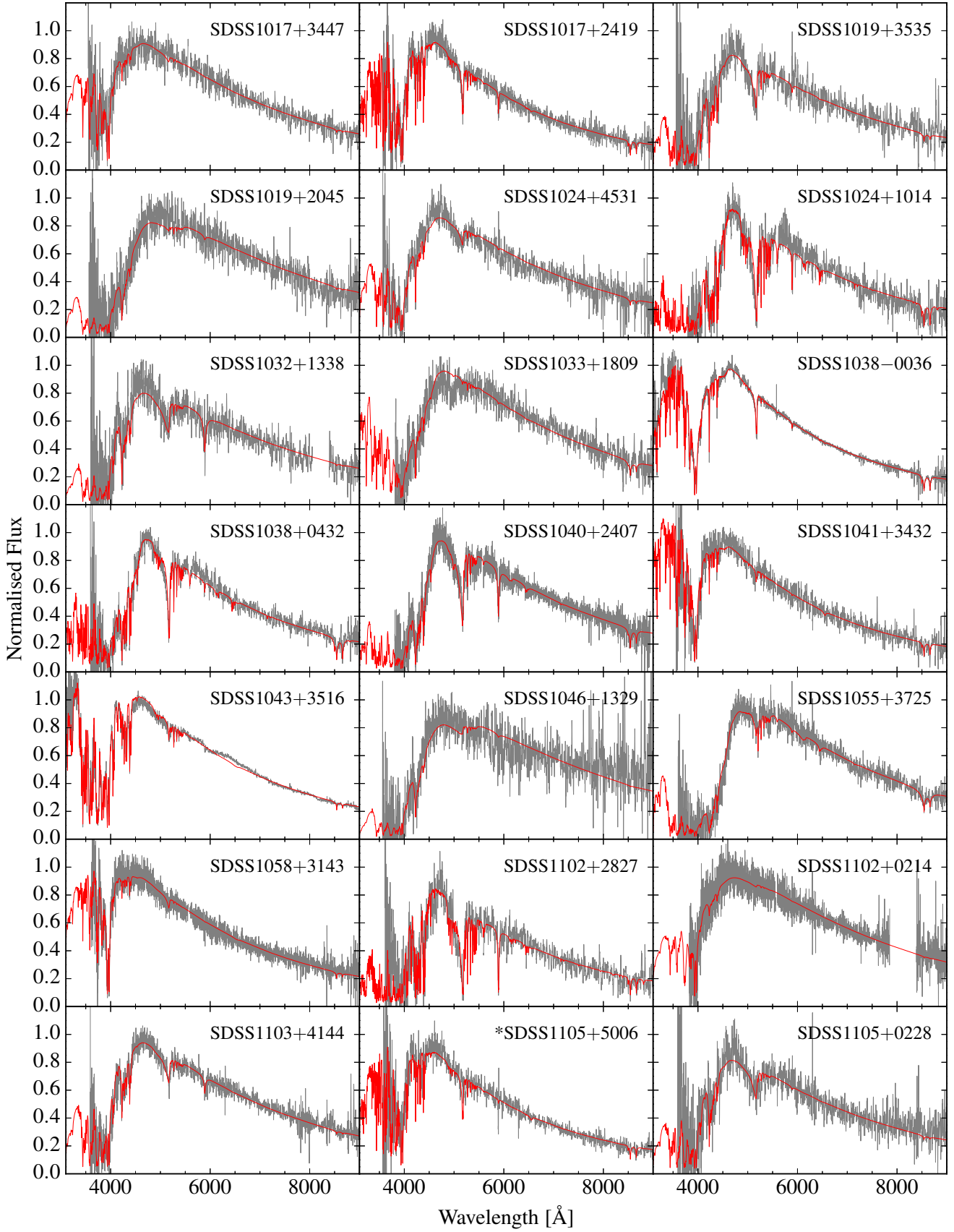


Figure B6. Figure B2 continued.



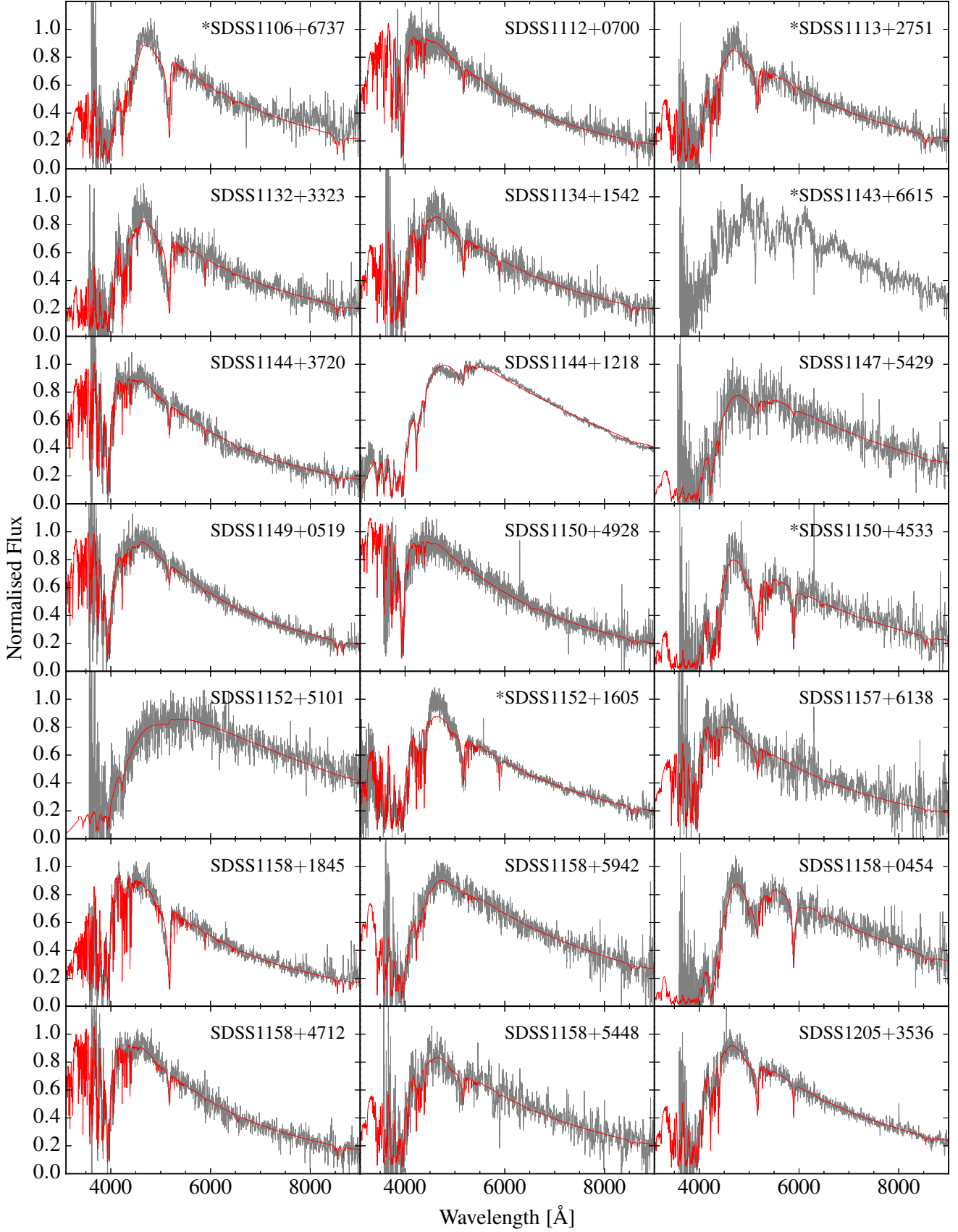


Figure B7. Figure B2 continued.

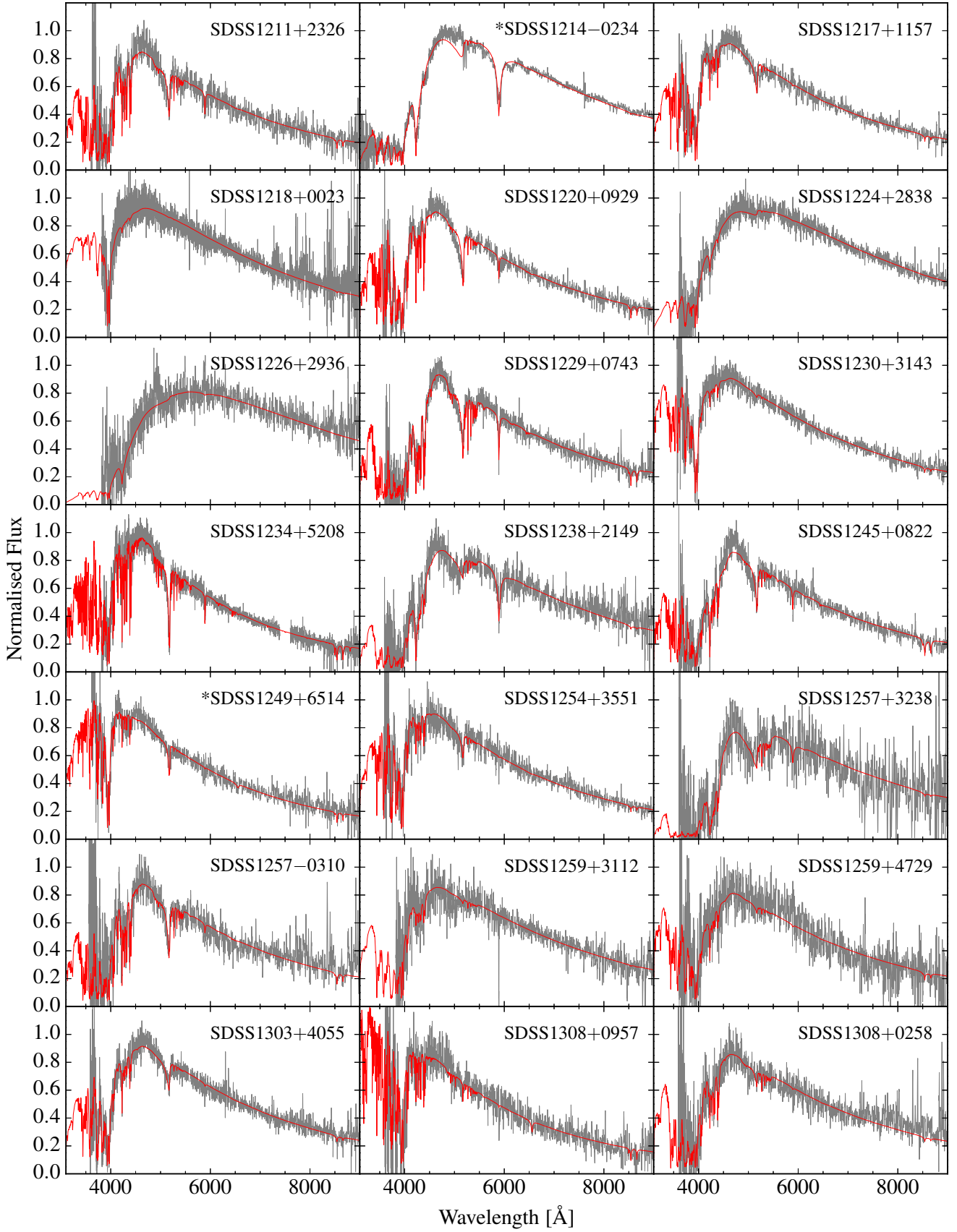


Figure B8. Figure B2 continued.

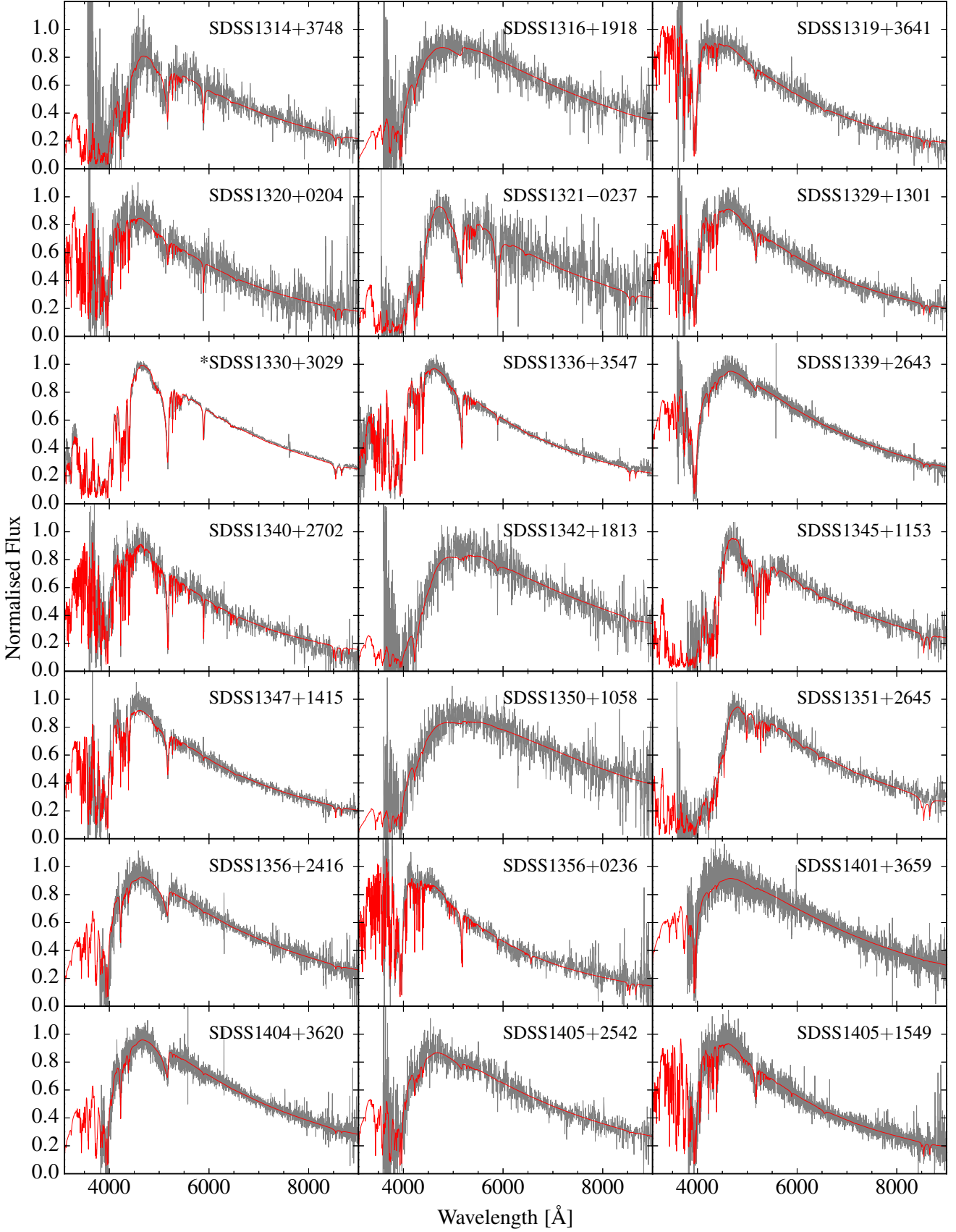


Figure B9. Figure B2 continued.

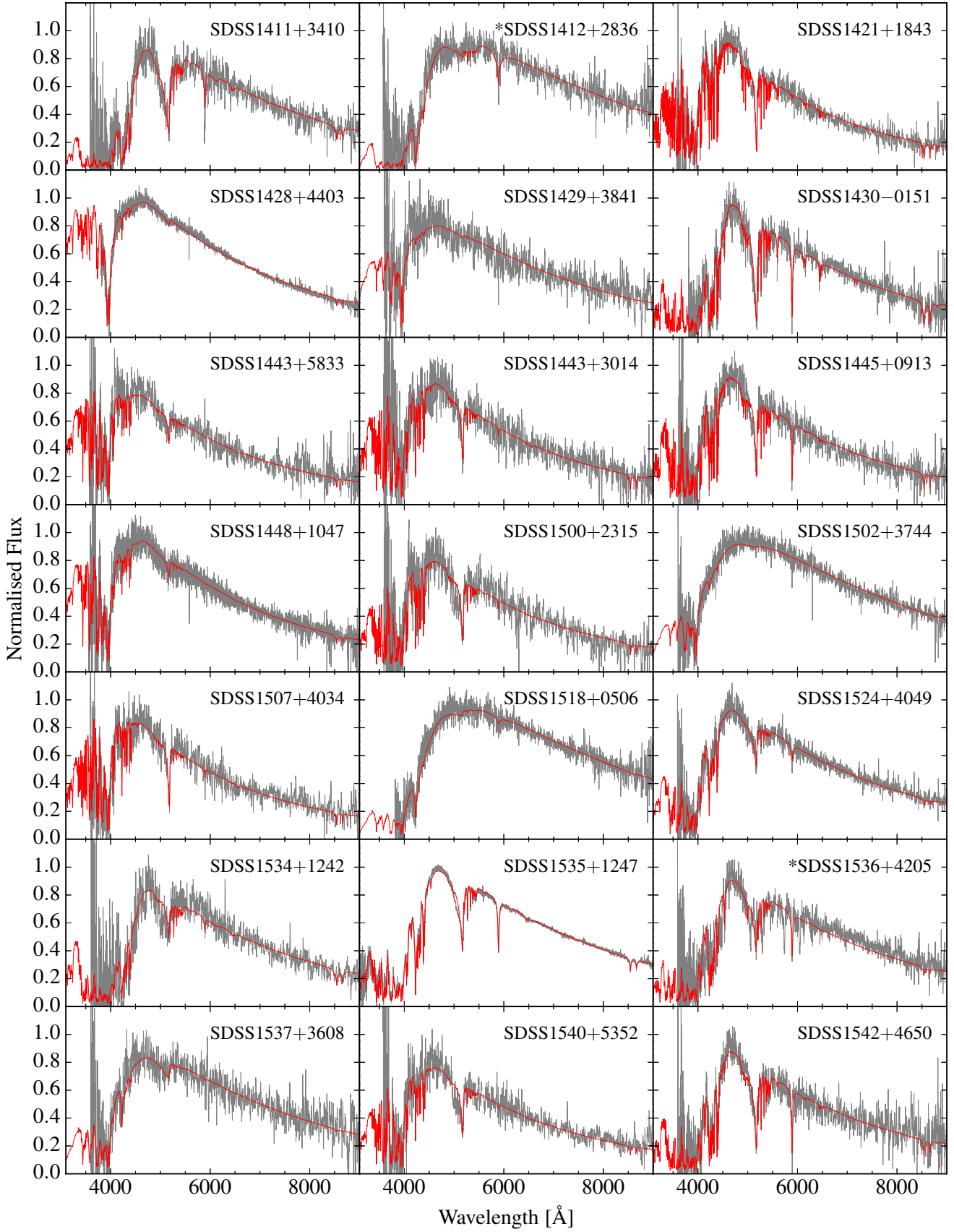


Figure B10. Figure B2 continued.

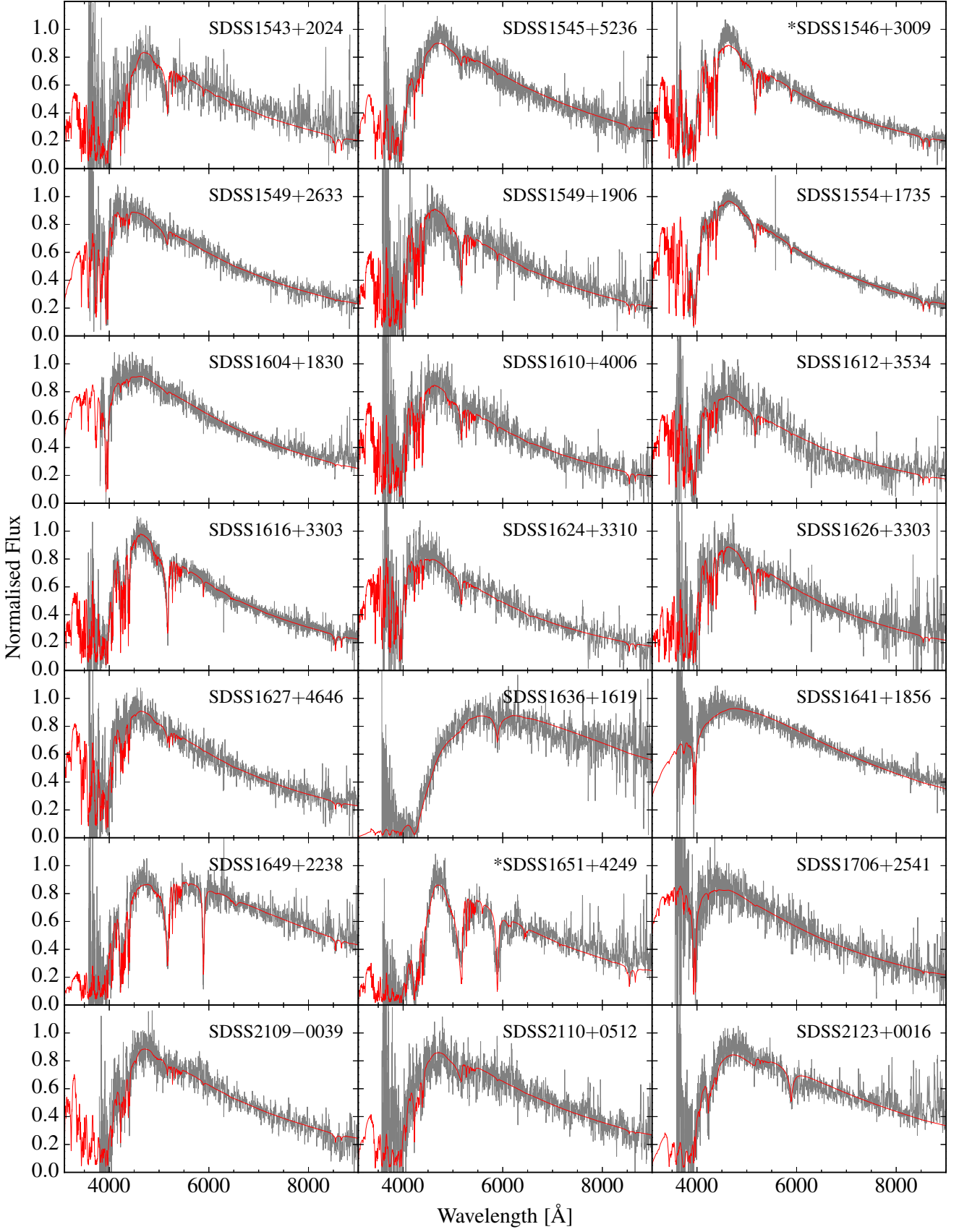


Figure B11. Figure B2 continued.



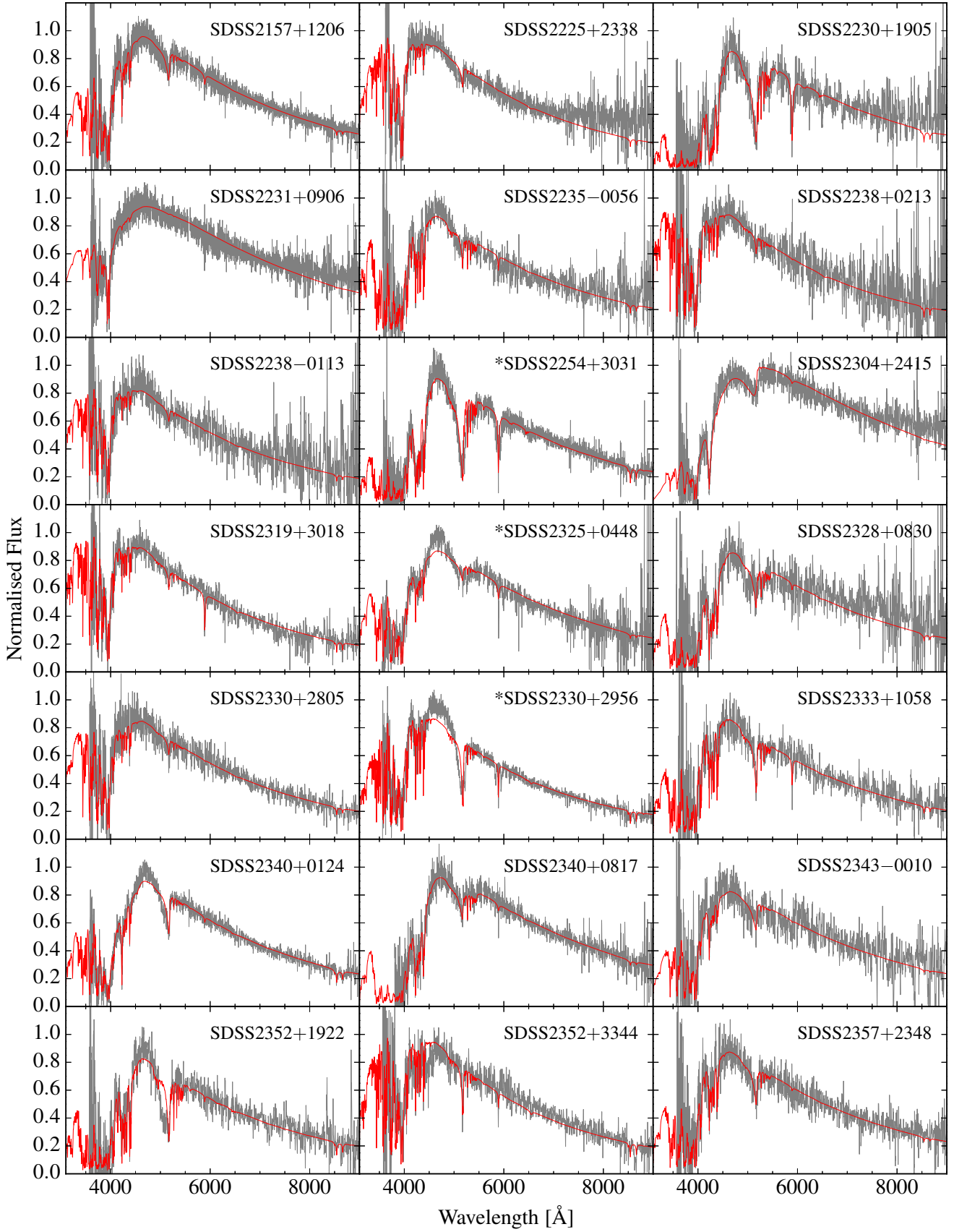


Figure B12. Figure B2 continued.